



Dipl.-Ing. David Veit

Characterization, Verification and Optimization of Ultra-Wideband Impulse Radio Ranging Systems

DOCTORAL THESIS

to achieve the university degree of

Doktor der technischen Wissenschaften

submitted to

Graz University of Technology

Institute of Microwave and Photonic Engineering

Supervisor

Ao.Univ.-Prof. Dipl.-Ing. Dr.techn. Erich Leitgeb

Co-Supervisor

Ass.Prof. Dipl.-Ing. Dr.techn. Michael Gadringer

Graz, August 2020

EIDESSTATTLICHE ERKLÄRUNG

Ich erkläre an Eides statt, dass ich die vorliegende Arbeit selbstständig verfasst, andere als die angegebenen Quellen/Hilfsmittel nicht benutzt, und die den benutzten Quellen wörtlich und inhaltlich entnommenen Stellen als solche kenntlich gemacht habe.


Graz, am 05.08.2020


.....
(Unterschrift)

STATUTORY DECLARATION

I declare that I have authored this thesis independently, that I have not used other than the declared sources/resources, and that I have explicitly indicated all material which has been quoted either literally or by content from the sources used.

Graz, at 05.08.2020


.....
(Signature)

Kurzfassung

Ultrabreitband Impuls Radio verwendet sehr kurze Pulse mit einer Dauer im Nanosekundenbereich. Diese kurzen Pulse nutzen eine große Bandbreite im Frequenzbereich. Die resultierenden Signaleigenschaften machen Ultrabreitband-Systeme robust gegen Fading und erlauben eine Nutzung in Kanälen mit Mehrwegausbreitung, was so mit schmalbandigen Systemen nicht möglich ist. Zusätzlich kann ein Ultrabreitband Impuls Radio präzise die Zeit messen, die ein Puls braucht, um sich von einem Gerät zu einem anderen zu bewegen. Mit Hilfe dieser präzisen Zeitmessung und der Ausbreitungsgeschwindigkeit der elektromagnetischen Wellen, kann man die Distanz zwischen den zwei Geräten schätzen. Unter optimalen Bedingungen liegt der theoretische Schätzfehler bei weniger als einem Zentimeter. In der Praxis können jedoch nur Schätzfehler im Bereich von fünf bis fünfzig Zentimetern erreicht werden. Das zeigt, dass, obwohl es die Ultrabreitband-Technologie schon seit vielen Jahren gibt, sie noch immer ein gewaltiges Potential für Optimierungen birgt.

Ein Grund dafür ist, dass es unzureichend ist dieselben Methoden, die für die Charakterisierung und Modellierung von schmalbandigen Systemen verwendet werden, für das Design von Ultrabreitband-Systemen zu verwenden. Die Modellierung eines Ultrabreitband Impuls Radios, inklusive der Interferenz zwischen mehreren Nutzern und dem Kanal mit Mehrwegausbreitung, ist eine anspruchsvolle Aufgabe, die eine Vielzahl von Annahmen und Vereinfachungen beinhaltet. Diese Annahmen beeinflussen ausschlaggebend die Qualität der abgeleiteten Modelle und daraus resultierend die Korrektheit von Simulationen und Schätzungen. Den Spalt zwischen Schätzung und realem Verhalten zu überwinden ist das Thema meiner Dissertation.

In dieser Arbeit messe, modelliere und analysiere ich den Einfluss von verschiedenen Störfaktoren auf die Leistungsfähigkeit von Ultrabreitband-Distanzschätzsystemen auf Systemebene. Weiter werden Methoden präsentiert, um speziell solche Systeme zu testen und zu charakterisieren. Die gewonnenen Informationen verwende ich zur Optimierung der Hochfrequenz Bauteile und Algorithmen in der Signalverarbeitung, um die bestmögliche Leistung des Gesamtsystems zu erzielen.

Zu Beginn wird eine Simulationsumgebung für den Physikalischen Layer von Ultrabreitband-Systemen präsentiert. Diese kann verwendet werden, um die Kommunikation und Distanzschätzung von Ultrabreitband-Systemen zu simulieren. Mit Hilfe dieser Simulationsumgebung wird auf den Einfluss verschiedener Störfaktoren, wie dispersives Verhalten von Antennen, Verzerrung von Pulsen durch Verstärker sowie schlecht angepasste Antennen, Kanäle mit Mehrwegausbreitung und Interferenz zwischen mehreren Nutzern, eingegangen.

Mit Blick auf die Hardware vergleiche ich analytisch und praktisch verschiedene Möglichkeiten, um Mixed-Mode Load-Pull Messungen durchzuführen. Solche Messungen erlauben die Charakterisierung von Bauteilen mit differentiellen Schnittstellen bezüglich ihres Verhaltens gegenüber differentiellen und Gleichtakt Signalen. Eine neue Methode welche einen größeren Stellbereich erlaubt, wird ebenfalls präsentiert.

Anschließend folgt eine Betrachtung von Methoden zum Durchführen von breitbandigen Load-Pull Messungen mit gepulsten Signalen. Solche Messungen können verwendet werden um Ultrabreitband-Systeme in ihrem Betriebszustand zu charakterisieren. Warum dies notwendig ist, wird anhand von Beispielen erklärt. Des Weiteren präsentiere ich eine neue Methode, um solche Messungen durchzuführen.

Abstract

Ultra-wideband impulse radio uses very short pulses with durations in the nanosecond range. These short pulses occupy a wide bandwidth in the frequency domain. Those signal properties make ultra-wideband systems robust against fading and work even in multipath channels compared to other narrowband communication standards. In addition, ultra-wideband impulse radio is able to precisely measure the time a pulse needs to travel from one device to another. Using this precise time measurement and the propagation velocity of the electromagnetic wave, the distance between the two devices can be estimated. The theoretical ranging error under optimal conditions would be below one centimeter. In practice, these systems show ranging errors from five centimeters up to fifty centimeters. Despite the fact, that ultra-wideband impulse radio systems have been around for many years, they still have a huge potential for optimization.

One reason for this is, that it is insufficient to apply the same methods employed to characterize and model narrowband systems for designing ultra-wideband systems. Modelling an ultra-wideband impulse radio, including multi-user interference and multipath channels, is a demanding task which involves a couple of assumptions and simplifications. These assumptions have a significant impact on the quality of the derived models and subsequently on the predicted performance. To close the gap between the predicted and the real life performance of ultra-wideband ranging systems, I measured, modeled and analyzed the impact of different impairments on the ranging performance on system level. I present methods to test and characterize ultra-wideband systems. Thereafter, I use the gathered information to optimize radio frequency components and the corresponding signal processing to achieve the best communication and ranging performance.

In a first step, I developed a physical layer ultra-wideband system simulation environment. Using this environment, I was able to simulate the communication and ranging performance of ultra-wideband systems. In this way I was able to elaborate the impact of the dispersive behavior of antennas, pulse distortion caused by amplifiers and mismatched antennas, multipath channels and multi-user interference on system performance.

From a hardware perspective, I investigated different approaches for passive mixed-mode load-pull measurements and compared their predicted behavior with measurements. Those measurement systems allow the characterization of devices with differential ports with respect to their differential and common mode behavior. In this context, I was able to introduce a new method, which provides an enhanced tuning range. Thereafter, I investigated wideband load-pull measurements, using pulsed signals, to perform load-pull measurements under the operating conditions of an ultra-wideband impulse radio device. I highlighted the need for such a measurement approach and showed a new method to perform such measurements.

Abbreviations

ADC	Analog Digital Converter
AUT	Antenna Under Test
AWG	Arbitrary Waveform Generator
AWGN	Additive White Gaussian Noise
BPM	Burst Position Modulation
BPPS	Burst Positions Per Symbol
BPSK	Binary Phase Shift Keying
CIR	Channel Impulse Response
CPB	Chips Per Burst
CRLB	Cramér-Rao Lower Bound
CZT	Chirp-Z Transformation
DW1000	Decawave 1000 Chip
DUT	Device Under Test
ECIR	Estimated Channel Impulse Response
FFT	Fast Fourier Transformation
FWHM	Full Width at Half Maximum
GNSS	Global Navigation Satellite Systems
HRP	High Rate Pulse Repetition Frequency
ICZT	Inverse Chirp-Z Transformation
IFFT	Inverse Fast Fourier Transformation
IPS	Indoor Positioning Systems
LF	Low Frequency
LNA	Low Noise Amplifier
LOS	Line-of-Sight
LRP	Low Rate Pulse Repetition Frequency
NLOS	Non Line-of-Sight
PA	Power Amplifier
PAR	Peak-to-Average Power Ratio
PCB	Printed Circuit Board
PHR	Physical Header
PHY	Physical Layer
PRF	Pulse Repetition Frequency
R&S	Rhode und Schwarz
RF	Radio Frequency
RMS	Root-Mean-Square
RS	Reed Solomon

RSS	Received Signal Strength
RTLS	Real-Time Location Systems
RX	Receiver
SA	Signal Analyzer
SECDED	Single Error Correction Double Error Detection
SFD	Start-of-Frame Delimiter
SFG	Signal Flow Graph
SHR	Synchronization Header
SINR	Signal-to-Noise and Interference Ratio
SIR	Signal-to-Interference Ratio
SNR	Signal-to-Noise Ratio
ToA	Time of Arrival
TRL	Through Reflect Line
TX	Transmitter
UWB PHY Sim	Ultra-Wideband Physical Layer Simulation Environment
UWB-IR	Ultra-Wideband Impulse Radio
VNA	Vector Network Analyzer

Equation Style Guide

This section explains different symbol formats in equations.

Vector:	$\underline{f}, \underline{x}, \underline{\sigma}$	$\underline{f} = \begin{bmatrix} f_1 \\ f_2 \\ f_3 \end{bmatrix} = \begin{bmatrix} f_x \\ f_y \\ f_z \end{bmatrix}$	(lower case letters if possible)
Matrix:	$\underline{F}, \underline{X}, \underline{\Sigma}$	$\underline{S} = \begin{bmatrix} S_{11} & S_{12} \\ S_{21} & S_{22} \end{bmatrix}$	(upper case letters if possible)
Random Variables:	$\mathbf{F}, \mathbf{X}, \mathbf{\Sigma}$		
Realization of a RV:	f, x, σ		
Definition of RV X:	$\mathbf{X} \sim N(\sigma, \mu)$		
PDF of RV X:	$\pi_x(x)$		
CDF of RV X:	$\Pi_x(x)$		
Mean Values:	$\bar{f}, \bar{X}, \bar{\Sigma}$		
Estimated Values:	$\tilde{f}, \tilde{X}, \tilde{\Sigma}$		

Table of Contents

Kurzfassung	i
Abstract	ii
Abbreviations	iii
Equation Style Guide	iv
1 Introduction	1
1.1 Structure	1
1.2 Motivation and Applications	2
2 Basic Knowledge	5
2.1 UWB and the IEEE 802.15.4 Standard	5
2.1.1 Transmitter	6
2.1.2 A Possible Receiver Implementation	7
2.2 Wireless Multipath Channels	7
2.2.1 Theoretical Performance Limits of Time-Based Ranging	9
2.2.2 Antennas as Part of the Channel	9
2.3 Introduction to Mixed-Mode S-Parameters	10
3 System Level Performance Analysis	15
3.1 The Simulation Environment	15
3.1.1 Transmitter	16
3.1.2 Channel and Antennas	18
3.1.3 Noise	18
3.1.4 Interference	19
3.1.5 Receiver	20
3.1.6 Distance Estimation	22
3.1.7 Database	22
3.2 Impact of Antenna Angle Dependencies	24
3.2.1 Antenna Designs and Measurement Setup	24
3.2.2 Measurement Results	25
3.2.3 Performance Analysis	30
3.3 Impact of Pulse Distortion	33
3.3.1 Measurement Setup	33
3.3.2 Measurement Results	34
3.3.3 Discussion of Measurement Results	36
3.4 Simulation of a Two-Ray Channel	37
3.5 Multiuser Interference Simulations	38
3.6 Conclusion for System Level Analysis	40

4	Device Characterization and Optimization	42
4.1	De-Embedding for Mixed-Mode Load-Pull Setups.....	44
4.1.1	Demo Setup	45
4.1.2	De-Embedding with Signal Flow Graphs	46
4.1.3	De-Embedding Results	49
4.2	Mixed-Mode Load-Pull	51
4.2.1	Load Configurations	51
4.2.2	Impact of Non-Ideal 180° Hybrids	54
4.2.3	Measurement Setups	59
4.2.4	Results for Load Networks.....	61
4.2.5	Results of Mixed-Mode Load-Pull Measurements	64
4.3	Wideband Load-Pull	66
4.3.1	Keeping Distances Short.....	67
4.3.2	The Two-Pulse Method	73
4.4	Conclusion for Device Characterization	78
5	Final Conclusion	80
5.1	Findings.....	80
5.2	The Future of UWB.....	80
	References.....	82
	List of Own Publications	88
	Appendix.....	89
	Appendix A : Chirp Z-Transformation and Correct Normalization	89
A.1	Results	89
A.2	CZT Implementation	93
A.3	ICZT Implementation	94
	Appendix B : Mixed-Mode S-Parameters for Matlab®	95

1 Introduction

For our modern society, the ability to accurately localize devices is essential for many applications. For large-scale outdoor localization, Global Navigation Satellite Systems (GNSS) are commonly used. Though GNSS systems provide a wide coverage, they have significant disadvantages when it comes to indoor localization, response time and power consumption. If a receiver cannot receive a GNSS signal from satellites inside a building, the receiver cannot locate itself. Should the receiver be able to receive signals, they will contain a large number of multipath components, drastically affecting the localization accuracy. Due to this reason Indoor Localization Systems, also called Indoor Positioning Systems (IPS) or Real-time Location Systems (RTLS), were developed. A RTLS is designed for short range indoor localization and does not use signals coming from space satellites. The “satellites” of an RTLS are often called “anchors” and are installed in the available infrastructure, while the mobile receivers are termed “tags” and can locate their position based on the available anchors.

1.1 Structure

In this thesis, I deal with the characterization and optimization of indoor positioning systems using ultra-wideband impulse radio technology (UWB-IR). In Section 1.2 I continue the introduction with a comparison of different ranging technologies and applications that benefit from indoor positioning systems. In Section 2.1 the basic working principle of UWB-IR ranging is explained with references to the IEEE 802.15.4 standard. Then I introduce the basics of wireless channels and multipath propagation in Section 2.2, followed by a short excursion into the world of differential signals and transmission lines in Section 2.3.

Based on the work of [1], [2], [3], [4] and [5] I elaborate on the need to investigate the system level performance of an UWB system in Section 3. In the past several analytical methods were developed to estimate the performance of UWB-IR systems, some of them are presented in [6], [7], [8] and [9]. In [2] it was proven that for UWB-IR a characterization of multi-user interference with a Gaussian model leads to overoptimistic predictions, rendering many analytical methods incorrect. Furthermore, the majority of the presented analytical models is only valid for a single combination of channel models, receiver architectures and pulse shapes, in case the pulse shape is considered at all. This makes a comparison of different systems nearly impossible or at least very impractical. Due to this reason, I propose a physical layer UWB simulation environment in Section 3.1. In comparison to existing simulation environments and analytical models, the presented one is also able to simulate the ranging error in addition to the bit error rate. This allows the investigation of the impact of different factors, like the angle dependent impulse response of an antenna, multiuser interference or pulse distortion caused by amplifiers, on UWB ranging and communication performance, as they are presented in the Sections 3.2 to 3.5. The findings of these Sections are then summarized in Section 3.6.

As the simulations mentioned in the previous paragraph depend on accurate models of the used hardware the characterization and optimization of devices using a load-pull approach is discussed in Section 4. A method to de-embed complicated mixed-mode load-pull setups is presented in Section 4.1. Building on the results presented in [10], [11], [12], [13], [14], [15] and [16] I present a new approach for passive mixed-mode load-pull which can be used to trade tuning range for ease of use and increased hardware effort in Section 4.2. As we are dealing with ultra-wideband signals, I also investigated different ways to perform wideband load-pull measurements using pulsed signals, which to the best of my knowledge has not been discussed in literature. The results of these investigations

are presented in Section 4.3, followed by a summary of the findings regarding mixed-mode and wideband load-pull measurements in Section 4.4.

As this thesis deals with two major topics, which are system level performance analysis and the characterization and optimization of non-linear devices, also the content is grouped into two sections, each having its own conclusion section.

Last but not least everybody interested in time-frequency domain conversion should have a look at the appendix. Starting from the traditional approaches shown in [17] and [18] I present results for the Chirp-Z Transformation using a normalization method I developed. This normalization method allows direct comparison of signals which were calculated with different time and frequency vectors, which would otherwise cause a different scaling for each of the signals.

1.2 Motivation and Applications

Indoor positioning systems are useful in applications where the position of a person or device is of interest. Many indoor localization systems are for example applied in shopping malls, hospitals, airports, logistics, farming or robotics. Due to the COVID-19 virus, localization systems are currently used to estimate the distance between persons and notify them if they are too close to each other. Mobile apps for tracking persons in your vicinity using the same app were employed. In case one of the tracked persons was tested positive for COVID-19, all persons which had contact to this person could be notified automatically. This vast field of applications requires different technical realizations. These range from simple but fast distance tracking between two objects or persons as mentioned for the COVID-19 distance tracker to localization of many objects with very low update rates and long battery lifetimes. The needed accuracy of the desired indoor location estimate is also an important factor and together with the application defines the best suited technology. Therefore, knowing the requirements of a system is the first and most important step in development. A comparison of different ranging technologies is shown below in Table 1. In the next sections I will give a few examples of how localization systems can improve workflows and provide new insights into existing processes.

Table 1. Comparison of different ranging technologies as in [19].

	Wi-Fi	Bluetooth	Passive RFID	Active RFID	UWB
Accuracy [m]	< 15	< 10	< 0.1	< 3	< 0.3
Range [m]	< 10	< 50	< 1	< 5 ... 30	< 100
Battery Lifetime	Medium (weeks-months)	High (years)	Only base station needs power.	High (years)	Low-Medium (days-months)
Number of Tags per Area	High	High	Low	Medium	Low-High (depends on protocol and update rate)
Scalability to Large Areas	Medium	Medium	Easy	Medium	Complex
Price	€€	€€	€	€€€€	€€€

a. Shopping Malls and Analytics

In shopping malls and retail stores, customer motions and behaviors are tracked by using their recorded indoor positions for data analysis. Intelligent software counts customers, offers customer flows, motion maps, heat maps, point-of-sale analytics and even demand management which can be based on indoor localization systems. [19]

b. Industry 4.0 and Logistics

Information about the exact positions, speeds, and tracks of forklifts, vehicles or operators at any time in a production facility or warehouse is a valuable piece of information to analyze traffic and identify workflow bottlenecks to save time and money. But not only traffic analysis is valuable, also access control to certain areas, navigation to relevant positions with new tasks on optimized routes can reduce time and improve efficiency. [19]

c. Sports

In any sport, precise localization and tracking of players is of interest to analyze players, record their motion and monitor their performance over a certain period. Specific optimizations can be drawn even during the game, when real-time data is available and the trainer realizes a player is not in focus. [19]

d. Healthcare

Hundreds of million euros are lost every year due to search and loss of equipment, like monitors, wheelchairs, beds, etc. By tracking the location of equipment, searching is reduced to a minimum and purchasing decisions can be evidence based. Also a continuous log of patient-caregiver interactions, from continuous improvement to litigation or compliance can be covered by an IPS. A patient can even be located quickly for medication, staff routines, when his family wants to pay a visit and he is gone somewhere else, or to alert staff immediately if he left the facility. Localization systems improve the efficiency in your daily job and increase comfort and security in healthcare and assisted living. [19]

e. Automotive Use Case

In the past few years, Keyless Go systems have been in the news a lot. Mostly because cars using early versions of this technology got stolen quite frequently. This is because relay station attacks were able to trick these systems into believing that the key is close to the car. Mostly low frequency (LF) technology was used for these early versions of Keyless Go systems. The decision if a key is close to the car was simply based on the signal strength. Relaying the LF signals between car and key, thereby increasing the received signal strength and faking a key position close to the car can easily be achieved with electronic equipment you can buy for less than 150€. It becomes worse if you consider that encryption does not help to solve this problem, as a relay station does not need to decode the signal. Due to this reason, car manufacturers have been working hard to add additional security layers.

One way to increase the security of existing LF systems is to use 3D coils as shown in Figure 1.1 to measure the 3D field vector. There are different ways to use this vector information to counter relay station attacks. One way is to use different anchors at the car and fire them one after another. The field vector then needs to change depending on the active anchor. If this is not the case, the key knows that the signal is not coming from the car but from a single relay station. But by using multiple relay stations, this system could be tricked as well, although the effort is already much higher. An additional layer of security could be added if the anchors are fired one after another and then multiple anchors at the same time. Then the sum of the first measured vectors should be equal to the measurement of the superimposed field vectors. For this a relay station would also need to resemble the geometry of the anchors relative to the key, which is significantly more effort and cannot be done easily. A downside of this approach is that the measurement time is relatively long (hundreds of milliseconds to seconds) and that the system might not work if the key moves between measurements, because this also changes the vectors similar to a relay station attack.

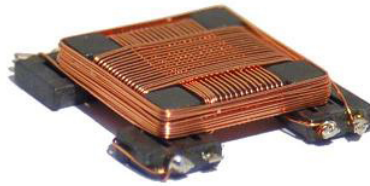


Figure 1.1. phot of a 3D coil used for LF communication.
(<https://www.grupopremo.com/img/imported/uploads/fck/3dc15-HF.JPG>)

Another way to counter relay station attacks is to not rely on the signal strength to determine the distance between key and car. This is where indoor positioning systems come into play. Indoor positioning systems like ultra-wideband (UWB), Wi-Fi or Bluetooth do not only rely on the signal strength to estimate the distance. In addition, they measure the travel time of the signal or direction the signal is coming from. These methods are called time-of-arrival and angle-of-arrival methods. As you can see in Table 1 the ranging accuracy of Wi-Fi and Bluetooth is low compared to UWB. This makes UWB attractive for car manufacturers because it also enables additional applications like detecting if a key is inside or outside a car. This can be used to prevent locking up your key in the trunk of your car. Furthermore, a good ranging accuracy is important for security. Just think what will happen if you park your car right next to your house and the ranging accuracy is about 10 m. In some cases the car might unlock believing the key is close enough, although it is inside the house.

In addition phone manufacturers are now starting to build UWB chips into smartphones, Apple being the first one to build UWB into their iPhone 11 [20]. Smartphones are already an integral part of our lives, they are not only used for making phone calls, writing text messages, organizing your appointments, or playing games. With pay services they started to replace physical credit cards, Google and Qualcomm are also working to replace ID cards by apps [21] with the aim of the smartphone doing away with the wallet entirely. And soon smartphones will also replace car keys, making it easy to share and manage permissions for example between family members. All these factors make UWB a promising technology for the automotive industry. But although UWB ranging systems have been around for more than 10 years, it is still a topic that needs to be investigated to achieve the best possible experience for customers and manufacturers. In the next chapter, I will explain the basics of UWB using the IEEE 802.15.4 standard as reference.

2 Basic Knowledge

This section provides the foundation for all following discussions. I start with a short roundup of the IEEE 802.15.4 standard, which UWB is a part of. Followed by a discussion about multipath channels and why they pose a problem for ranging applications as well as derivations for theoretical limits for range estimators. I also explain why antennas should be considered to be a part of the wireless transmission channel. At last this section introduces mixed-mode S-parameters which are used to describe networks with differential ports.

2.1 UWB and the IEEE 802.15.4 Standard

The IEEE 802.15.4 standard [22] defines common functionalities of low rate and short range systems to allow interoperability between devices of different manufacturers. This standard also includes detailed specifications for UWB systems. In the following sub-sections I will give a coarse explanation of the working principle of such an UWB system. For more detailed information have a look at section 16. of the IEEE 802.15.4 standard, which deals with the physical layer of high rate pulse repetition frequency ultra-wideband systems (HRP UWB PHY), which I will simply call UWB PHY for the remainder of this thesis. In contrast to the high rate pulse repetition frequency UWB systems there are also low rate pulse repetition frequency UWB systems (LRP UWB) which work slightly different and are also explained in the standard. This thesis only deals with HRP UWB systems, but most findings could also be applied to LRP UWB systems.

Before having a look at each building block an overview of an UWB system is given in Figure 2.1. The blue block (TX Chip) and red block (RX Chip) represent what is included in the IEEE 802.15.4 standard. In my opinion, the wireless transmission channel is also an important part of the overall system. For this reason, I also added the channel to the system overview. A more detailed discussion of wireless multipath channels can be found in Section 2.2. UWB can use several different bands ranging from 250 MHz up to 10.6 GHz and a single band may have a bandwidth of up to 1.3 GHz. A combination of burst position modulation (BPM) and binary phase-shift keying (BPSK) is used to support coherent and non-coherent receivers using a common signaling scheme. To increase interference rejection also burst position hopping is applied. By changing the number of possible burst positions in the frame and the duration of each burst, various data rates can be supported. Forward error correction coding in the form of an inner block code and outer convolutional code is employed to protect the data from transmission errors. [22]

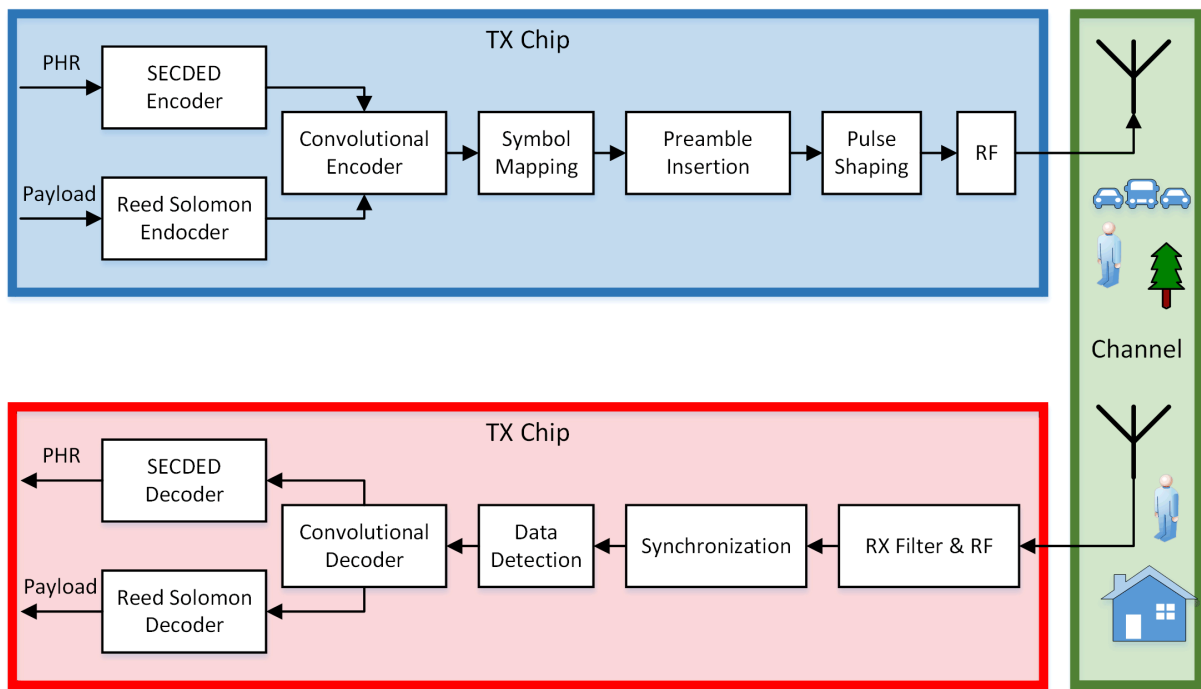


Figure 2.1. UWB system overview block diagram.

2.1.1 Transmitter

I will discuss the building blocks in the order the data passes through them, starting with the block encoders in the transmitter (TX). The Physical Header (PHR) is 18 bits long and contains information about the data rate, frame length, preamble duration and if the frame is used for ranging. It is the first section in the data part of a frame, followed by the payload data. As this information is needed in the receiver the PHR is encoded separately from the payload using single error correction double error detection (SECEDED) encoding. Differently the payload data is encoded using a Reed Solomon (RS) block code. After the inner encoding with a block code a systematic outer convolutional code with code rate $\frac{1}{2}$ is added. This combination is popular as convolutional decoders tend to produce blocks of errors and RS decoders are good at correcting those. The parity information produced by the systematic convolutional encoder is incorporated in the polarity of the transmitted pulses by using the BPSK part of the modulator. If the receiver is a non-coherent receiver this additional information cannot be used. As the code is systematic, such receivers can still decode the received signal even without this additional parity information. After the encoders, the data is mapped to the corresponding symbols using the BPM part of the modulator. Depending on the position of the burst in the frame either a "1" or "0" is transmitted (see Figure 3.5 on page 22). [22]

After the symbol mapping the data part of a frame is ready for transmission. But for synchronization and ranging a frame also needs a synchronization header (SHR). This SHR is added before the data part and contains between 16 or 4096 repetitions of a symbol generated using a ternary code with a length of either 31 or 127. The +1 and -1 symbols again indicate the polarity of a pulse, while the 0 symbol indicates a missing pulse. The different codes in [22] are designed in a way to provide optimum cross correlation and auto correlation functions, increasing interference rejection and ranging performance. The ternary code used for the SHR of a frame is also used to generate the burst position hopping sequence for the data part, again using the optimum cross correlation functions to increase interference rejection. A specific start-of-frame delimiter symbol (SFD) indicates the end of the SHR and start of the PHR.

After all parts of the frame are assembled into a ternary sequence of pulses, the baseband signal needs to be generated in the pulse shaper. The standard defines a root raised cosine pulse with a roll-off factor of 0.5 as a reference pulse. In order to be compliant with this standard, the cross-correlation function of the transmitted pulse and the reference pulse must have a main lobe with magnitude greater to 0.8 for at least 0.5 ns for low bandwidth channels and 0.2 ns for high bandwidth channels. For comparison the pulse duration for low bandwidth channels is 2 ns and for high bandwidth channels between 0.74 ns and 0.92 ns. [22]

This definition is beneficial because manufacturers can choose different pulse shapes to increase ranging performance. The problem with the root raised cosine pulse shape is that its autocorrelation function has leading side lobes, which reduce the dynamic range of the ranging in the receiver if a leading edge detection algorithm is used. Leading us directly to the next section about a possible receiver implementation as it is mentioned in [22].

2.1.2 A Possible Receiver Implementation

In this section I will shortly explain how an UWB receiver (RX) could work. As the standard does not demand a specific receiver implementation and the information about receivers in [22] is purely informative, different implementations are possible. Figure 2.1 shows that in general the first part in a receiver is the radio frequency (RF) section including the filters used for pulse shaping in the receiver. As you know from other communication systems the pulse shaping can be split between the transmitter and receiver. This may or may not be used in an UWB system. In any case a receive filter is needed to attenuate out of band interference signals before the bandpass signal enters the demodulator. In this case, I assume an IQ demodulator for coherent demodulation of the signal. The outputs of the IQ demodulator are the I and Q baseband signals which are then sampled in an ADC. After the receiver synchronized its clock to the received signal using the SHR it starts correlating the received symbols of the SHR with the preamble code which is known to the transmitter and receiver. This cross correlation can then be used to calculate an estimated channel impulse response. More details about this topic are provided in Section 3.1.5 on page 21. Once the start-of-frame delimiter has been detected, the receiver starts to decode the BPM symbols. In case of an IQ demodulator the I and Q signals can be used to determine the polarity of individual pulses. This polarity information can be used together with the systematic data from the burst positions to generate the input bit stream for the convolutional decoder. The output of the convolutional decoder is split to decode the first part containing information about the PHR in the SECDED decoder, and the second part with the payload data in the Reed Solomon decoder. If the forward error correction coding managed to remove all errors the receiver should have received the same data that was supplied to the transmitter. In addition, the receiver also knows the estimated channel impulse response of the propagation channel. This estimated channel impulse response in combination with a timestamp transmitted in the payload can be used to estimate the distance between transmitter and receiver. More information on how this is accomplished can be found in [23], [24], [25], [26], [27] and [28]. General information on UWB transceiver design can be found in [29] and [30].

2.2 Wireless Multipath Channels

Localization performance depends highly on the accuracy of the combined range and/or direction measurements. Because UWB uses mainly time-of-arrival (ToA) for ranging, which can provide high ranging accuracy compared to other techniques, this section is focused on the error sources in time-based ranging methods. First, I need to introduce some terms with reference to Figure 2.2 [26]. A

line-of-sight (LOS) channel is a channel where the direct path between the TX and RX is free of blocking elements, as between TX and RX₁. For non line-of-sight (NLOS) channels the direct path is obstructed by some obstacles. This may cause a reduction in signal strength of the direct path component (often called LOS component) as well as a delay due to varying propagation velocities in different media. Between TX and RX₂ the direct path is attenuated and probably delayed, but can still be received by RX₂. The thick wall surrounding RX₃ heavily attenuates the LOS component below the sensitivity of RX₃. RX₂ and RX₃ receive non direct path components (often called NLOS components) coming from different reflectors. Because the signal transmitted by TX takes multiple paths to the corresponding RX we are talking about a multipath channel. Please note that the scenario missing in Figure 2.2 is that RX₁ also receives reflections coming from a reflector and the direct path is not blocked. This is commonly called a LOS multipath channel.

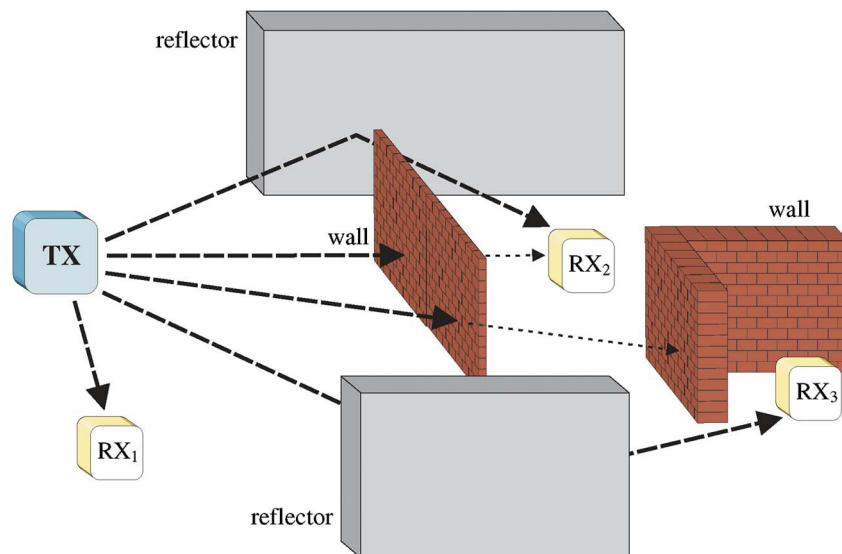


Figure 2.2. Possible LOS and NLOS conditions from transmitter to various receivers. RX₁ is in LOS condition, RX₂ is in NLOS condition without direct path blocking, and RX₃ is in NLOS condition with direct path blocking, as shown in [26].

For communication systems, these effects are quite welcome as a RX is able to receive a signal even if no LOS component is available. For ranging systems, a problem arises. The RX does not know if it is receiving a LOS or NLOS component and often just assumes that the first signal it receives is the LOS component. Furthermore, the receiver assumes a constant propagation velocity as not the distance but the propagation delay is the measured physical property. This causes ranging errors due to the wireless multipath channel. The error sources can be grouped together like summarized below.

1. Multipath Fading: Constructive and destructive interference. Especially harmful for narrowband systems. Harsh multipath conditions can also affect wideband signals possibly causing a negative or positive ranging error.
2. Direct Path Excess Delay: Change in propagation velocity due to the direct path travelling through different media. Adds a positive bias to the range estimate.
3. Direct Patch Blocking: The LOS component is completely blocked from the RX allowing only the reception of NLOS components. The RX will wrongly interpret a NLOS component as LOS component, which also adds a positive bias to the range estimate.

There are also error sources that do not belong to the channel and, therefore, are not being discussed here. Two examples are clock drift and interference [26].

2.2.1 Theoretical Performance Limits of Time-Based Ranging

We know that time-based ranging requires the estimation of the time-of-arrival of the direct path. By deriving the Cramér-Rao lower bound (CRLB) as a lower threshold for the mean square error of the unbiased ranging estimate, we develop an understanding of which parameters affect ranging accuracy and how strong the impact is. If you are interested in the derivations, please have a look at [26], [31], [32] and [33]. In (2.1) the bandwidth of the signal is introduced with β , which is the second moment of the spectrum. For an Additive White Gaussian Noise (AWGN) channel and multipath channels with resolvable multipath components, the only other parameter affecting the CRLB is the signal-to-noise and interference ratio (SINR). For dense multipath channels, an effective signal-to-noise and interference ratio \widehat{SINR} was introduced in [32] to incorporate the effect of the dense multipath channel. By looking at (2.1) it becomes obvious why higher bandwidths are desired for ranging applications as the CRLB decreases with the bandwidth to the power of two while the signal power only has a linear impact. For comparison in (2.2) the CRLB for ranging systems using received signal strength (RSS) measurements for ranging is provided. Here, it only depends on the transmit signal power σ_s , the path loss exponent γ of the channel and the distance d . This means for RSS based ranging the bandwidth has no impact. In [26] it was shown that for practical implementations the dependency of the CRLB to the square of the bandwidth only occurs up to 2.5 GHz. Above 5 GHz of bandwidth, nearly no further improvement can be observed. Experimental results confirming this were presented in [34].

$$CRLB_{\text{time}} = \frac{1}{8\pi^2 \beta^2 SINR} \quad (2.1)$$

$$CRLB_{RSS} = \left(\frac{\ln(10)}{10} \frac{\sigma_s d}{\gamma} \right)^2 \quad (2.2)$$

2.2.2 Antennas as Part of the Channel

It is hard to separate the influence of antennas and propagation channels, as objects which physically belong to the channel might lie within the near field region of an antenna. Any objects introducing a distortion within an antenna's near field change the behavior and inherent properties of the antenna. The fact that there is no hard boundary between near-field and far-field complicates matters even more. For further information on near field and far field boundaries, I refer to my investigations presented in [35]. Although, they were performed for a radar use case, the analytical equations for far field and near field behavior boundaries are the same.

In addition to the gain of an antenna, also its impulse response is of importance for UWB ranging systems. This becomes obvious when looking at Figure 2.3 to Figure 2.6. They show a comparison of the angle dependent impulse response between a Vivaldi antenna and log-periodic antenna which was presented in [36]. Although the log-periodic antenna covers a wide bandwidth, its impulse response is very long in comparison to the impulse response of the Vivaldi antenna. This is because different frequency components are transmitted with different delays. For the transmission of short wideband pulses with durations smaller 2 ns this is not acceptable. For the Vivaldi antenna the impulse response is short in comparison, but the group delay varies with radiation angle. This is a similar behavior to the direct path excess delay caused by a multipath channel described in Section 2.2. Depending on which radiation direction of the antenna was used for calibration the error can also be negative, causing too short distance estimates. A detailed investigation of the impact of angle dependent antenna impulse responses on UWB ranging accuracy is presented in Section 3.2.

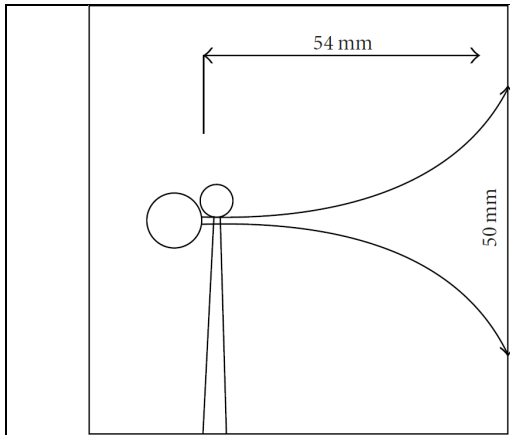


Figure 2.3. Layout of a Vivaldi antenna from [36].

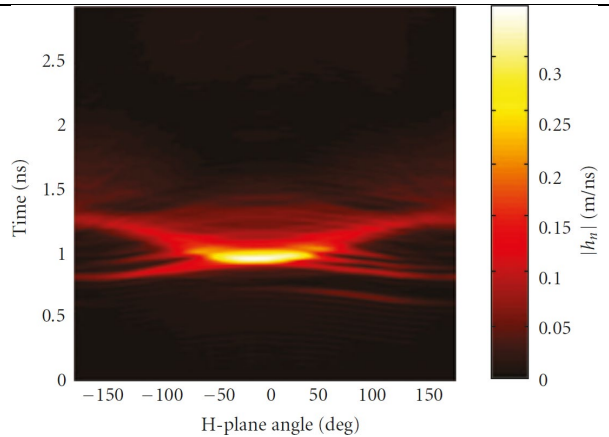


Figure 2.4. Measurement of the transient response envelope of a Vivaldi antenna versus angle and time for the horizontal plane and co-polarization from [36].

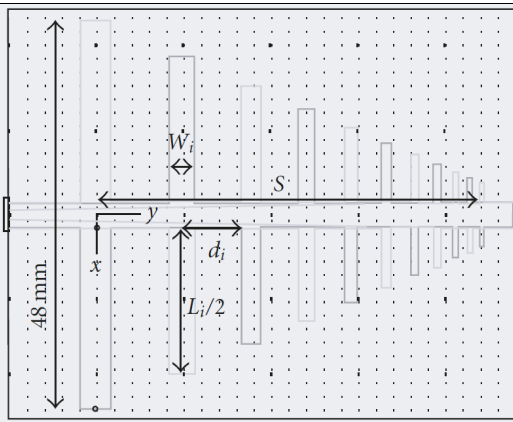


Figure 2.5. Layout of a log-periodic antenna from [36].

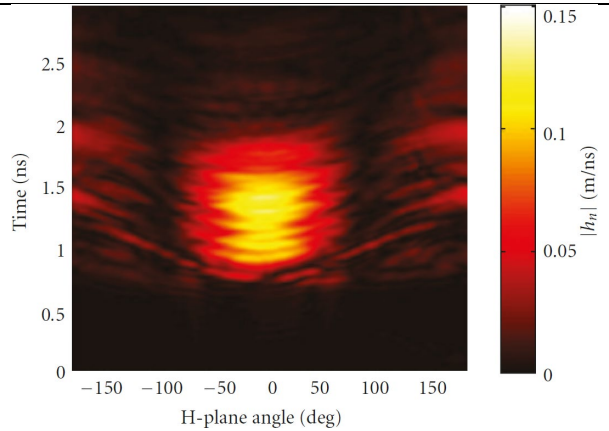


Figure 2.6. Measurement of the transient response envelope of a log-periodic antenna versus angle and time for the horizontal plane and co-polarization from [36].

2.3 Introduction to Mixed-Mode S-Parameters

Most people now about S-parameters, but mixed-mode S-parameters used to describe differential networks are often less understood, although they are of major importance for the characterization of devices which make use of differential signaling. In [37] the concept of mixed-mode S-parameters is being explained thoroughly. In this section, I provide a short summary with reference to [37], because mixed-mode S-parameters are heavily used in Section 4 for the characterization of differential networks. In Section Appendix B I provide a Matlab® implementation of generalized mixed-mode S-parameters, which is able to combine single-ended and mixed-mode ports in a single network. This is especially useful for describing networks like baluns or 180° hybrids.

A simple and very common differential network is a four port with two single-ended ports at the input and two single-ended ports at the output as shown in Figure 2.7. The two single-ended ports at the input (port 1 and port 2) can be paired as a mixed-mode port number 1. Accordingly, port 3 and port 4 at the output can be paired as a mixed-mode port number 2. It is important to note that the overall number of ports stays the same, as a mixed-mode port can be used for two different modes, and each mode is assigned to an individual port. The same approach is used in many electromagnetic simulation

environments, where a specific mode is mapped to an individual “virtual” port, although the physical port of the structure might be the same.

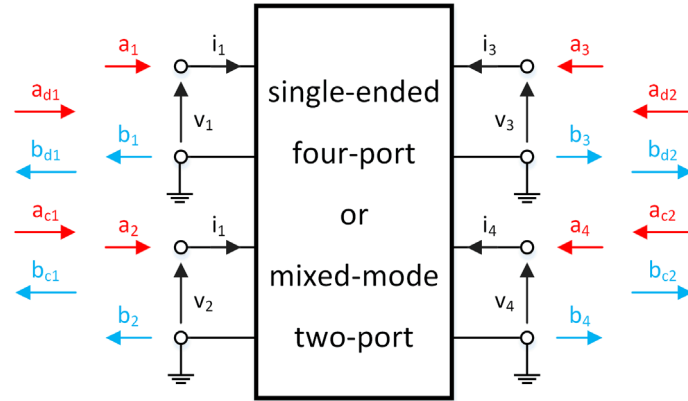


Figure 2.7. General network featuring either four single-ended ports or two mixed-mode ports. The left ports 1 and 2 as well as the mixed-mode port 1 are referenced as the input ports, while the right ports 3, 4 and mixed-mode port 2 are referenced as the output ports.

Following Figure 2.7 we can define currents and voltages for the mixed-mode ports as shown below. By looking at (2.3) we see that the differential voltages do not depend on the reference potential of the used ground. At a differential port, we assume that the current entering the network at one node leaves at the other node of the port, due to this the differential currents in (2.4) are defined as half the difference between the currents entering nodes 1 and 2. In (2.5) we defined the common-mode voltage as the average voltage on the two nodes of a port. We can observe that in contrast to the differential-mode voltage the common-mode voltage is still referenced to the reference potential of the ground. From this it also becomes obvious that the return current of the common mode flows through the ground terminal and the input current is the sum of the currents entering at both nodes of a port like defined in (2.6). In all further derivations I will assume a reference potential of v_0 equal to 0.

$$v_{d1} = (v_1 - v_0) - (v_2 - v_0) = v_1 - v_2 \quad (2.3)$$

$$v_{d2} = (v_3 - v_0) - (v_4 - v_0) = v_3 - v_4$$

$$i_{d1} = \frac{i_1 - i_2}{2} \quad (2.4)$$

$$i_{d2} = \frac{i_3 - i_4}{2}$$

$$v_{c1} = \frac{(v_1 + v_0) + (v_2 + v_0)}{2} = \frac{v_1 + v_2}{2} + v_0 \quad (2.5)$$

$$v_{c2} = \frac{(v_3 + v_0) + (v_4 + v_0)}{2} = \frac{v_3 + v_4}{2} + v_0$$

$$i_{c1} = i_1 + i_2 \quad (2.6)$$

$$i_{c2} = i_3 + i_4$$

Using the above definitions, we are able to define wave variables, which are needed for the definition of S-parameters. For better understanding [37] introduced a practical simplification which assumes that each pair of ports in the network is a symmetric coupled pair of transmission lines. This simplification is not limiting, because the length of such lines as reference lines of differential circuit ports may be arbitrarily short. In such a symmetric coupled transmission line, two modes can propagate (even mode, odd mode). At each terminal of such a line, the voltage and currents of both modes are referenced to ground. The resulting voltages and currents at different positions z along the line are superpositions of voltage waves and current waves of both modes, propagating in both

directions. In (2.7) I introduced a shorthand form of the incident and reflected voltage waves for even and odd mode. V_0^+ is an incident voltage wave while V_0^- is a reflected voltage wave. The variable x can either be e or o indicating if the wave either belongs to the even or odd mode. The variable γ_x is the propagation constant for the given mode and Z_{0x} is the characteristic impedance seen by the corresponding mode. The zeros in the indices indicate that voltages and currents are linked by the characteristic impedance. The superimposed voltage and current values along each of the single-ended lines are defined in (2.8) and (2.9).

$$v_x^\pm = v_x^\pm(z) = V_{0x}^\pm e^{\mp\gamma_x z} \quad x \in [\text{even}, \text{odd}] \quad (2.7)$$

$$i_x^\pm = i_x^\pm(z) = I_{0x}^\pm e^{\mp\gamma_x z} = \frac{V_{0x}^\pm}{Z_{0x}} e^{\mp\gamma_x z} \quad x \in [\text{even}, \text{odd}]$$

$$v_1(z) = v_e^+ + v_e^- + v_o^+ + v_o^- \quad (2.8)$$

$$v_2(z) = v_e^+ + v_e^- - v_o^+ - v_o^-$$

$$i_1(z) = i_e^+ - i_e^- + i_o^+ - i_o^- \quad (2.9)$$

$$i_2(z) = i_e^+ - i_e^- - i_o^+ + i_o^-$$

Using (2.3) to (2.9) the differential-mode and common-mode voltages and currents can be expressed as in (2.10) to (2.13).

$$v_d = v_d(z) = 2(v_o^+ + v_o^-) \quad (2.10)$$

$$i_d = i_d(z) = \frac{v_o^+ - v_o^-}{Z_{0o}} \quad (2.11)$$

$$v_c = v_c(z) = v_e^+ + v_e^- \quad (2.12)$$

$$i_c = i_c(z) = 2 \frac{v_e^+ - v_e^-}{Z_{0e}} \quad (2.13)$$

In agreement with conventional S-parameters the definitions of voltages, currents and characteristic impedances can be used to introduce wave variables corresponding to each of the modes as shown below. I used the definition of power waves as in [38].

$$a_d = a_d(z) = \frac{v_d + i_d Z_{Rd}}{2\sqrt{\text{Re}\{Z_{Rd}\}}} \quad (2.14)$$

$$b_d = b_d(z) = \frac{v_d - i_d Z_{Rd}^*}{2\sqrt{\text{Re}\{Z_{Rd}\}}} \quad (2.15)$$

$$a_c = a_c(z) = \frac{v_c + i_c Z_{Rc}}{2\sqrt{\text{Re}\{Z_{Rc}\}}} \quad (2.16)$$

$$b_c = b_c(z) = \frac{v_c - i_c Z_{Rc}^*}{2\sqrt{\text{Re}\{Z_{Rc}\}}} \quad (2.17)$$

Often used simplifications to these equations are the assumption that the reference impedances Z_{Rx} , which can be chosen arbitrarily as in the case of conventional S-parameters, are equal to the characteristic impedances of the used lossless transmission line Z_{0x} , which includes that they are real valued. As in the case of conventional S-parameters a scattering matrix can be defined for the incident and reflected differential-mode and common-mode waves as in (2.18) for the general case and in (2.19) for the four-port case presented in Figure 2.7.

$$\begin{bmatrix} \underline{b}_d \\ \underline{b}_c \end{bmatrix} = \begin{bmatrix} \underline{S}_{dd} & \underline{S}_{dc} \\ \underline{S}_{cd} & \underline{S}_{cc} \end{bmatrix} \begin{bmatrix} \underline{a}_d \\ \underline{a}_c \end{bmatrix} \quad (2.18)$$

$$\begin{bmatrix} b_{d1} \\ b_{d2} \\ b_{c1} \\ b_{c2} \end{bmatrix} = \begin{bmatrix} S_{dd11} & S_{dd12} & S_{dc11} & S_{dc12} \\ S_{dd21} & S_{dd22} & S_{dc21} & S_{dc22} \\ S_{cd11} & S_{cd12} & S_{cc11} & S_{cc12} \\ S_{cd21} & S_{cd22} & S_{cc21} & S_{cc22} \end{bmatrix} \begin{bmatrix} a_{d1} \\ a_{d2} \\ a_{c1} \\ a_{c2} \end{bmatrix} \quad (2.19)$$

The scattering matrices defined above can be used to gain insights into the behavior of a differential network, which would not be easy using conventional S-parameters. For example, the Parameter S_{cd12} describes how much of the power entering the mixed-mode port 2 as differential mode comes out at the mixed-mode port 1 as common mode. If all S_{cd} and S_{dc} terms are zero, one knows that no mode conversion is taking place in the network. As the differential-mode and common-mode voltages and currents defined in (2.10) to (2.13) are just linear combinations of the single-ended voltages and currents, a linear transformation between the derived conventional S-parameters and mixed-mode S-parameters also exists. How the transformation matrix is derived, is presented in [37]. In [37] also a method to calculate S-matrices of networks containing differential-mode ports, common-mode ports and single-ended ports is presented. The resulting matrices are called ‘‘Generalized Mixed-Mode Scattering Matrices’’. This allows to analyze networks like baluns or 180° hybrids which feature mixed-mode ports as well as single-ended ports. Although I do not provide the complete derivation the general shape of a generalized mixed-mode scattering matrix is shown in (2.20) for a n-port network with p mixed-mode ports and $n - 2p$ single-ended ports. Remember that each mixed-mode port consists of two paired single-ended ports. The upper left corner of the generalized mixed-mode scattering matrix \hat{S} contains the mixed-mode S-parameters as derived before. These for matrices have a size of $p \times p$ as shown in (2.21). Accordingly, (2.22) shows the block matrices \hat{S}_{ds} , \hat{S}_{sd} , \hat{S}_{cs} and \hat{S}_{sc} used to describe the behavior between mixed-mode ports and single-ended ports. \hat{S}_{ss} has the shape of a conventional S-parameter matrix and links single-ended ports to single-ended ports as presented in (2.23).

$$\hat{S} = \begin{bmatrix} \hat{S}_{dd} & \hat{S}_{dc} & \hat{S}_{ds} \\ \hat{S}_{cd} & \hat{S}_{cc} & \hat{S}_{ce} \\ \hat{S}_{sd} & \hat{S}_{sc} & \hat{S}_{ss} \end{bmatrix} \quad (2.20)$$

$$\begin{aligned} \underline{\hat{S}}_{dd} &= \begin{bmatrix} \hat{S}_{dd11} & \cdots & \hat{S}_{dd1p} \\ \vdots & \ddots & \vdots \\ \hat{S}_{ddp1} & \cdots & \hat{S}_{ddpp} \end{bmatrix} & \underline{\hat{S}}_{dc} &= \begin{bmatrix} \hat{S}_{dc11} & \cdots & \hat{S}_{dc1p} \\ \vdots & \ddots & \vdots \\ \hat{S}_{dcp1} & \cdots & \hat{S}_{dcpp} \end{bmatrix} \\ \underline{\hat{S}}_{cc} &= \begin{bmatrix} \hat{S}_{cc11} & \cdots & \hat{S}_{cc1p} \\ \vdots & \ddots & \vdots \\ \hat{S}_{ccp1} & \cdots & \hat{S}_{ccpp} \end{bmatrix} & \underline{\hat{S}}_{cd} &= \begin{bmatrix} \hat{S}_{cd11} & \cdots & \hat{S}_{cd1p} \\ \vdots & \ddots & \vdots \\ \hat{S}_{cdp1} & \cdots & \hat{S}_{cdpp} \end{bmatrix} \end{aligned} \quad (2.21)$$

$$\begin{aligned} \underline{\hat{S}}_{ds} &= \begin{bmatrix} \hat{S}_{ds11} & \cdots & \hat{S}_{ds1(n-2p)} \\ \vdots & \ddots & \vdots \\ \hat{S}_{dsp1} & \cdots & \hat{S}_{dsp(n-2p)} \end{bmatrix} & \underline{\hat{S}}_{sd} &= \begin{bmatrix} \hat{S}_{sd11} & \cdots & \hat{S}_{sd1p} \\ \vdots & \ddots & \vdots \\ \hat{S}_{sd(n-2p)1} & \cdots & \hat{S}_{sd(n-2p)p} \end{bmatrix} \\ \underline{\hat{S}}_{cs} &= \begin{bmatrix} \hat{S}_{cs11} & \cdots & \hat{S}_{cs1(n-2p)} \\ \vdots & \ddots & \vdots \\ \hat{S}_{csp1} & \cdots & \hat{S}_{csp(n-2p)} \end{bmatrix} & \underline{\hat{S}}_{sc} &= \begin{bmatrix} \hat{S}_{sc11} & \cdots & \hat{S}_{sc1p} \\ \vdots & \ddots & \vdots \\ \hat{S}_{sc(n-2p)1} & \cdots & \hat{S}_{sc(n-2p)p} \end{bmatrix} \end{aligned} \quad (2.22)$$

$$\underline{\hat{S}}_{ss} = \begin{bmatrix} \hat{S}_{ss11} & \cdots & \hat{S}_{ss1(n-2p)} \\ \vdots & \ddots & \vdots \\ \hat{S}_{ss(n-2p)1} & \cdots & \hat{S}_{ss(n-2p)(n-2p)} \end{bmatrix} \quad (2.23)$$

A Matlab® implementation of a transformation between conventional S-parameters to generalized mixed-mode scattering S-parameters is presented in Section Appendix B.

3 System Level Performance Analysis

Traditionally the performance of communication systems is estimated using analytical methods, called link budget calculations. As mentioned in the introduction UWB-IR hardly allows analytical modelling of network simulations for wide ranges of channel models or receiver architectures, especially if multi-user interference is present on multipath channels. One of the reasons for this is that the characterization of multi-user interference with a Gaussian model was proven to be incorrect. Most of the existing analytical models, like the ones presented in [1], [2], [7], [8] and [9] are limited to specific modulation and channel types making comparisons between them difficult. A way to circumvent the limitations imposed by analytical methods is to utilize simulation environments as they were presented in [3], [4] and [5]. These simulation environments apply heavy simplifications like the approximation of pulses with a triangular shape. And although ranging is the most common use case for UWB-IR, none of the aforementioned simulation environments allows to analyze the ranging accuracy.

An ultra-wideband physical layer system simulation environment, for the remainder of this thesis abbreviated as UWB PHY Sim, had been developed by the author and first results were presented in [39]. This UWB PHY Sim can simulate the performance of a whole UWB system, including key characteristics like bit error rate, package error rate and ranging error. To simulate the performance of a whole UWB system, the physical layer (PHY) of the whole system needs to be modeled, which is a demanding task considering the multitude of parameters. Many of those parameters are not inherent to the UWB device itself but are imposed by the environment. Examples are the parameters of multipath channels or the presence of interference. Nevertheless, they need to be included in the system simulation as they significantly influence the performance of the whole system. In the next section I summarize the implementation of this system.

3.1 The Simulation Environment

I used the Matlab® framework and its object-oriented programming capabilities to group the building blocks of the UWB PHY Sim in different classes. Inheritance is used to define interfaces to each class, allowing to develop multiple models for each part of the simulation independently. The parallel processing capabilities of Matlab® are utilized to deal with the rather long simulation times. The simulation time for a single UWB frame on one core of an average PC using an Intel® i5 is between 15 and 60 seconds. Parallel computing on multiple cores or even workstations can be used to shorten simulation times, as an arbitrary number of frames can be calculated in parallel. A single simulation run simulates the transmission of a single frame. For handling input and output data an SQLite® database (DB) is used, enabling access to simulation data from different platforms. Figure 3.1 summarizes all building blocks of the simulation environment and their connections to the database. In the following sub-sections the functionality of each building block will be discussed in detail.

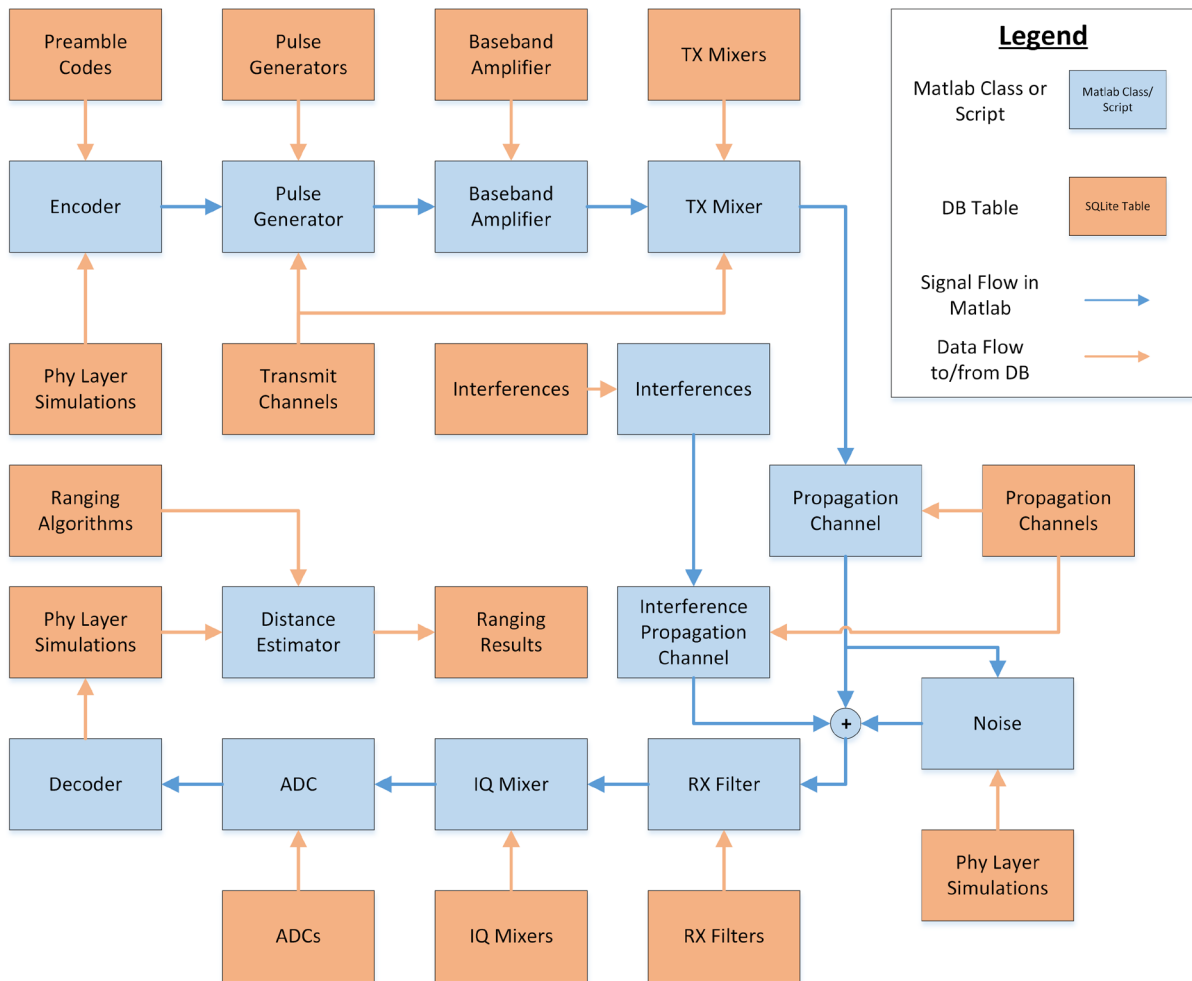


Figure 3.1. Block diagram showing the structure of the UWB physical layer simulation environment (UWB PHY Sim). Blue blocks indicate Matlab® classes, orange blocks represent tables in a SQLite database. Blue arrows indicate the program flow in the Matlab® code, orange arrows show how data is transferred to and from the database as I showed in [39].

3.1.1 Transmitter

The Transmitter summarizes all building blocks resembling the transmitting UWB device, except the antenna. These are the encoder, baseband pulse generator, amplifier and mixer. The output of the transmitter is located at the reference plane to the antenna. Therefore, the output signal of the transmitter is the signal that is fed to the antenna. Each frame generated by a transmitter is split into short time intervals called chips. Each chip may contain a single pulse. In [22] the peak pulse repetition frequency (PRF) was defined to be 499.2 MHz. This frequency corresponds to the highest rate at which a transmitter may emit pulses. The reciprocal value of the PRF defines the duration of a chip with about 2 ns.

a. Encoder

The encoder is the first block in the transmitter and the whole signal flow diagram (see Figure 3.1) and it reflects what is proposed in [22]. It generates the ternary symbol sequence which is passed to the pulse generator. This sequence consists of the synchronization header (SHR), physical header (PHR) and data field. In a first step, the SHR is generated by repeating a 31 or 127-bit preamble code. The logical channel for the transmission defines the applied preamble code. These codes are designed to feature a minimum cross correlation and can be found in [22]. The ternary code defines the polarity of

the pulses in the SHR, in addition a spacing of 4, 16 or 64 chips is inserted between pulses in the SHR. A start-of-frame delimiter symbol signals the end of the SHR and is followed by the physical header and subsequently the data field. Forward error correction coding in the form of an inner block and optional outer convolutional code is applied to the physical header and data field. A single error correction double error detection (SECDED) block code is applied to the PHR, while the payload data is Reed-Solomon encoded. The convolutional encoder uses a systematic code with code rate $\frac{1}{2}$. The PHR and data field are coded for burst position modulation with binary phase shift keying (BPM-BPSK). The output of the encoder is a vector with one element for each chip in a frame. The bursts and their positions are calculated for each symbol using a shift register defined in [22] with the used preamble code as initial value. This is supposed to provide additional interference rejection between logical channels. Detailed information on the encoding and modulation scheme can be found in [22].

b. Pulse Generator

Using the ternary coded vector from the encoder the pulse generator creates the “analog” baseband signal. Of course, there is no real analog signal in Matlab®, but if we choose a sampling rate high enough relative to the maximum signal frequency this is not a problem. Please consider that due to mixing and non-linearity the highest signal frequency might be much higher than the center frequency of the signal. To calculate the baseband signal, the ternary coded vector is up sampled to the desired sample rate of the “analog” signal and convolved with the chosen pulse shape. Pulse shapes are provided as parameterized analytical expressions and stored in the database. As a parameter these expressions take the pulse duration T_p . In this way, the bandwidth of the signal can be changed without changing the shape of the pulse. Examples for this are given in (3.1) for a root raised cosine pulse with a roll-off factor of 0.5 and (3.2) presenting a Gaussian pulse shape resulting in a bandwidth occupation similar to the root raised cosine pulse shape for same values of T_p .

$$s_p(t) = \frac{2}{\pi\sqrt{T_p}} \frac{\cos(1.5 \pi t/T_p) + \frac{\sin(0.5 \pi t/T_p)}{2 t/T_p}}{1 - (2 t/T_p)^2} \quad (3.1)$$

$$s_p(t) = \exp\left(-\frac{1}{2}\left(\frac{2.4 \cdot t}{T_p}\right)^2\right) \quad (3.2)$$

c. Amplifier and Mixer

In a real device, the driver amplifier would be found after the mixer. For the sake of computational efficiency a complex baseband amplifier model is used before the mixer instead. A memory polynomial amplifier model based on [40], [41] and [42] utilizing piecewise linear approximation and real measurement data was used. After the amplifier block, the mixer block calculates a band pass signal from the complex baseband signal. At this stage, imperfections like local oscillator mismatch or drift are added to the signal. In (3.3) the equation used in a simple mixer model is presented. The output vector \underline{y} is calculated from the complex baseband input signal vector \underline{x} , the center frequency f_c , the time vector \underline{t} and the phase vector $\underline{\varphi}$. The phase $\underline{\varphi}$ can either be a vector or scalar, depending if an instability of the local oscillator needs to be simulated or not. A constant frequency offset can be achieved by supplying different center frequencies to the transmitter and receiver blocks.

$$\underline{y} = \sqrt{2} A [\cos(2\pi f_c \underline{t} + \underline{\varphi}) \text{Re}(\underline{x}) - \sin(2\pi f_c \underline{t} + \underline{\varphi}) \text{Im}(\underline{x})] \quad (3.3)$$

3.1.2 Channel and Antennas

Due to the inability to separate antennas and channels described in Section 2.2.2, the common approach to treat them as one entity was used. The band pass signal at the output of the transmitter is convolved with the channel impulse response of a given channel. The modular structure of the UWB PHY Sim allows different types of channel models to be used for this task. Also measured or pre-calculated channel impulse responses can be imported from the database. A useful channel model for testing and simulation of simple propagation scenarios (e.g. tow-ray channels) is shown in (3.4) where the coefficients a_k and delays τ_k are provided by the user in terms of database entries. The database entries can either be numeric values or Matlab® expressions like rand(), which can be used to generate random values for each realization of the channel.

$$h[n] = \sum_k a_k \delta[n - \tau_k] \quad (3.4)$$

Because the time lags τ_k can be chosen arbitrarily by the user or are generated by some third-party software or script, they most likely will not coincide with the sample interval used in the simulation environment. For the simple channel model described in (3.4) each multipath component is shifted towards the nearest neighboring sample to solve this issue. If two components are shifted to the same sample, they are added in a way to preserve the total energy of the channel impulse response. The reason this approach was used is that this channel model is used for testing of the simulation environment or simulation of two-ray channels. Thus, preserving the magnitudes of the individual components helps the user to understand the simulation. A second more realistic channel model was implemented based on [43], [44] and [33]. This channel model uses exponentially decaying clusters first described by Saleh and Valenzuela in [45] and “diffuse” clusters with a longer decay time constant. Parameter sets for residential, office, outdoor and industrial environments are included. For each environment line-of-sight (LOS) and non-line-of-sight (NLOS) parameter sets are specified in [44]. For this type of channel model, the coefficients of the complex channel are aligned to the samples of the simulation using the linear interpolation function of Matlab® on the sample vector. After alignment, the signal is convolved with the channel.

3.1.3 Noise

For the implemented transmitter system, all components showed a noiseless behavior. After the transmitter output signal was convolved with the impulse response function of the antenna and the channel, white Gaussian noise is added to the resulting signal. Adding the noise at this stage, allows to specify the level of signal-to-noise ratio (SNR) at the receiver desired for the simulation. By this approach I am neglecting the influence of non-Gaussian noise components generated within the transmitter (for example, through the transformation by the nonlinear amplifier). Only their Gaussian-like effect is represented appropriately. It is much more efficient to add an amount of noise at one point instead of specifying the noise figures for all components. The calculations needed to achieve the desired SNR are presented in equations (3.5) to (3.11). In (3.5) the power of the received signal vector \underline{x} inside the frequency band specified by \underline{f} is calculated using the Matlab® function bandpower(). The desired noise power $P_{v,desired}$ to achieve the given SNR is calculated in (3.7). The vector containing the noise signal and its in-band power is then derived in (3.8) and (3.9), before its power is scaled in (3.10) to meet the SNR specification. In a last step, the noise signal is added to the received signal as indicated by (3.11).

$$P_x = \text{bandpower}(\underline{x}, f_{\text{sample}}, \underline{f}); \quad (3.5)$$

$$\underline{f} = [f_{\text{lower}} \ f_{\text{upper}}] \quad (3.6)$$

$$P_{v,\text{desired}} = \frac{P_x}{10^{\text{SNR}/10}} \quad (3.7)$$

$$\underline{v}' = \text{randn}(N) \quad (3.8)$$

$$P_v = \text{bandpower}(\underline{v}', f_{\text{sample}}, \underline{f}) \quad (3.9)$$

$$\underline{v} = \underline{v}' \cdot \sqrt{\frac{P_{v,\text{desired}}}{P_v}} \quad (3.10)$$

$$\underline{s} = \underline{x} + \underline{v} \quad (3.11)$$

3.1.4 Interference

Not only noise but also interference can be added to the signal. For my investigations the most important kind of interference are UWB signals on different logical or physical channels. Based on the modular design of the UWB PHY Sim, different sources of interference like strong continues wave signals, WiFi™ and Bluetooth® can be added as well if needed. The easiest way to achieve this is to use built in Matlab® functions for signal generation. As the generation of an UWB signal already exists in the simulation environment, it is straightforward to create additional interference signals which are then added to the payload signal. A different preamble, center frequency and channel can be chosen for this interference signal. Also, a percentage for the overlap of the two UWB frames must be specified, ranging from -90% to 100% where a negative overlap specifies an overlap at the beginning of the signal frame while a positive overlap specifies an overlap at the end of the signal frame as shown in Figure 3.2. A uniformly distributed random variable can be added to the specified overlap value to create some randomness, as the overlap in a real system is a pure random variable. As by now, the simulation environment only supports the simulation of interference signals with same frame length and parameters. Only the logical channel (preamble code), physical channel (center frequency and bandwidth) and propagation channel can be different for the interference signal. This resembles the use case of interference between multiple identically UWB devices. Of course also the signal-to-interference ratio (SIR) can be defined by the user, this is independent of the used propagation channel models for signal and interference. If the user wishes a dependency of the SIR on the used propagation channels this can be achieved by a calculation of the SIR according to the selected channel models before the simulation.

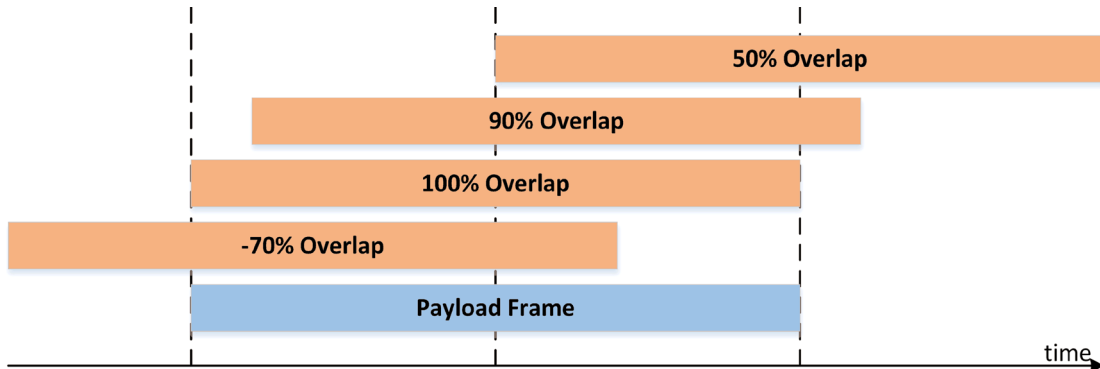


Figure 3.2. Visualization of different overlap factors for UWB interference simulation.

3.1.5 Receiver

The first stage in the receiver is the receive filter (RX filter) which performs band pass filtering. This filtering stage prevents the mixing of unwanted frequency components in the following IQ-mixer. The specifications of a filter often only consist of maximum passband ripple, minimum stopband attenuation and transition bandwidth. Therefore, it is hard to choose an appropriate filter type and deliver results that can be compared to each other. Depending on the chosen filter type and parameters (for example, ripple, out-of-band attenuation, transition bandwidth), filter frequency responses can be vastly different. Even if simulations of all common filter types are performed, their ideal frequency responses do not match the observed behavior in a real system. This led me to the decision to use zero phase filtering with filters of high order and frequency responses that match the requirements for passband ripple, stopband attenuation and transition bandwidth as closely as possible. These are still not the results a real system would show, but at least the simulated results are repeatable and comparable. An example filter response is shown in Figure 3.3. As it can be observed the generated filter response follows the filter mask with some degree of freedom in the transition band. Because zero phase filtering is utilized the phase is not affected by this filter. The user may also use a custom filter response instead of the presented default implementation.

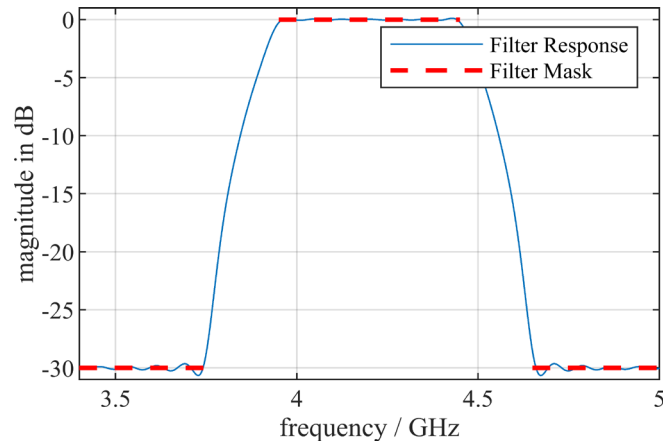


Figure 3.3. Filter response of the RX filter in the PHY Sim. Used input parameters are a center frequency of 4.2 GHz, bandwidth of 500 MHz, transition bandwidth of 200 MHz and stop-band attenuation of 30 dB.

After the RX filter the signal is down-converted using an IQ-mixer to get the complex baseband signal at the receiver. This mixer can either be ideal or exhibit imperfections like magnitude or phase imbalance, as well as LO mismatch or drift. In equation (3.12) the voltage gains for each path of the IQ demodulator are calculated, G being the overall gain and Δ_G being the gain imbalance between the paths. Equation (3.13) shows how the received signal vector x is split into an I-channel and Q-channel. The phase imbalance between the channels can be set with Δ_φ . A drift or offset of the local oscillator equally impacting both channels can be introduced by setting the center frequency f_c or phase vector φ . As in the RX filter the signal is then filtered by a high order arbitrary magnitude response low pass filter for image rejection, or a custom filter response supplied by the user.

$$V_I = 10^{G/20}; V_Q = 10^{(G-\Delta_G)/20} \quad (3.12)$$

$$\underline{y}_I = V_I \cdot \left(\cos \left(2\pi f_c \underline{t} + \underline{\varphi} \right) \cdot \underline{x} \right); \underline{y}_Q = V_Q \left(\sin \left(2\pi f_c \underline{t} + \underline{\varphi} + \Delta_\varphi \right) \cdot \underline{x} \right) \quad (3.13)$$

Subsequently the two channels are sampled in the ADCs. This sampling process can be influenced by an adjustable value of aperture jitter. To simulate aperture jitter linear interpolation is used to estimate points which do not coincide with existing samples. The ADCs do not only perform sampling, but also quantization. This quantization is done according to a quantization curve, providing the ability to simulate offsets, gain errors, differential non-linearity and integral non-linearity. The two resulting

vectors with I and Q samples are then passed to the decoder, which performs the steps shown in Figure 3.4.

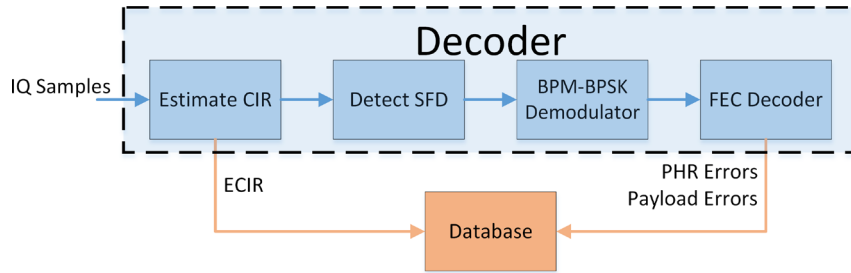


Figure 3.4. Processing steps in the decoder block of the PHY Sim. [39]

First the estimated channel impulse response (ECIR) is calculated. For this task, the cross-correlation of the known preamble and the received signal is calculated. Because the synchronization header consists of repetitions of the same symbol, the cross-correlation function also repeats with the symbol interval. This is used to reduce the noise floor by calculating the average of all repetitions in the cross-correlation function, resulting in improved dynamic range of the ECIR but without influencing the impact of multipath propagation. The averaged cross-correlation function is used as an estimate of the real channel impulse response (CIR). The formula for the cross-correlation R_{yx} of a linear time invariant system with impulse response h , input signal x and output signal y is shown in (3.14). If the autocorrelation R_{xx} of the input signal approaches a Dirac delta distribution the expression in (3.14) can be rewritten like in (3.15), showing that in this case the cross correlation function is identical to the channel impulse response scaled by some factor. This is achieved by applying the sampling property of a Dirac delta distribution as in (3.16). Although the autocorrelation functions of UWB signals are not ideal Dirac delta distributions, the convolution of their narrow autocorrelation function with the CIR can be used as an ECIR. At this point, I would like to mention that R_{xx} limits the ability to resolve individual multipath components even if all other system components are ideal.

$$R_{yx}(\tau) = h(\tau) * R_{xx}(\tau) \quad (3.14)$$

$$R_{yx}(\tau) = h(\tau) * p_0 \delta(\tau) = p_0 h(\tau) \quad (3.15)$$

$$\int_{-\infty}^{\infty} f(\tau) \delta(\tau - t) d\tau = f(t) \quad (3.16)$$

After the calculation of the ECIR, the data part of the frame can be demodulated using the burst and hopping sequences derived from the known preamble code. For this task, the received signal is split into parts, each having the length of one symbol, starting after the start-of-frame delimiter (SFD). For each received symbol, the correlation with the expected burst is calculated. As shown in Figure 3.5 the position of the burst in the frame indicates a transmitted “0” or “1” data bit, while the polarity of the burst is used in the following Viterbi decoder as parity information, yielding a Burst Position Modulation with Binary Phase Shift Keying (BPM-BPSK). Because a single burst is shorter than the range of valid burst positions, burst position hopping is used to gain additional multi-user interference rejection. For additional performance, soft decisions are used in the Viterbi decoder if bursts appear at unexpected positions. Following the Viterbi decoder, the SECDED encoded PHR and RS encoded payload is decoded. In a last step the bit errors in the PHR and payload are calculated by comparison of the received data with the transmitted data.

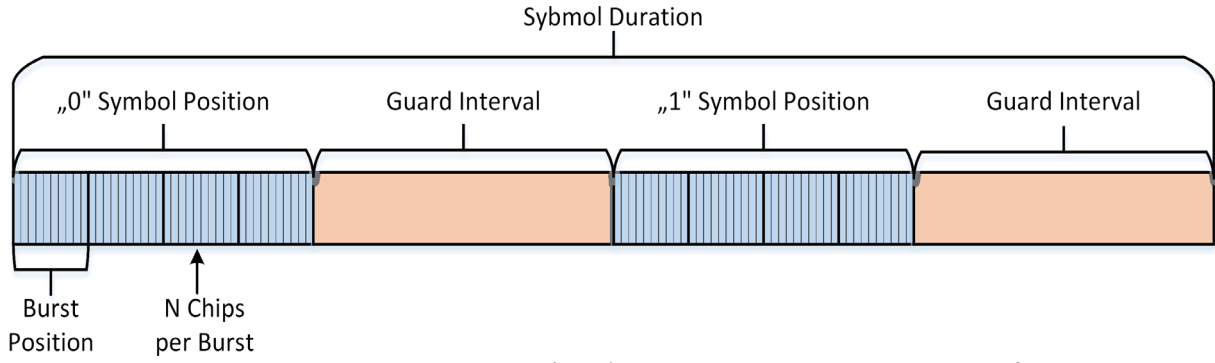


Figure 3.5. Burst Position Modulation (BPM) with Burst Position Hopping symbol format.

3.1.6 Distance Estimation

As described in the previous section the output of the simulation is the ECIR and number of bit errors. For ranging applications, we require also an estimation of the distance. To compare different ranging algorithms efficiently the stored ECIRs are used as an input, instead of running a full simulation run for each individual ranging result. In the UWB PHY Sim two default ranging algorithms are implemented, which are a leading-edge detection algorithm with a fixed threshold and another leading-edge detection algorithm with a threshold relative to the noise floor. Using ECIRs normalized to a maximum value of one, the threshold defines the lowest possible value of a direct path compared to the maximum value that can still be detected. A fixed threshold is relative to the maximum value of the ECIR, while a noise dependent threshold depends also on the dynamic of the ECIR. The noise dependent threshold γ is calculated in (3.17). In (3.18) \bar{v} is the arithmetic mean of the noise in the ECIR, N being the length of the ECIR and k being an index after which no multipath components are expected or they are attenuated enough to be neglected. λ is the threshold multiplier in a range from 0 to 1 and γ the resulting threshold. All values are in linear scale. By using the stated equations, a threshold multiplier of 0.5 would place the threshold exactly in the middle between the average noise floor and peak value of the ECIR.

$$\gamma = (1 - \bar{v}) \cdot \lambda + \bar{v} \quad (3.17)$$

$$\bar{v} = \frac{1}{(N - k + 1)} \sum_{n=k}^N ECIR(n) \quad (3.18)$$

3.1.7 Database

Figure 3.6 shows the architecture of the employed database with all tables and columns. The table "Phy Layer Simulations" is the centerpiece of the database. This table is directly related to a single simulation run of the UWB PHY Sim. As presented in Figure 3.1, each block of the simulation has its own corresponding table to store its input parameters. If there are more than one possible model for a block the corresponding table stores the type information of the model to be used. For example, the table "Propagation Channels" contains a column "model_type". With this parameter, the user can choose between the default model using discrete multipath components and the IEEE channel model. The difference between the two was explained in Section 3.1.2. As interface between Matlab® and the SQLite database a third party Matlab® library called MKSQLite [46] is used. This library is written in C++ and provides much better performance than the SQLite connector included within Matlab®.

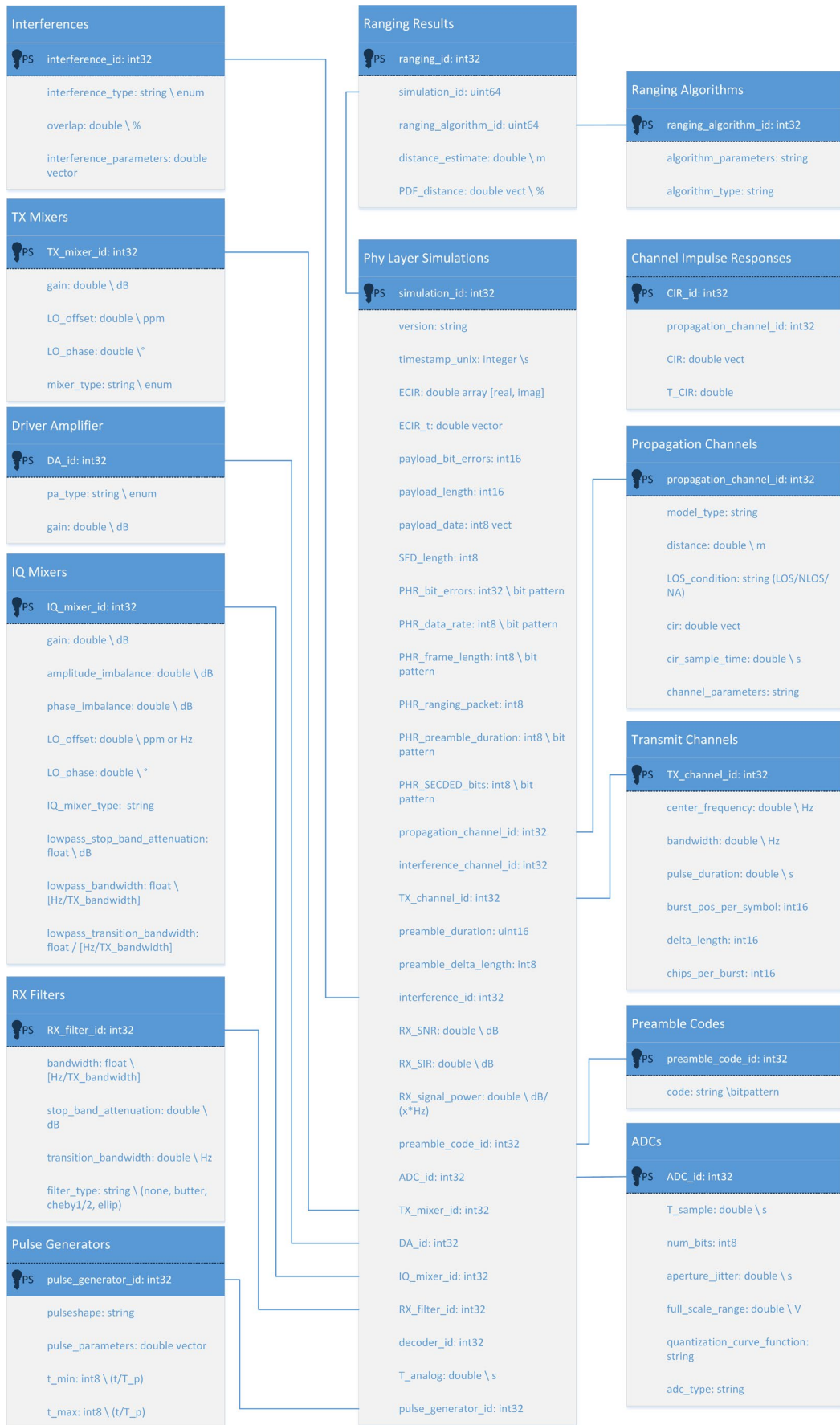


Figure 3.6. Database UML diagram showing all tables and parameters stored in the database.

3.2 Impact of Antenna Angle Dependencies

After providing a comprehensive overview on the UWB PHY Sim and its implementation, I will apply this simulation environment to investigate the ranging accuracy of such systems. In this context, I was interested to evaluate the influence of the antenna on the ranging performance. Based on the measurement results of two different antennas, multiple commonly used antenna characteristics were related to the ranging error of an UWB system [47]. Especially for UWB-IR antenna designers came up with different figures of merit like the full width at half maximum (FWHM), RMS delay spread, ringing duration, peak value, group delay and fidelity factor [36] [48] [49] [50] [51]. With the help of these parameters a designer should be able to estimate the impact of an antenna on UWB system performance. To verify this approach, I compare the mentioned parameters with results obtained from the UWB PHY Sim.

3.2.1 Antenna Designs and Measurement Setup

To investigate the impact of antennas on the UWB-IR ranging accuracy, I designed and manufactured two planar UWB antennas using 1.55 mm RO4350B substrate. The first antenna, presented in Figure 3.7, is an omnidirectional antenna that is optimized to be as small as possible without the need of discrete components. It is based on the design proposed in [52]. An optimization of the parameters was performed using CST Studio Suite®. Figure 3.8 shows the layout of the second antenna, which was inspired by the designs presented in [53] and [54]. Different to [53] the patch is positioned exactly on the symmetry line of the parabolic ground plane cutout. In addition, the parabolic function for the cutout is inclined by 45° with reference to the feeding line. Combined with an eccentric microstrip feed this design features a good directivity and high bandwidth. Another advantage over the design presented in [53] is that the main lobe is always pointing in the same direction, independent of the input signal frequency. In [53] the eccentrically placed patch causes a sweep of the main lobe with frequency.

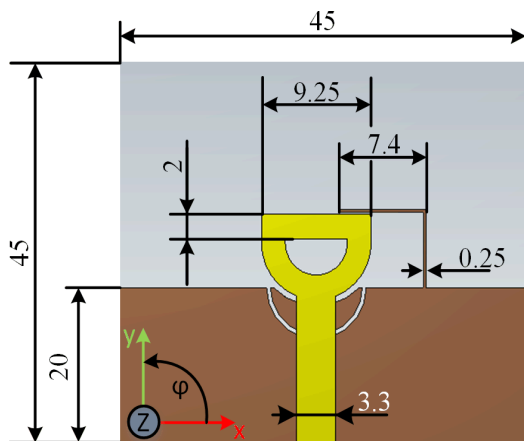


Figure 3.7. Layout of the designed omnidirectional UWB antenna [47].

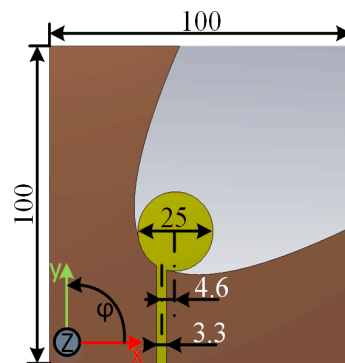


Figure 3.8. Layout of the designed directional UWB antenna [47].

Both antennas were characterized in an anechoic chamber using a R&S® ZVA64 Vector Network Analyzer (VNA) with appropriate calibration. For the employed calibration procedure, two identical reference antennas and a calibration kit for the VNA are needed. First, a calibration is performed at the end of the SMA cables connected to the VNA, shifting the reference plane of the measured S-parameters to the input ports of the antennas. The measured S_{21} is the transfer function from the antenna under test (AUT) to the reference antenna. (3.19) shows the relationship of the measured S_{21} and the antenna parameters. Please note that all presented equations are simplified and only account

for the co-polarization parts of the parameters, this approach is appropriate if the polarization purity of the reference antennas is adequate. A detailed explanation, including complete analytical derivations, of this calibration procedure can be found in [36]. By using a second identical reference antenna instead of the AUT, (3.19) can be rewritten to derive the frequency response of the reference antenna as in (3.20). This is possible because the distance r_{12} between the antennas as well as the propagation velocity c is known, and S_{21} is the measured variable. Once the frequency response of the identical reference antennas is known, the frequency response H_{AUT} of the AUT can be calculated using (3.19).

$$S_{21}(\omega, \varphi, \theta) = \frac{U_{RX,2}(\omega, \varphi, \theta)}{U_{TX,2}(\omega, \varphi, \theta)} = H_{ref}(\omega, \varphi_0, \theta_0) H_{AUT}(\omega, \varphi, \theta) \frac{j\omega}{2\pi r_{12} c} e^{-j\omega r_{12}/c} \quad (3.19)$$

$$H_{ref}(\omega, \varphi, \theta) = \sqrt{\frac{2\pi r_{12} c}{j\omega} S_{21}(\omega, \varphi, \theta) e^{j\omega r_{12}/c}} \quad (3.20)$$

For the UWB PHY Sim the channel response in time domain is needed. Usually the Inverse Fast Fourier Transformation (IFFT) is used to perform the conversion from frequency to time domain, but for this the frequency grid of the frequency domain data needs to start at DC. As this is typically not the case for data produced by VNA measurements, often a zero padding down to DC is performed, given that the grid is chosen in a way that a zero padding with equally spaced samples yields a sample exactly at DC. If this is not the case, the time domain signal will be complex after the IFFT. Often this fact is neglected, and the time domain signal is “corrected” by using only its real value. In my opinion this is not a correct way of handling this problem, as no inverse conversion to the same frequency domain representation is possible after taking the real part of the signal and information of the signal is intentionally neglected. In fact, I only know of two methods to handle this issue correctly. One is to perform an interpolation in the frequency domain to enforce a frequency grid that can be extended to DC, the second method which was used for this thesis is to employ the Chirp Z-transformation (CZT) and its counterpart the Inverse Chirp Z-transformation (ICZT). Details on the CZT can be found in the appendix in Section Appendix A. The angle dependent time domain impulse responses in this section are therefore calculated using the ICZT as indicated in (3.21).

$$h_{AUT}[n, \varphi, \theta] = ICZT(H_{AUT}[w, \varphi, \theta]) \quad (3.21)$$

3.2.2 Measurement Results

The matching of the antennas was measured using a VNA. Results for the simulated and measured return loss of the antennas are presented in Figure 3.9. Measurements and simulations agree quite well, although for return losses below 15 dB some differences can be observed. The omnidirectional antenna achieves a matching better than 10 dB between 3 GHz and 8.5 GHz. The directional antenna was able to achieve this matching performance over the frequency range from 2.5 GHz to 9.5 GHz. A comparison of the simulated and measured radiation patterns for discrete frequencies is summarized in Figure 3.10 and Figure 3.11. The coordinate system for all plots is the same as the one introduced in Figure 3.7 and Figure 3.8. The omnidirectional antenna shows a difference of 12 dB between maximum and minimum directivity, except for some small regions. For the directional antenna, a maximum directivity of approximately 12 dBi in the frequency range of 6.5 GHz and above was achieved. For lower frequencies, the maximum directivity was about 9 dBi.

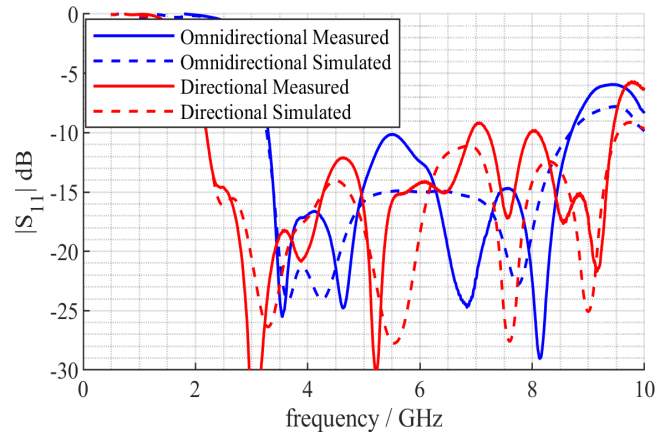


Figure 3.9. Simulated and measured return loss of both antennas [47].

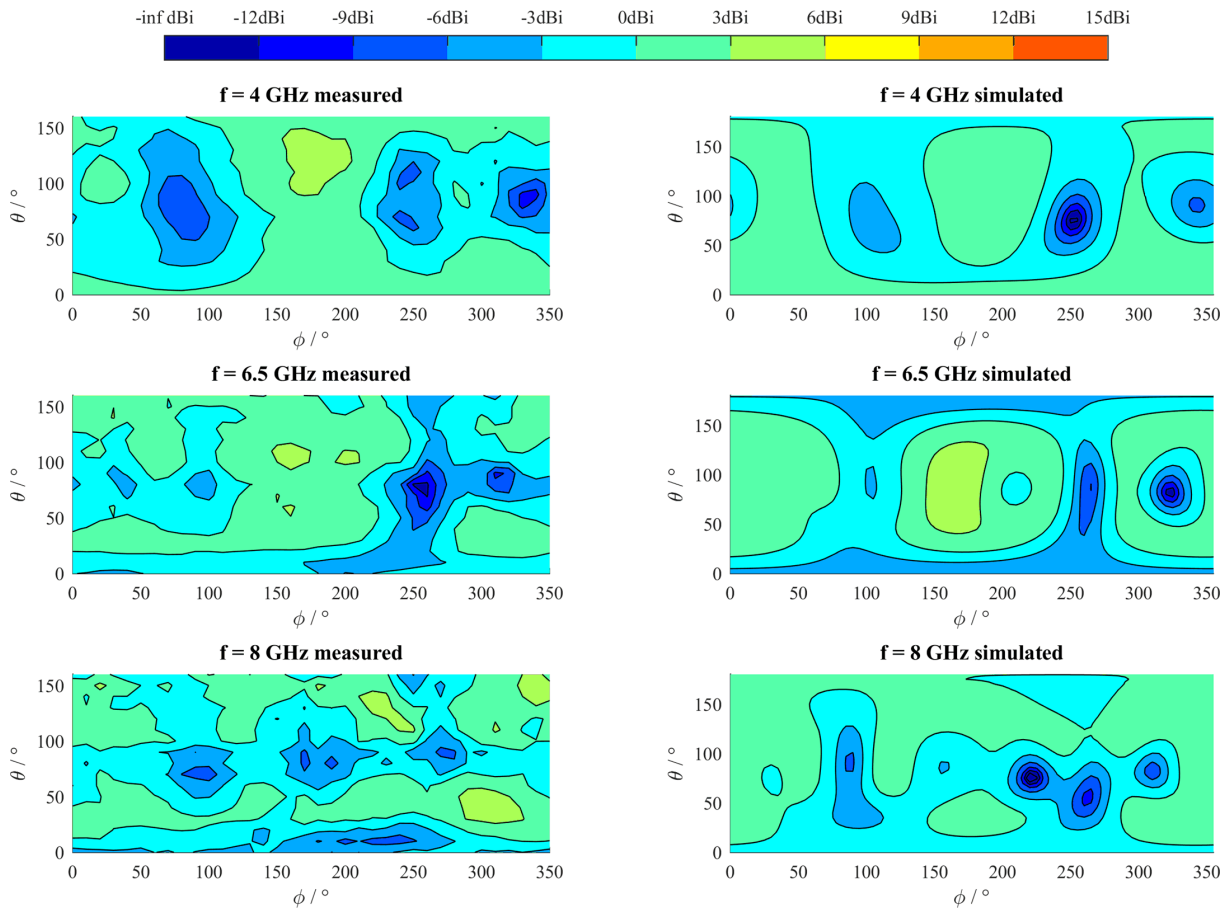


Figure 3.10 Directivity of the omnidirectional antenna [47].

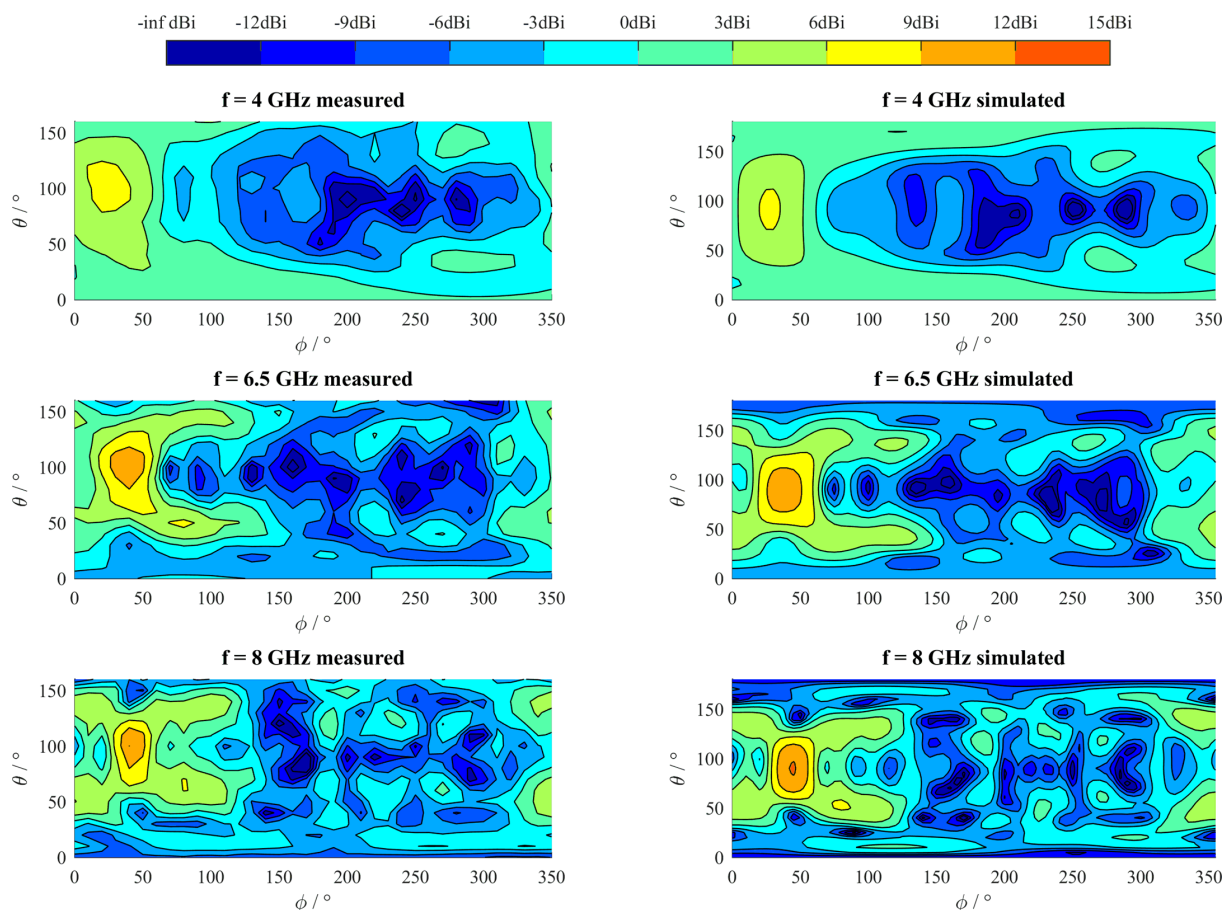


Figure 3.11. Directivity of the directional antenna [47].

The transient parameters of the antennas' impulse responses are presented in Figure 3.12 to Figure 3.17. These graphs highlight the transient effective directivity of each antenna for absolute, horizontal and vertical polarization values. Like the transient effective gain [36], the transient effective directivity is calculated using the impulse responses of the antennas. Figure 3.10 and Figure 3.11 show the directivity of each antenna if they are excited with a continuous wave signal. If the antennas are tested using a Dirac impulse, the transient effective directivity can be observed. As it will be discussed later, neither of these two excitation signals (CW, Dirac) represents a real use case for UWB-IR. Nevertheless, they are often used to judge the performance of a wideband antenna. Especially for the directive antenna, a big difference between the maximum directivity and maximum transient effective directivity can be observed. This is because the passband of the directive antenna starts at about 2.2 GHz (see Figure 3.9), but at these low frequencies the antenna features only a very low directivity, resulting in a lower average directivity over the whole frequency band. This weighted averaging effect can be misleading and is one reason to be cautious when using this representation.

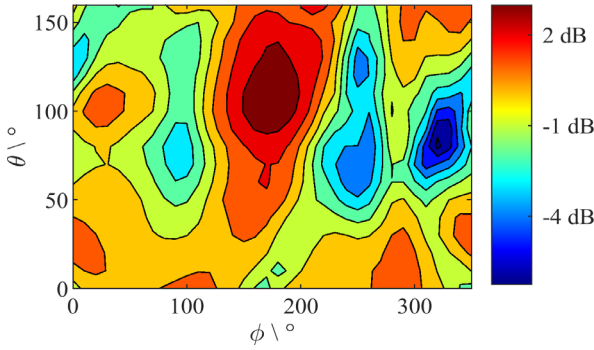


Figure 3.12. Transient effective directivity for absolute polarization values of the omnidirectional antenna.

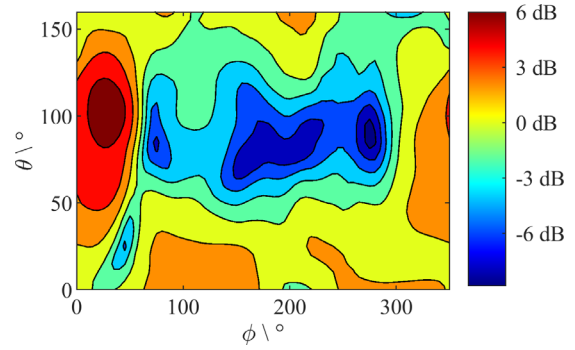


Figure 3.13. Transient effective directivity for absolute polarization values of the directional antenna.

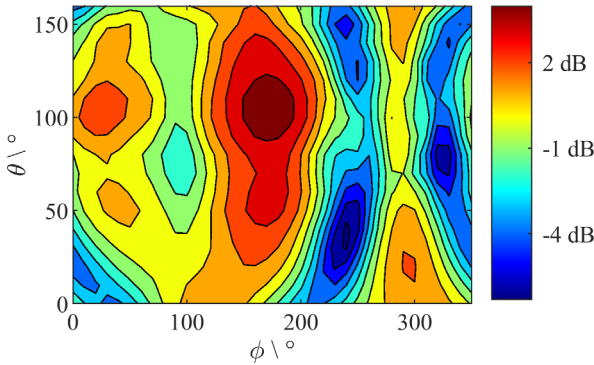


Figure 3.14. Transient effective directivity for horizontal polarization of the omnidirectional antenna.

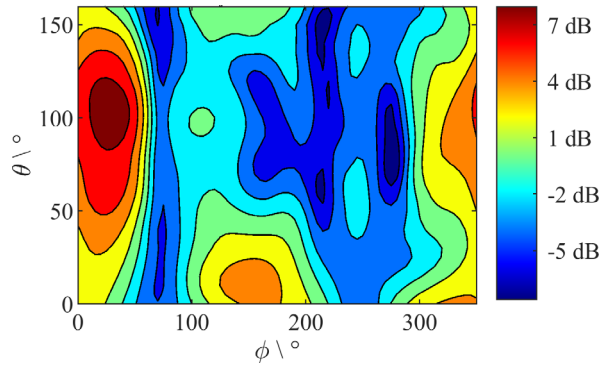


Figure 3.15. Transient effective directivity for horizontal polarization of the directional antenna.

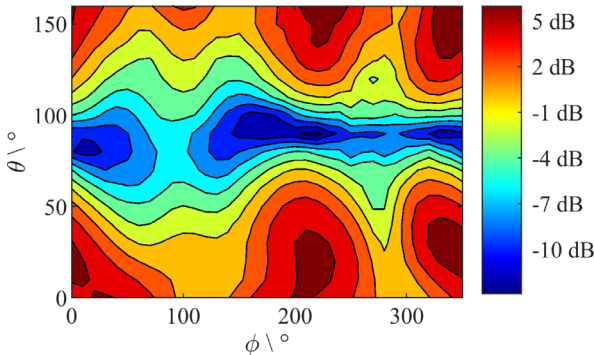


Figure 3.16. Transient effective directivity for vertical polarization of the omnidirectional antenna.

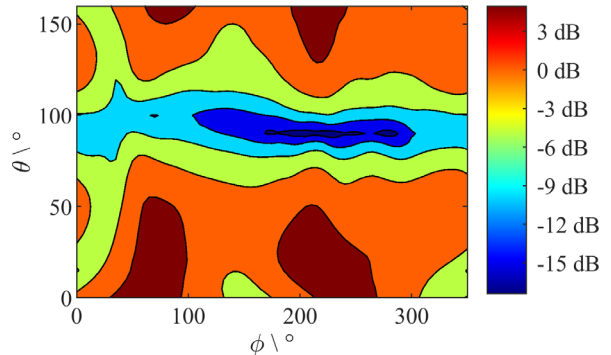


Figure 3.17. Transient effective directivity for vertical polarization of the directional antenna.

In addition to the transient effective directivity many more parameters like the FWHM, RMS delay spread, ringing duration, group delay, peak value and peak-to-average-power ratio (PAR) can be extracted from the transient impulse response of an antenna [36] [48] [49] [50] [51]. Of the above mentioned Figures of Merit (FOM) the PAR, RMS delay spread and group delay variation are plotted for each antenna. Figure 3.18 and Figure 3.19 show the PAR of both antennas, followed by Figure 3.20 and Figure 3.21 visualizing the group delay variation. Figure 3.22 and Figure 3.23 depict the RMS delay spread over the different radiation directions. The equations (3.22) and (3.23) show how the PAR was calculated, A being the power density delay spectrum calculated from the impulse response h_{AUT} of the antenna under test. The length of A is 12 nanoseconds with some buffer time before and after the pulse.

$$A[n, \varphi, \theta] = |h_{AUT}[n, \varphi, \theta]|^2 \quad (3.22)$$

$$PAR[\varphi, \theta] = \frac{\max(A[n, \varphi, \theta])}{\frac{1}{N} \sum_{n=0}^{N-1} A[n, \varphi, \theta]} \quad (3.23)$$

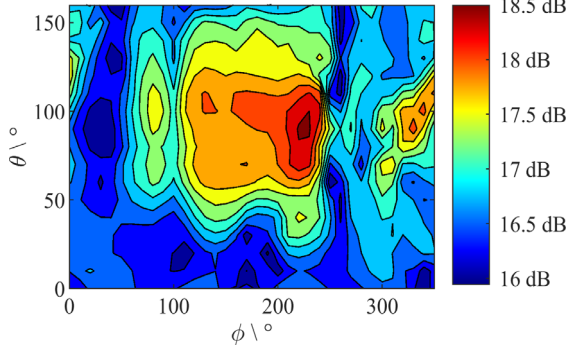


Figure 3.18. peak-to-total-power ratio of the omnidirectional antenna using absolute polarization values.

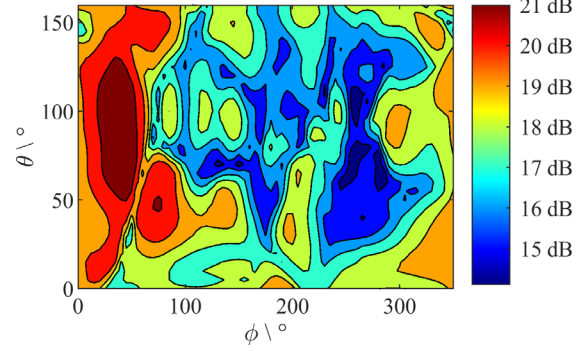


Figure 3.19. peak-to-total-power ratio of the directional antenna using absolute polarization values.

The calculation of the group delay is given by (3.24), followed by the definition of the group delay variation in (3.25). The group delay variation for a specific direction was defined as the difference of the group delay calculated for the direction of interest to the arithmetic mean of the group delays over all directions. In (3.25) K is the number of measurements along φ , and M is the number of measurements along θ .

$$\bar{\tau}[\varphi, \theta] = \frac{\sum_{n=0}^{N-1} t[n] \cdot A[n, \varphi, \theta]}{\sum_{n=0}^{N-1} A[n, \varphi, \theta]} \quad (3.24)$$

$$\tau_{var}[\varphi, \theta] = \bar{\tau}[\varphi, \theta] - \frac{1}{KM} \sum_{k=0}^{K-1} \sum_{m=0}^{M-1} \bar{\tau}[k, m] \quad (3.25)$$

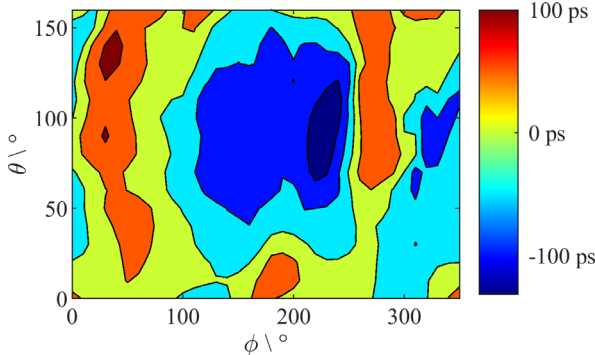


Figure 3.20. Group delay variation of the omnidirectional antenna using absolute polarization values.

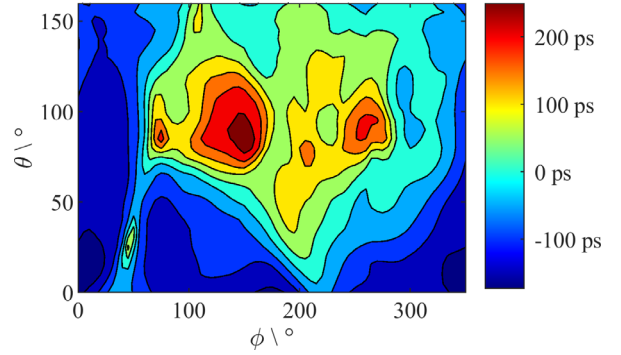


Figure 3.21. Group delay variation of the directional antenna using absolute polarization values.

The delay spread or RMS delay spread is defined as the root of the variance of the normalized power density delay spectrum as presented in (3.26). It is a measure for how widespread in time the impulse response of the AUT is. Larger values correspond to a longer impulse response, though it does not give any information about the exact shape of the impulse response.

$$\tau_{RMS}[\varphi, \theta] = \sqrt{\frac{\sum_{n=0}^{N-1} (t[n] - \bar{\tau}[\varphi, \theta])^2 \cdot A[n, \varphi, \theta]}{\sum_{n=0}^{N-1} A[n, \varphi, \theta]}} \quad (3.26)$$

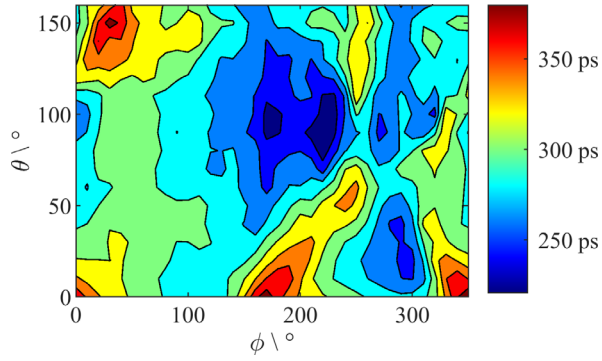


Figure 3.22. RMS delay spread of the omnidirectional antenna using absolute polarization values.

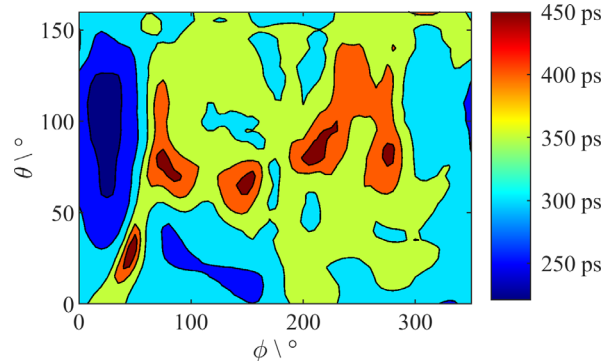


Figure 3.23. RMS delay spread of the directional antenna using absolute polarization values.

On the one hand, the direction of highest directivity of the omnidirectional antenna does not match the direction of the highest PAR, while for the directional antenna this is the case. On the other hand, the highest PAR of the omnidirectional antenna coincides with the direction of the lowest group delay, but here this is not the case for the directional antenna. A similar behavior can be observed if the delay spread is compared to the other parameters. This leads me to the conclusion that although there is some correlation between the above-mentioned parameters, the strength of this correlation is not always the same for different antennas. Therefore, no generally valid connection between PAR, RMS delay spread and directivity can be drawn.

3.2.3 Performance Analysis

The impulse responses calculated by (3.21) are used in the channel model of the UWB PHY Sim to calculate the distance estimation error caused by the non-ideal angle dependent antenna impulse responses. The transmit antenna was modeled using the measured impulse responses, while the receiving antenna was defined as ideal and isotropic. This assumption is necessary, as it is not possible to simulate and visualize results for the permutations of all antenna orientations. For the simulations channel 2 and 4 of the IEEE 802.15.4 standard [55] were used. These channels feature a bandwidth of 500 MHz and 1330 MHz respectively, both at a center frequency of 4 GHz. A leading-edge detection algorithm with a threshold of -20 dB relative to the maximum of the ECIR was used. All remaining parameters were set to ideal conditions, which are: no noise, no interference, no other sources of pulse distortion and an ADC with double precision resolution. A Gaussian pulse shape was selected for the baseband pulse, as the autocorrelation function of an ideal Gaussian pulse does not show any side lobes. The transmit signal s is then calculated as shown in (3.27). T_p being the pulse duration and f_c being the center frequency. For the channels 2 and 4, f_c is approximately 4 GHz and T_p is 2 ns and 0.75 ns. The factor of 2.4 in the exponential function in (3.27) is added to achieve a similar bandwidth as the reference pulse with the same values for T_p as in [55]. The resulting time domain signals are shown in Figure 3.24 and their frequency domain representations as well as the corresponding spectral masks are plotted in Figure 3.25.

$$s(t) = \exp\left(-\frac{1}{2}\left(\frac{2.4 \cdot t}{T_p}\right)^2\right) \cdot \cos(2\pi f_c t) \quad (3.27)$$

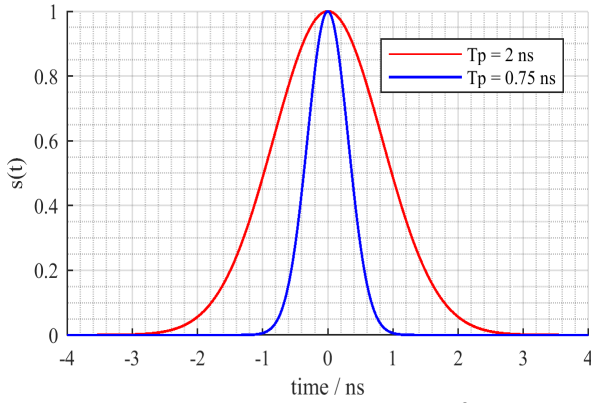


Figure 3.24. Gaussian time-domain waveforms used for simulations [47].

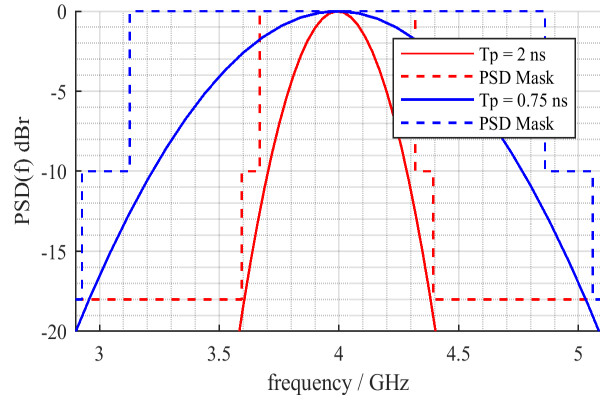


Figure 3.25. Power Spectral Density (PSD) of the waveforms used for simulations [47].

The statistics of the distance estimation error simulations are visualized in Figure 3.26 for the omnidirectional antenna and Figure 3.27 for the directional antenna. The estimation error for the omnidirectional antenna has a 95 % confidence interval of ± 7 cm for both channels. A larger confidence interval of ± 14 cm for channel 2 and ± 17 cm for channel 4 is caused by the directional antenna. How the errors are distributed across the angles is shown in Figure 3.28 and Figure 3.30. For comparison, the fidelity factor across the angles [56] is plotted in Figure 3.29 for the omnidirectional antenna only.

The statistical distributions of the ranging error need to be interpreted with caution. It was expected that the average ranging error over all angles would be much lower for the omnidirectional antenna than for the directional antenna because the directional antenna is intended to be used only in the direction of the main lobe. Pulses radiated in directions with very low directivity are distorted heavily and produce larger ranging errors. This can be observed in Figure 3.30. Depending on the sensitivity of a real system this might not be an issue, due to low antenna gain in this direction which might prevent a correct reception of the signal at all. As I did not introduce any noise in my simulations, all frames could be decoded without data error. Even in directions with low antenna directivity.

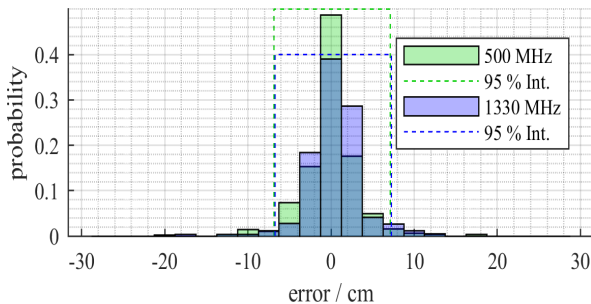


Figure 3.26. Histogram of the distance estimation error caused by the omnidirectional antenna for channel 2 and 4 using 1000 measurements [47].

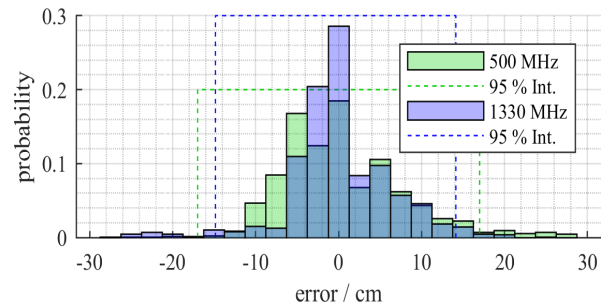


Figure 3.27. Histogram of the distance estimation error caused by the directional antenna for channel 2 and 4 using 4000 measurements [47].

In Section 3.2.2 I concluded that different parameters extracted from the impulse response of an antenna show some correlation, but cannot be interrelated by some general rule. Furthermore, all of the antenna characteristics presented in the previous section are calculated from the antennas impulse response or frequency response, differently the fidelity factor uses information of the employed transmit signal s as calculated in (3.27). This explains why in my analysis the transient effective directivity, PAR, group delay variation and RMS delay spread show only a weak correlation to the distance estimation errors presented in Figure 3.28 and Figure 3.30. The reader should keep in mind that a leading-edge detection algorithm was used for this analysis. Parameters like RMS delay spread or ringing might not be important for this family of algorithms but need to be considered when

algorithms are used that rely on the detection of multipath components. This is because a leading-edge detection algorithm does not use information of the signal after the detected first peak.

The fidelity factor is calculated by the correlation of the input signal to the output signal of the antenna [56]. It is the only of the above-mentioned parameters that uses information of the transmit signal, explaining why there is a strong correlation between the distance estimation error in Figure 3.28 and the fidelity factor in Figure 3.29. At first glance, it looks like all angles with a poor fidelity factor are more prone to higher distance estimation errors. This might sound plausible but is not necessarily true in all cases. In an UWB-IR receiver, an ECIR is calculated by the cross-correlation between the received signal and some pulse template as explained in Section 3.1.5. The ranging algorithm then looks for the first peak of this ECIR. This means that not only the maximum magnitude of the cross-correlation function, which is the definition of the fidelity factor, but also the shape of it is important. The result of this shows at angles where the fidelity factor is low, suggesting a high distance estimation error, but the simulated distance estimation error is also low. This is because the peak of the cross-correlation function might be low, but still at the right position and above the threshold of the used leading-edge detection algorithm. For example, channel 2 at $\varphi = 100^\circ$ and $\theta = 150^\circ$ shows such a behavior. Similarly, a good fidelity factor does not guarantee a good ranging estimate, as the peak of the cross-correlation function might be high, but shifted away from the reference position as in case of channel 2 at $\varphi = 260^\circ$ and $\theta = 140^\circ$. Both examples are highlighted in Figure 3.28 and Figure 3.29 with red circles. Nevertheless, the fidelity factor proved to be a good indicator for the distance estimation error as it provides the best correlation to the simulated distance estimation error of all the analyzed parameters.

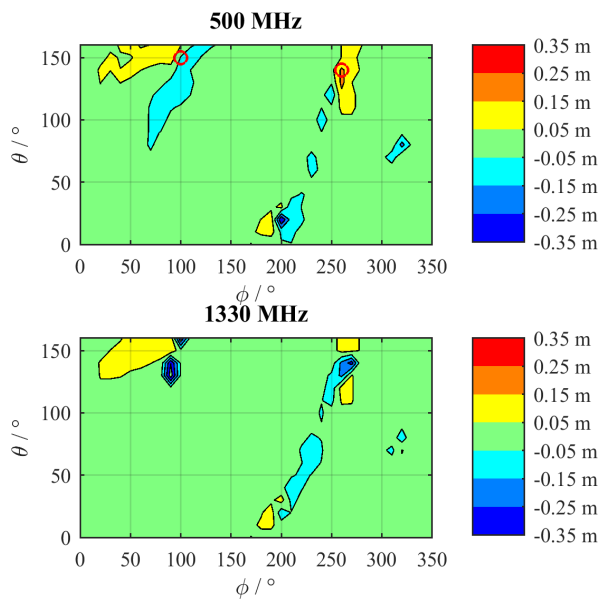


Figure 3.28. Simulated distance estimation error for the omnidirectional antenna. The upper plot is for channel 2 and the lower plot for channel 4. The two red circles in the upper plot indicate examples for angles where the fidelity factor does not match the distance error, as I presented in [47].

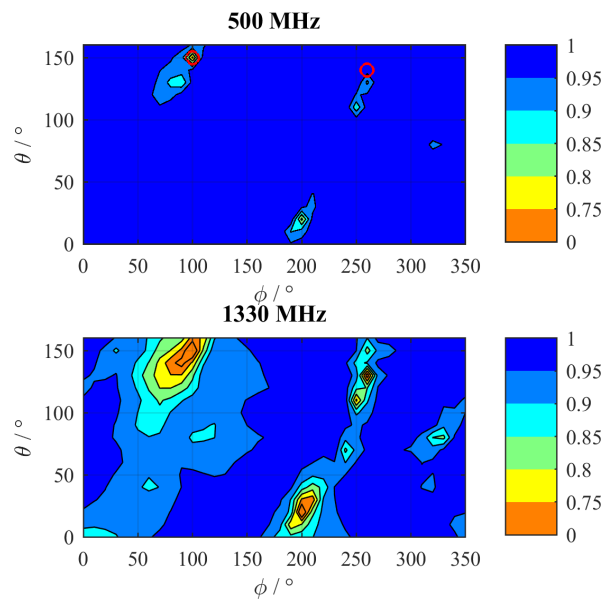


Figure 3.29. Fidelity factor for the omnidirectional antenna. The two red circles in the upper plot indicate examples for angles where the fidelity factor does not match the distance error, as I presented in [47].

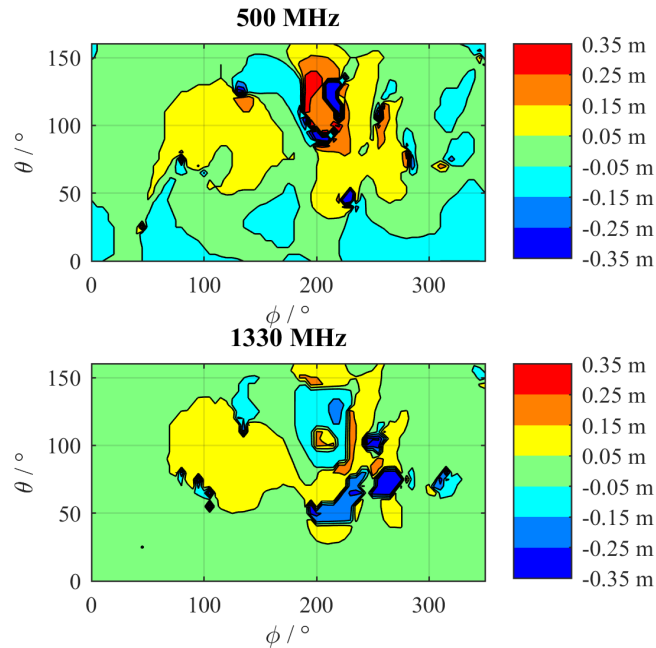


Figure 3.30. Simulated distance estimation error for the directional antenna. The upper plot is for channel 2 and the lower plot for channel 4 [47].

3.3 Impact of Pulse Distortion

In the previous section, I discussed the impact of the angle dependent impulse response of antennas on the ranging accuracy of UWB systems. In a next step, I will highlight the impact of pulse distortion caused by power amplifiers and multiple reflections between a mismatched antenna and the chip as it was discussed in [57]. Pulse distortion is an important topic, due to the correlation-based calculation of the ECIR. Because of this, not only the received signal power, but also the shapes of the received pulses are of vital importance.

3.3.1 Measurement Setup

For the presented measurements, a state of the art UWB chip from NXP Semiconductors™ was used as pulse generator. The chip was configured in a way that it continuously sends the same UWB frame as specified in Section 16. of [58]. The chosen preamble parameters were a code length of 127, delta length of 4 and 64 symbols in the synchronization header. As the following investigations only deal with the synchronization header, the parameters for the data portion of the frame are not mentioned. The used physical channel features a center frequency of 6489.6 MHz and a bandwidth of 499.2 MHz [58]. The output power of the chip was set to a constant value of -0.5 dBm.

To analyze the impact of amplifier non-linearities an external power amplifier (PA) was connected as presented in Figure 3.31. To change the input power of this PA I used a set of attenuators. The selected PA is a HMC311SC70E InGaP HBT from Analog Devices™ featuring a gain of about 14 dB and a 1 dB compression point output power of 15 dBm. The output of the PA was connected to a transmit antenna located at the center of an anechoic chamber. This connection was achieved either directly with a male-male SMA adapter or with SMA cables featuring a length of 75 cm and 180 cm. An identical receive antenna was mounted on a boom. The directional antennas used for this setup are the same antennas which were presented in Section 3.2.1. The two antennas were pointing towards each other using the same polarization plane. To compensate for a portion of the free-space loss a low noise amplifier (LNA) with about 20 dB gain is located right after the receive antenna, before the received

signal is fed to a MS2850A Anritsu™ signal analyzer (SA). The SA's internal LNA further boosts the received signal power, which allows a reception of the signal with a signal-to-noise ratio greater than 30 dB. To capture the UWB signal the analysis bandwidth of the SA was set to 1 GHz. Selecting an analysis time of 250 μ s, an appropriate trigger level and trigger hold off time allowed to measure a whole UWB frame per trigger event.

The captured IQ data was then read by a PC using Matlab® for post processing. In a first step, I truncated the captured IQ data to contain only the synchronization header. Then the data was interpolated to achieve a sampling rate of 26 GHz using sinc interpolation. From this interpolated signal, the peak and RMS power levels were calculated. With the received signal vector y and the ternary code vector x , which was used to generate the preamble, the cross correlation R_{xy} can be calculated by applying (3.28). In this equation N being the length of x and y , and m being the lag of the cross-correlation function. Because the ternary code is not identical to the transmitted signal, even in the ideal case the maximum of the cross-correlation function would not achieve a value of 1. To allow an easier comparison of the results I applied an additional normalization using the maximum value of the cross-correlation function obtained by measuring the signal directly at the chip.

$$R_{xy}[m] = \begin{cases} \sum_{n=0}^{N-m-1} \frac{x[n+m]}{\sqrt{\sum_n |x[n]|^2}} \frac{y^*[n]}{\sqrt{\sum_n |y[n]|^2}} & m \geq 0 \\ R_{yx}^* & m < 0 \end{cases} \quad (3.28)$$

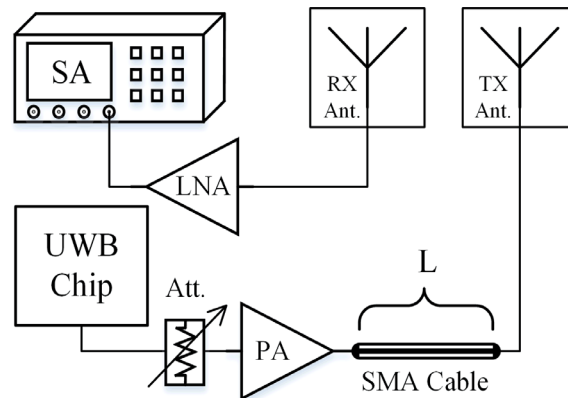


Figure 3.31. Measurement setup for pulse distortion measurements due to amplifiers and mismatched antennas. [57]

3.3.2 Measurement Results

Before I conducted further measurements, I analyzed the stability of the chip's output. For this, I measured 100 frames directly at the chip and calculated the cross correlations of these frames with the mean value of the same frames by using (3.28). This calculation is identical to the calculation of the fidelity factor [50], which was introduced in Section 3.2. The peak values of the calculated cross correlation functions range from 0.983 to 0.999, which is a good result. For comparison, according to [59] a fidelity factor above 0.9 is desired for UWB antennas.

a. Amplifier Non-Linearity

Two pulses of the received frame as well as the corresponding cross-correlation function are shown for different power levels at the input of the PA in Figure 3.32 and Figure 3.33. Table 3.1 contains the peak and RMS power levels at the input of the PA (P_{in}) as well as at the SA (P_{RX}). Furthermore, it also shows the corresponding maximum values of the cross-correlation functions.

Table 3.1. Power and cross correlation values as presented in [57].

Att. [dB]	$P_{in,peak}$ [dBm]	$P_{in,RMS}$ [dBm]	$P_{RX,peak}$ [dBm]	$P_{RX,RMS}$ [dBm]	$\max(R_{xy})$
10	-0.80	-10.49	-18.22	-27.61	0.96
5	4.20	-5.49	-16.46	-24.87	0.86
3	6.20	-3.49	-16.05	-23.95	0.81
0	9.20	-0.49	-15.65	-22.87	0.76

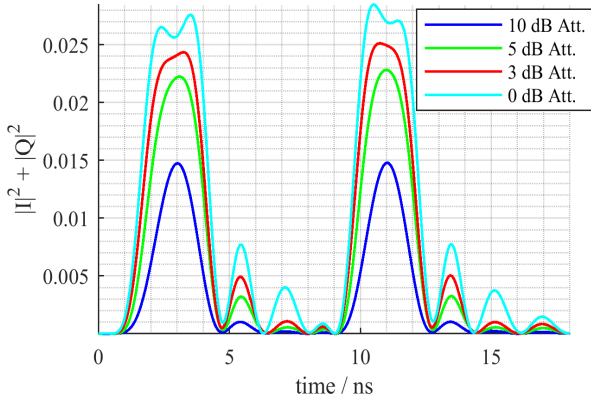


Figure 3.32. Impact of amplifier non-linearities on the transmitted UWB waveform. [57]

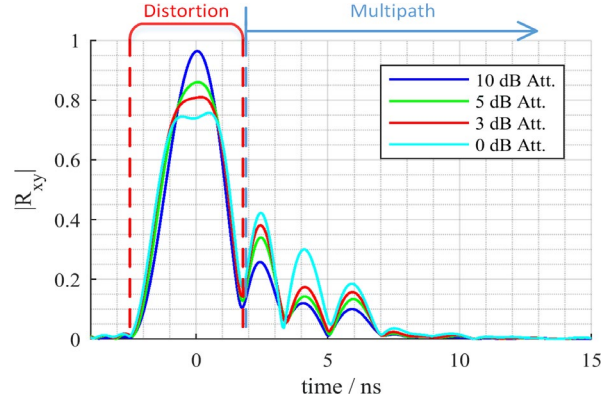


Figure 3.33. Impact of amplifier non-linearities on the cross correlation function for four different input power levels. [57]

b. Antenna Mismatch

Figure 4.29 demonstrates the impact of an antenna positioned at a significant electrical distance from the power amplifier. The two dashed grey lines indicate where reflections due to finite antenna and amplifier output matching were expected for a 75 cm and 180 cm SMA cable respectively. The blue trace shows the result if a male-male SMA adapter was used. The output matching of the PA was determined using a VNA and it is in the range of -14.4 dB to -12.3 dB. The dynamic range of the cross-correlation function is around 60 dB. The corresponding lower sensitivity limit for the cross correlation is introduced by the noise floor of the measured IQ signal. The signal's noise floor is further reduced by about 30 dB due to the correlation over 4096 pulses with the ternary code.

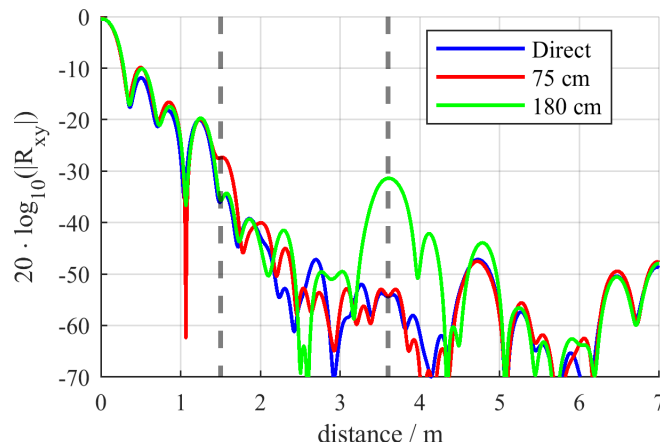


Figure 3.34. Impact of mismatched antenna at different distances from the PA. Distances on the x-axis are calculated assuming a propagation velocity of 0.7 times the speed of light. [57]

3.3.3 Discussion of Measurement Results

Above I mentioned that not the transmitted waveform is used as a template for the cross-correlation (R_{xy}), but rather the ternary code used to generate the preamble. This is a method often used in practice to reduce the computational effort. By following this approach, the analysis is closer to what is achieved in a real system. Another benefit is that for pulse shapes without leading side lobes this template does not produce any side lobes before the main lobe in the cross correlation function R_{xy} , as it can be observed in Figure 3.33. This is of major importance for any application which relies on leading edge detection algorithms for ranging. In this case, the leading side lobe level limits the maximum possible strongest to first path detection ratio. For the remainder of this section I always refer to a system using a ternary code as template and a leading-edge detection algorithm for ranging. Most leading-edge detection algorithms known to the author use a threshold to identify a leading edge in R_{xy} , as described in Section 3.1.6. Then the next peak in R_{xy} is identified to be the first path, this is also the method proposed in [58].

Before I continue with this discussion, I need to define what I understand by the terms “distortion” and “multipath”. For simplicity I categorize everything as distortion that has an influence on the main lobe of the cross-correlation function. In Figure 3.33, this area is marked with the dashed red lines. Be aware that by this definition a second signal path with an electrical distance close to the shortest path also introduces a distortion effect. The other way round, everything affecting the part after the cross correlations main lobe is further referred to as a multipath effect. Following this definition, the only thing affecting the ranging accuracy of an ideal receiver using a leading-edge detection algorithm is distortion and SNR, under the assumption that a proper threshold was chosen.

a. Impact of Amplifier Non-Linearity

Figure 3.32, Figure 3.33 and Table 3.1 show what happens to the signal and R_{xy} if the PA is driven into saturation. With a 10 dB attenuator, the instantaneous peak input power of the PA is at -0.8 dBm, resulting in a gain of 14 dB. Under these conditions the PA is still well below its 1 dB compression point. In this case, the maximum value of R_{xy} is 0.96, which is only 0.02 below the chip’s performance but also incorporates the distortion due to the antennas. Increasing the input power (P_{in}) step-by-step drives the amplifier into saturation, as you can observe due to the diminishing increase of received power (P_{RX}) at the SA (see Table 3.1). As expected, the received peak power is increasing less than the RMS power. This also demonstrates why looking at the RMS power might be misleading. While in saturation, a higher percentage of energy is distributed to the side lobes of the pulse, and the magnitude of the multipaths in R_{xy} is increased. By my definition, multipaths do not affect the ranging accuracy, but additional signal power in the side lobes of the pulse increases the SNR. It becomes obvious that although a higher RMS output power increases the SNR of the signal, the peak power of the signal is the characteristic factor for the dynamic range of R_{xy} . Phrased differently, additional power in the side lobes of the pulse does not improve the dynamic range of R_{xy} , despite increasing the RMS output power. Only increasing the power of the pulse’s main lobe yields an increase in dynamic range of R_{xy} .

In addition to the increase in multipath level, driving the PA into saturation also introduces distortion due to gain compression. Figure 3.33 demonstrates this effect. The main lobe of R_{xy} becomes wider and flatter the more the PA is pushed into compression. A flatter main lobe reduces the accuracy of the peak detection, and therefore of the estimated ranging result. In the case of 0 dB attenuation the main lobe gets two peaks which are about 1.5 ns apart from each other. By looking at the signal in Figure 3.32 one can also observe that there is a difference in shape between the first and second pulse. As I used a delta length of only 4 chips between pulses, they begin to interfere with each other. Increasing the delta length would be a possible solution for this issue, but also increases the duration of a frame. The drawback of long frames is that transmit and receive chips need to be in a high-power

state for longer periods. In such a state, many digital parts of the chips will also be powered up, resulting in a significant increase in power consumption. [60]

b. Impact of Antenna Mismatch

In final products antennas are usually placed close to the chip. For demonstration purposes or laboratory setups the antenna might be connected to a chip using a SMA cable as well. Because of the imperfect matching of the antenna and the chip's output, reflections between them distort the pulse or appear as multipath components. As already mentioned, the return loss of the used antenna is about -15 dB to -13 dB, and the return loss at the chip's output is in a range of -14.4 dB to -12.3 dB. Adding twice the insertion loss of the additional cables leads to reflections around -30 dB relative to the magnitude of the output pulse. On the one hand, this does not pose a problem for a leading-edge detection algorithm, as the reflection is too weak to significantly distort the pulse if the connection is short. In the case of a long cable the additional multipath does not influence the result. On the other hand, this might lead to misinterpretations if the cross-correlation function is used to estimate the complete channel impulse response. The artificial multipath could be wrongly interpreted as a property of the wireless transmission channel. Furthermore, it should be mentioned that the matching of the selected antenna and the chip output is rather good. Less beneficial conditions might result in more severe distortion and stronger multipath magnitude. As shown above, simply adding the return losses of antenna and chip provides a rough estimation of this phenomenon. For laboratory setups, this effect can be mitigated by adding an additional attenuator between chip and antenna. The loss in SNR can be compensated by increasing the number of preamble symbols and accordingly the power consumption.

3.4 Simulation of a Two-Ray Channel

An important test case for evaluating the ranging error is the two-ray channel with dominant second path. Two ray channels are popular to analyze the performance of ranging systems in a controlled and repeatable environment with wired connections. The closer the spacing and the higher the magnitude of the second path, the more difficult it gets for a ranging system to detect the first path. For this analysis, different signal-to-noise ratios (SNR) and thresholds for the leading-edge detector were simulated instead of changing the multipath parameters. All simulations were performed using a Gaussian pulse shape resulting in a 10 dB bandwidth of 500 MHz and an ideal ADC with 1 GHz sample rate and double precision resolution. Figure 3.35 shows the mean relative distance estimation error over SNR for 5 different threshold multipliers. Each trace is the mean value of 64 realizations. As a reference, also the package error rate is plotted. The length of the payload data was chosen to be 128 bits, and the preamble consisted of 64 symbol repetitions of a 31-bit preamble code. A two-ray channel with a line-of-sight (LOS) distance of 10 m and 20 dB stronger second path at 15 m was used as a propagation channel.

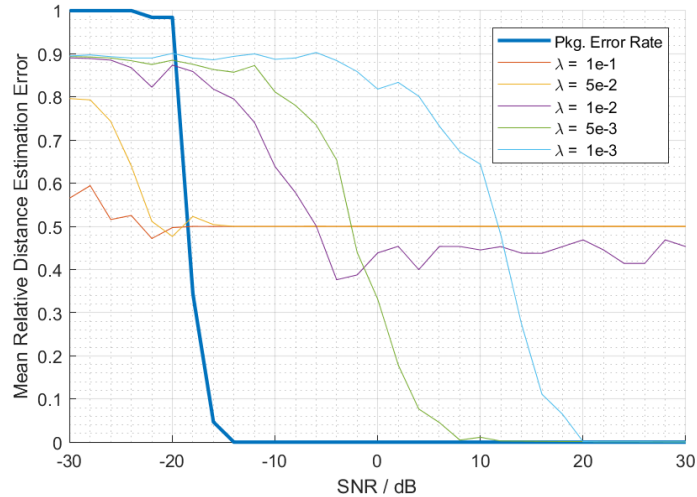


Figure 3.35. Comparison of threshold multipliers λ for a two-ray channel with a LOS distance of 10 m and a 20 dB stronger multipath component at 15 m. Ranging errors of 0.5 are due to the algorithm detecting only the stronger second path instead of the first LOS path. [39]

The results presented in Figure 3.35 display the trade-off when deciding for a threshold multiplier. On the one hand, the threshold should be far away from the noise floor to minimize the number of false detections due to noise. On the other hand the threshold should be very low to enable the detection of weak first paths. For a threshold multiplier of λ equal 1e-1 to 1e-2 the average distance estimation error does not fall below 0.5. This is because the leading-edge detection algorithm only detects the 20 dB stronger multipath component, but not the LOS component. The upside is that this strong component can be detected down to about -25 dB SNR. In case of low thresholds, the ranging error approaches zero for high SNR values but the ranging starts to fail before the package error rate is affected, which shows the necessity of analyzing the ranging error and package error rate jointly. Regarding the simulation itself a smaller SNR step size of 1 dB or 0.5 dB and higher simulation count per SNR value would improve the quality of the plots but were not carried out because it already took a couple of days to simulate the presented results. These simulation results look similar to the measurement results presented in [61], and represent quite well the expected behavior. When looking at the presented results the reader should remember that the dynamic of the ECIR does depend on the SNR of the received signal as well as the length of the SHR, as it was mentioned in Section 3.1.5.

3.5 Multiuser Interference Simulations

In situations with many UWB devices operating in close vicinity to each other, multiuser interference becomes a major issue. In an automotive context, a scenario for this case is the parking lot after a soccer game. For indoor localization a subway station can be mentioned as an example for a multi-user interference case. To mitigate the effect of multiuser interference the frame format can be optimized for multiuser interference rejection. In this section, I investigate the impact of different frame parameters on package error rate in a multiuser interference scenario. These results can be applied in high level protocol simulations to find the sweet spot between long and robust frames with high collision probability, or short frames susceptible to errors due to multiuser interference. All simulations were performed using a Gaussian pulse shape resulting in a 10 dB bandwidth of 500 MHz and an ideal ADC with 1 GHz sample rate and double precision resolution.

Figure 3.36 and Figure 3.37 present a comparison of the package error rate over signal to interference ratio (SIR) for two different demodulator models and 3 symbol formats. Demodulator 1 (solid line) only looks at the correlation at the expected burst positions while demodulator 2 (dashed line) uses the

whole symbol. The symbol formats vary in terms of burst positions per symbol (BPPS) and chips per burst (CPB). For the presented simulations, an infinite SNR and perfect LOS channel were used. The package error rate was calculated from 128 realizations and 128 bits payload data per frame. Figure 3.36 shows results for cases where the data part of the interference signal is overlapping with the data part of the transmitted signal, while Figure 3.37 shows results for preambles of the interference signal overlapping with the data part of the transmitted signal.

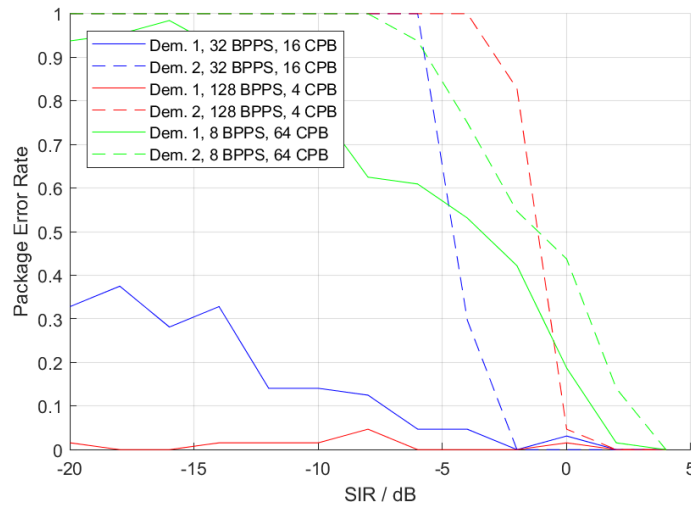


Figure 3.36. Impact of interference on package error rate for different demodulators and symbol formats. For this plot the data part of the interference signal is overlapping with the data part of the transmitted signal. [39]

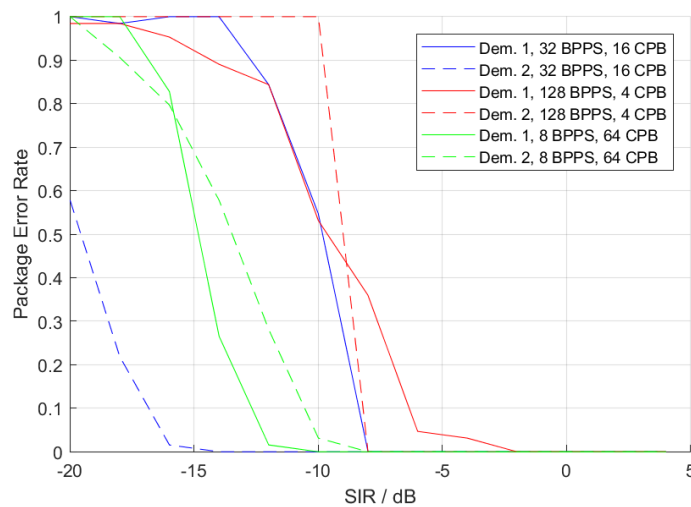


Figure 3.37. Impact of interference on package error rate for different demodulators and symbol formats. For this plot, the preamble of the interference signal is overlapping with the data part of the transmitted signal. [39]

Figure 3.38 presents a comparison of interferences on different logical channels, which means that the preamble code of the interference signal is changing. In this case, the interference signal uses an equally distributed time shift relative to the transmitted signal. Under these conditions, the interference signal's preamble is overlapping with the beginning of the transmitted signal's data part in about 50% of the simulations.

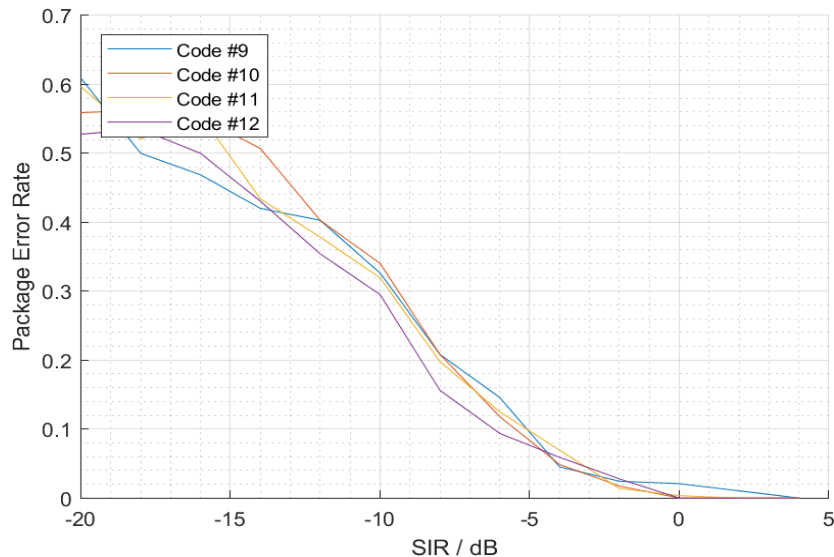


Figure 3.38. Comparison of different preamble codes for the interference signal while the transmitted signal is using code #10. The used symbol format is 32 burst positions per symbol (BPPS) and 16 chips per burst (CPB). There is a probability of 50% that the beginning of the data part is overlapped by the preamble of the interference signal. [39]

The results of the interference simulations shown in Figure 3.36 and Figure 3.37 visualize that burst position modulation is able to suppress the impact of overlapping frame data parts, but not the impact of an interference preamble overlapping the transmitted data part. This drawback is mitigated by the fact that the impact of preamble overlapping only becomes visibly for lower SIRs compared to data part overlapping, with the exact value depending on the used symbol format. A higher number of chips per burst increases the energy of a burst, which is beneficial for interference rejection against preamble pulses. Although in Figure 3.37 demodulator 2 seems to perform better with only 16 chips per burst. This behavior depends on the spacing between preamble pulses, which was chosen to be 16 chips for the presented simulations. More chips per burst result in multiple preamble pulses to overlap with the same burst, alleviating the advantage of longer and higher energy bursts. For a decoder masking out unexpected burst positions an increased number of burst positions per symbol positively influences the impact of data part overlapping as can be observed in Figure 3.36. The downside of increasing the number of burst positions per symbol as well as chips per burst is a lower bitrate and longer frames. Longer frames increase the overall probability of a frame collision on a shared channel. The simulation results for different logical channels illustrated in Figure 3.38 confirm the expected. All channels perform equally well, with a slight deviation which can be explained by the low count of simulations per SIR value of only 64. Even if the interference signal is on the same logical channel, but time shifted, the performance is equal to other logical channels due to the good autocorrelation properties of the chosen codes.

3.6 Conclusion for System Level Analysis

Let us summarize the learnings of this section. The presented ultra-wideband physical layer simulation environment (UWB PHY Sim) developed in Matlab® makes use of most parameters defined in the IEEE 802.15.4 standard [22] and more. Ready to use channel models are provided with the simulation environment to allow a quick start. The import of channel measurements is supported and due to the modular structure and defined interfaces. The implementation of new models is straightforward. This is not only the case for channel models but holds for all building blocks of the UWB PHY Sim.

The presented simulation environment was used to investigate the correlation of commonly used antenna characteristics to the distance estimation error of an UWB system. More precisely the impact of the angle dependent impulse response of two planar UWB antennas on the ranging accuracy was investigated and presented in Section 3.2. For this purpose, measurements in combination with the UWB PHY Sim were used. This new approach led to the conclusion that antenna parameters derived from the antenna's impulse response only provide limited information on the behavior of an antenna in a real system. This is because most parameters, except for the fidelity factor, do not use any information of the used signal. In my opinion, this is not only a problem of antenna designers providing the wrong information, but rather a lack of integration in the system design process. Antenna designers often do not know in which systems their antennas will be used. Therefore, they need to rely on such generic parameters to describe the performance of their antennas. The results for the distance estimation error showed, that for many applications the error caused by the antenna might be negligible if an appropriate UWB antenna is used. If the impact must be considered, a detailed analysis of the antenna considering the used transmit signal and ranging algorithm needs to be carried out, for example by using the UWB PHY Sim. Pre-distortion in the chip and matching networks can help to achieve better system performance. System architects need to be aware that antennas cause angle dependent pulse distortion, and depending on the antenna design this impact might be significant.

In Section 3.3 I explained that the peak power of an UWB signal is an important factor for the maximum dynamic range of the cross-correlation function. Due to this fact, instead of the commonly used SNR, a peak signal power to noise power ratio should be used as performance metric. I also showed that driving an amplifier into compression causes the main lobe of the cross-correlation function to become flatter. This increases the ranging error, because of a reduced accuracy of the peak detector often used in combination with leading edge detection algorithms. An additional source of pulse distortion due to antennas, besides their non-ideal transmit impulse responses mentioned in the previous paragraph, is the double reflection between them and the output of the chip. A rough estimation of the impact of this phenomenon can be achieved by adding the return loss of the antenna and the chip output. For small electrical lengths between chip and antenna, this value is a measure of the introduced pulse distortion. If the corresponding length is greater than the duration of the pulse's main lobe it is a measure for the magnitude of artificially generated multipath component.

The simulations for different SNRs in Section 3.4 show the dilemma designers are facing when they need to decide for thresholds for leading edge detection algorithms. A low threshold provides good first path detection but increases the probability of false detections due to noise. A high threshold might miss the first path and incorrectly identify a stronger second path's leading-edge. To mitigate this issue the dynamic of the ECIR can be improved by increasing the number of symbols and consequently total power in the SHR. This approach increases the frame duration and power consumption in the transmitter and receiver. In addition, the probability of frame collisions increases with the length of frames, after all the wireless channel utilized by UWB-IR is a shared medium.

The impact of multiuser interference on package error rates was investigated in Section 3.5. Increasing the burst positions per symbol and chips per burst increases interference robustness in case of a frame collision. Yet, it also increases the frame length and due to that also the probability of frame collisions. As the UWB PHY Sim only deals with the physical layer, network simulations cannot be done directly, but the results are stored in a database and can easily be accessed from a third-party software. The next task at hand would be to derive metrics for striking the compromise between probability of collision and robustness in case of a collision. Such investigations are not part of this thesis and are left for protocol designers dealing with this matter.

4 Device Characterization and Optimization

The external circuitry of a chip significantly influences its performance. With respect to the radio frequency (RF) signal path it is mandatory to optimize the external circuitry in a way to achieve good performance in terms of power consumption, power matching and for UWB-IR systems also pulse shape. To achieve these goals, accurate information on the behavior of the chip – our device under test (DUT) – is needed. Behavioral models representing the linear and nonlinear response of the chip can provide this information. The loading applied by the external components can significantly influence both, the linear and nonlinear device behavior. Due to the sensitivity of the device onto the external loading as well as the complex nonlinear interactions between the external components and the device itself, highly accurate models representing the linear and nonlinear behavior over the full bandwidth, the baseband and harmonic frequency ranges are required. Designing and parameterizing such models is a highly demanding task. To avoid this complex modeling task and still get the desired relationship between the device and its external components requires implementing them in hardware. By connecting tunable external components, typically realized by slab-line based stub tuners, the device can be tested under different loading and operation conditions. These tuners introduce the desired reflection coefficients at the ports of the device. Such a hardware-based approach to optimize the device behavior is summarized by the term load-pulling or source-pulling of a device dependent on the placement of the tuners at the output or the input. Figure 4.1 shows a comparison between different types of load-pull setups. The first setup (a) is passive load pull system as it only uses passive components to generate the wanted reflection coefficient. The setups (b) and (c) are active load-pull systems because they use active components. The advantage of active load-pull systems over passive systems is that the maximum reflection coefficient that can be provided to the DUT can have a magnitude of one or even higher. Achieving a magnitude of one with passive load-pull systems is not possible because of the insertion loss of the used components. On the one hand, this gives active load-pull systems a significant advantage over passive systems when it comes to tuning range. On the other hand, building such an active system is more complex as the linearity of the used devices needs to be considered and becomes problematic if the DUT is a high-power device, in addition the stability of the control loops needs to be taken into account. The diagrams in Figure 4.1 only show single ended load-pull setups. If such a setup should be built for a differential device the additional complexity of having two balanced control loops makes this approach an even more demanding task. How to build a passive load-pull setup for differential devices with rather low effort is summarized in Section 4.2.

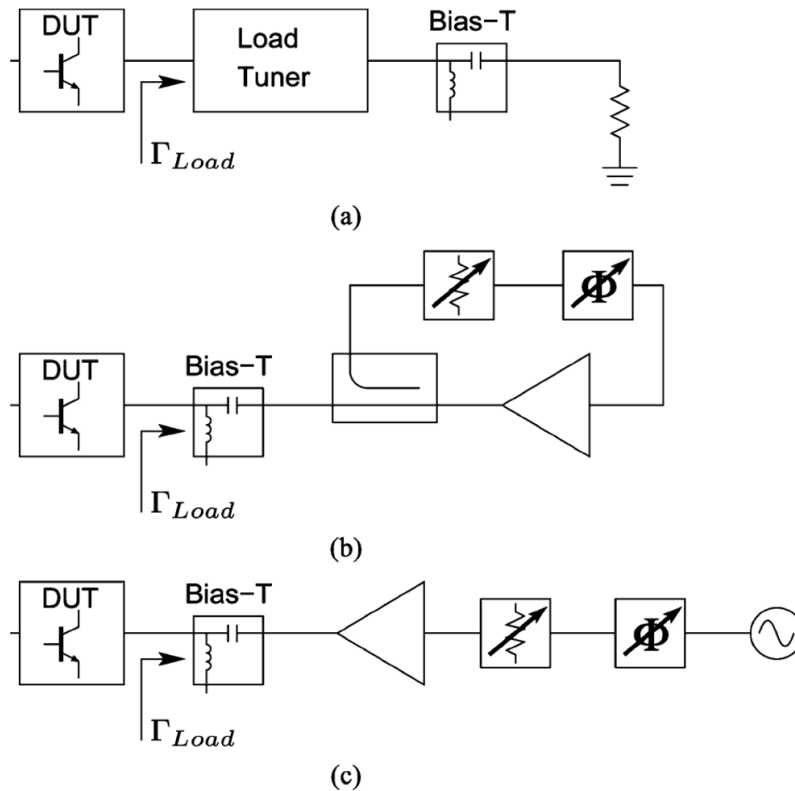


Figure 4.1. A typical configuration for passive load pull (a), compared with a typical closed-loop configuration (b) and a typical open-loop configuration (c) for active load pull. [62]

The most used modern impedance tuner is the slide-screw tuner. For all measurements involving impedance tuners in my test setups, I used two such tuners manufactured by Maury Microwave®. They consist of a 50 Ω slab-line made of two parallel plates and a center conductor. A probe can be placed in different distances above the line (y position) and moved to different locations along the line (x position) as shown in Figure 4.2. When the probe is completely withdrawn from the slab-line, the signal entering the tuner passes through with minimal interference. As the probe is lowered into the slab-line, a part of the signal is reflected towards the DUT. The magnitude of the reflection coefficient introduced by the tuner is increased in this way. As the probe's position along the line changes, the distance between the tuning element (probe) and DUT changes, causing a phase shift of the reflection coefficient. This behavior is presented in Figure 4.2 and Figure 4.3. By moving the probe up and down, left and right, I am able to present nearly any impedance to the DUT, only limited by the insertion loss of the used connections and the tuner itself.

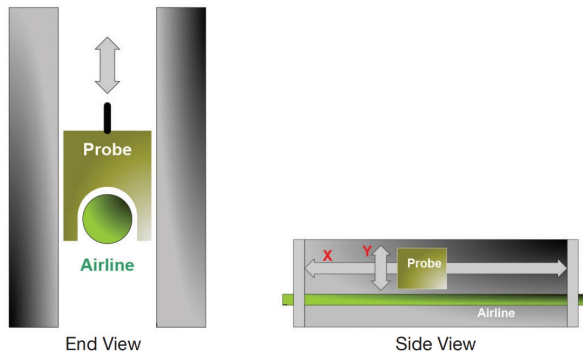


Figure 4.2. shows the mechanical structure of a Slide-Screw Tuner.

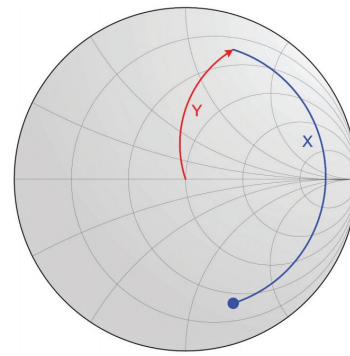


Figure 4.3. shows the impact of changing the X and Y positions (see Figure 4.2) of a Slide-Screw Tuner on the reflection coefficient at the input of the tuner.

4.1 De-Embedding for Mixed-Mode Load-Pull Setups

Before discussing different methods for mixed-mode load-pull measurements, I want to discuss the de-embedding procedure needed for such a system. De-embedding mathematically removes a fixtures effect on the measurements, leaving only the behavior the DUT. This is used for non-coaxial connections from a VNA to the DUT, which make it impossible to perform a calibration at the reference plane of the DUT. In case of two-port networks, de-embedding can easily be achieved by using T-parameters as shown in Figure 4.4. For this approach, the S-parameters S_{fix} of the fixture need to be known. This can be achieved by performing initial measurements with known calibration standards instead of the DUT. For further information on this topic, the author can recommend [63] and [64].

For multiport networks, the simple approach presented in Figure 4.4 cannot be applied directly. Therefore, this Section deals with de-embedding of multiport networks using a Mason's rule Matlab[®] implementation.

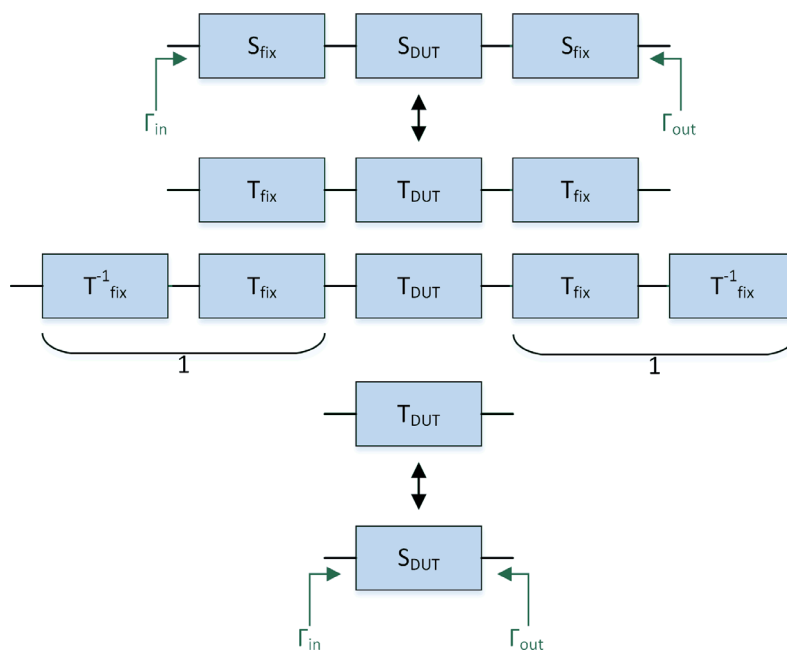


Figure 4.4. De-embedding of measurement fixture using T-parameters.

4.1.1 Demo Setup

The load-pull measurement system used for the investigations in this Section uses microstrip directional couplers to perform measurements with minimal influence on the load impedance provided to the device under test (DUT) [65] [62] [66]. The setup is shown in Figure 4.5 and was first proposed in [67]. It uses the DW1000 chip, featuring two different variable amplifier stages, allowing adjustment of the gain over a range of 24.5 dB in 0.5 dB steps. On the printed circuit board (blue rectangle in Figure 4.5) each line of the differential output passes two directional couplers, before they are connected to the interface (SMA connectors), used to attach different loads. As load, a stub tuner was connected to each SMA connector. The directional couplers are used for measuring either the forward or backward traveling waves along the line. Some measurement device like an oscilloscope can be connected to these measurement ports, while a load is connected to the chip via the direct path. For [67] the LeCroy WaveMaster® 816 Zi oscilloscope was used. On the one hand, a low coupling factor for the directional couplers was selected to minimize coupling between the oscilloscope and the load presented to the device. On the other hand, the sensitivity of the employed oscilloscope needs to be considered. A coupling factor of about -20 dB is the lowest factor that allows measuring the output signals of the chip, if an oscilloscope featuring a sensitivity of 2 mV is used. To calculate the signal at the pads of the chip from the measurement results provided by the oscilloscope, de-embedding needs to be applied to the recorded data. This de-embedding must remove the influence of lines, directional couplers, connectors and cables between the chip and the oscilloscope. In addition to the de-embedding of the passive connection network, also constant synchronization errors between the channels of the oscilloscope are removed in this post processing step.

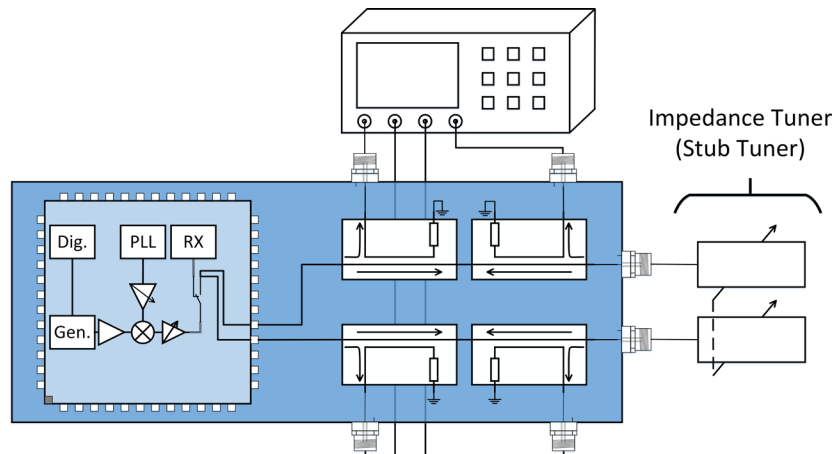


Figure 4.5. Block diagram of a DW1000® UWB ranging chip on a PCB with directional couplers. Connected to the PCB are an oscilloscope and impedance tuners. All components together form a differential load-pull measurement setup. [67]

a. Directional Couplers

As mentioned in the last section the directional couplers are crucial components of the measurement system. They need to have a relatively constant coupling factor of approximately -20 dB over the full frequency range of interest. Due to the intended UWB application, I am interested in the frequency range from 3.7 GHz to 7 GHz. This includes 6 of 7 channels supported by the DW1000 [68] [69]. Furthermore, a good directivity is desired, to accomplish a high decoupling between the forward and backward traveling waves. After simulation and comparison of different directional coupler types presented in [70], [71], [72], [73], [74] and [75], I selected a microstrip wiggly line coupler [70], [71]. These couplers provide a relatively constant coupling factor and acceptable directivity over a wide bandwidth. Furthermore, they do not need any lumped elements. The layout of the designed coupler is presented in Figure 4.6. One line of the coupler is kept straight to allow accurate length matching of

the differential microstrip lines. The optimization of this coupler was done using the National Instruments® Applied Wave Research (AWR) software package. Simulation results are shown in Figure 4.7. The figure highlights the desired coupling factor of approximately -20 dB as well as a directivity between 15 dB and 20 dB in the frequency range of interest.

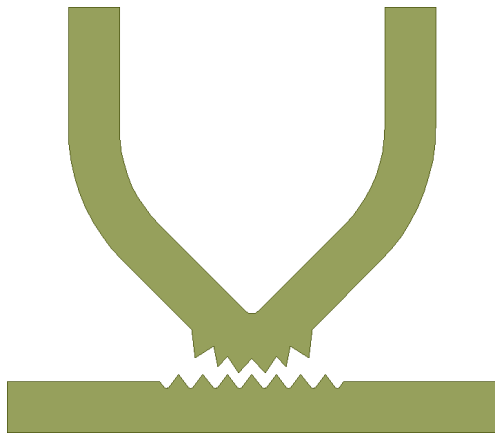


Figure 4.6. Wiggly line directional coupler in microstrip technology on a RO4350B substrate. [67]

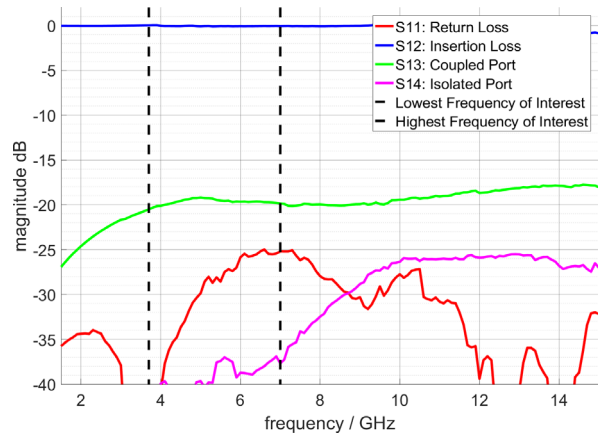


Figure 4.7. Simulated S-parameters of the wiggly line directional coupler. In the frequency range of interest an isolation of better 10 dB is achieved. [67]

4.1.2 De-Embedding with Signal Flow Graphs

During the de-embedding of the measurement system, a model of the fixture is used. This procedure provides the signals at the reference plane of the DUT without complex non-coaxial calibration standards [76]. However, the model of the test fixture must accurately represent the behavior of the corresponding hardware under all impedance and operating conditions.

Figure 4.8 visualizes the composition of the measurement and the DW1000 PCB. As the lines of the differential output stage are symmetric, only one side of the PCB is covered by the following simulations and measurements. The red line at the zoom in view of the chip highlights the location of the corresponding reference plane. Clearly, the position of this interface prevents measuring the network parameters of the test fixture directly. Due to the complex transition from the interface position to the microstrip line on the measurement board, I did not want to rely on simulation results only.

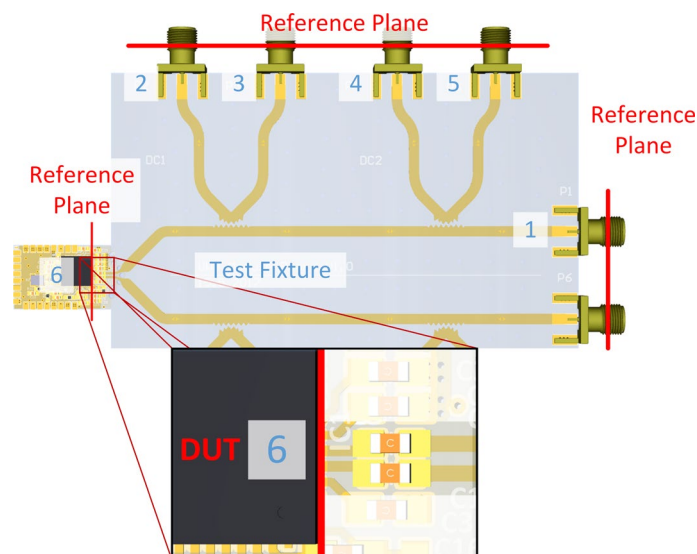


Figure 4.8. PCB layout implementing the block diagram of Figure 4.5 and the directional coupler shown in Figure 4.6. [67]

To characterize the measurement setup, two additional PCBs using the same stackup composed of Rogers RO4350B™ laminate, were designed and manufactured. The PCB presented in Figure 4.9 is an exact copy of the test fixture, but instead of the chip it features a SMA connector. Only one of the differential lines was placed on this PCB, as the differential lines are symmetric and their coupling is weak. The six port S-parameters of this PCB were measured directly using a vector network analyzer. The second PCB shown in Figure 4.10 contains calibration standards to determine the two port S-parameters of the additional SMA connector, pads and RF lines, which replaced the chip, by means of a through, reflect, line (TRL) calibration [77] [78]. To derive the S-parameters of the test fixture (see Figure 4.8), the two port S-parameters from the error boxes of the TRL calibration were de-embedded from the measured six port S-parameters (see Figure 4.9) within AWR.

For the de-embedding, also the reflection coefficients of the chip and oscilloscope as well as the S-parameters of the used SMA cables are needed. To measure the reflection coefficient of the chip (Γ_{Chip}), S_{11} was measured at port 1 (see Figure 4.8) using a VNA. Then the influence of the test fixture was de-embedded, resulting in the reflection coefficient at the pads of the chip. The reflection coefficient for each channel of the oscilloscope as well as the S-parameters of the cables were measured directly using the VNA with proper calibration. For the measurement of the different oscilloscope channels, I took care that the input voltage range setting of the oscilloscope was kept constant to avoid changing impedances. Therefore, I measured the reflection coefficients of the oscilloscope for each applicable input voltage range.

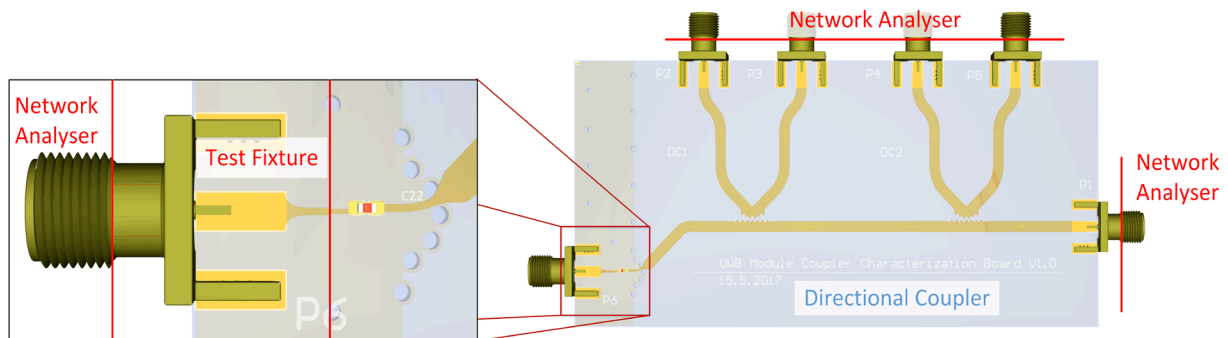


Figure 4.9. PCB with directional couplers and SMA connector instead of the chip. The S-parameters of this PCB can be measured using a VNA.

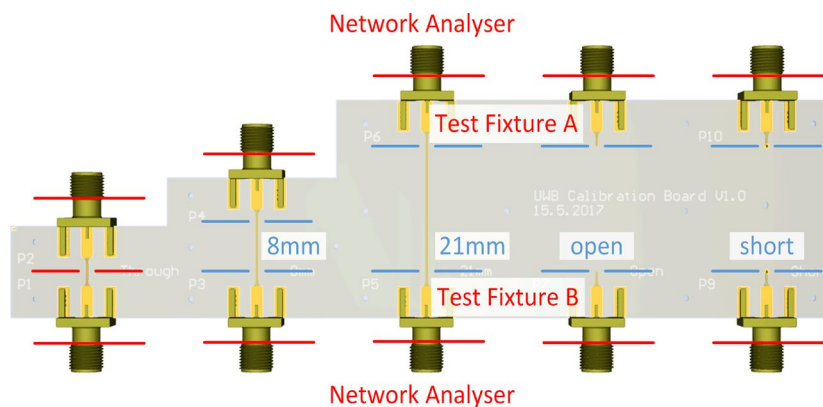


Figure 4.10. TRL calibration kit used to calculate the S-parameters of the test fixture which replaced the chip in Figure 4.9. The influence of this test fixture can then be removed from the measured signals.

For the de-embedding of the whole measurement system, including the PCB test fixture, SMA cables, oscilloscope matching and chip matching, a signal flow graph (SFG) was derived and is shown in Figure 4.11. The resulting SFG, composed of 22 nodes, was solved using a Matlab® script [79] utilizing Mason's gain formula. This script provides the analytically derived path gains needed for the de-embedding procedure. These transfer functions G_{ij} are used in de-embedding to calculate the signal at the pads

of the chip from the signal measured at the ports of an oscilloscope. Due to the complexity of these expressions, they are not stated here.

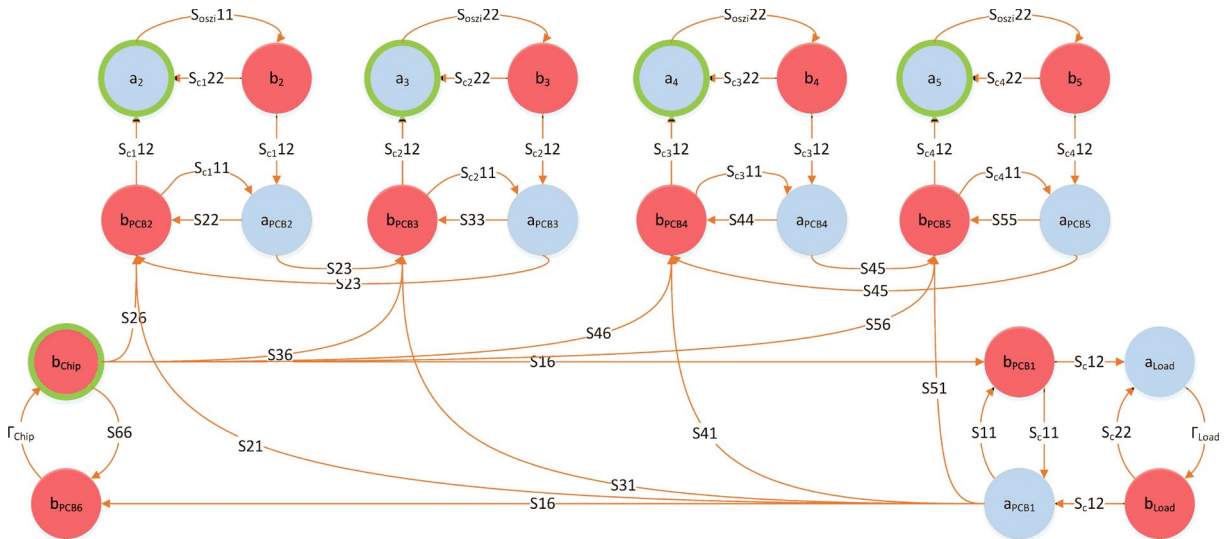


Figure 4.11. Signal flow graph used for de-embedding. The circles with green contour show the node b_{Chip} representing the output signal of the chip and the nodes a_2 to a_5 which represent the input signals of the oscilloscope. The path gain between this nodes is used to calculate the signal at the reference plane of the shop from the measured signals.

The mentioned transfer functions contain S-parameters, which are a frequency domain representation of the behavior of the corresponding circuitry. To use the time-domain signal $v(t)$ captured by the oscilloscope together with the frequency domain transfer functions, it needs to be converted to its frequency domain representation $V(f)$. For this purpose, either a combination of linear interpolation and the Fourier transformation, or better the chirp Z transformation as described in Appendix A should be used. In the presented case I opted for the Chirp-Z transformation.

Bandpass filtering was used for noise reduction. To preserve the phase of the measured signal, zero phase filtering was conducted. After the signal was transformed to frequency domain and filtered, de-embedding was performed using (4.1) for the measurements of forward traveling waves, where \underline{V}_i is the vector containing the Fourier transformed signal measured at port i , \underline{G}_i is the transfer function from the chip to port i , and \underline{V}_{di} is the vector containing the de-embedded signal in frequency domain. For measurement of reflected waves the signal first needs to be de-embedded to the reference plane of the load, by using the transfer function \underline{G}_{j1} , and then to the chip as it is shown in (4.2). Due to the symmetry in the setup, the same de-embedding procedure applies to the second line of the differential pair. The inverse chirp Z transformation of \underline{V}_{di} yields the de-embedded time domain signal \underline{v}_{di} .

$$\underline{V}_{di} = \frac{\underline{V}_i}{\underline{G}_i} \quad i \in [1, 2, 4] \quad (4.1)$$

$$\underline{V}_{di} = \frac{\underline{V}_i}{\underline{G}_{i1} \underline{G}_1} \quad i \in [3, 5] \quad (4.2)$$

If the de-embedding was performed correctly, all the de-embedded voltage signals of the forward traveling waves should be the same up to a residual error introduced by the measurement noise and imperfections of the manufactured calibration standards. The same requirement applies for the reflected waves as well. In addition to the de-embedding of fixtures, also synchronization errors between the channels of the oscilloscope need to be accounted for. These constant timing differences can be measured and removed from the measurement results.

As it was the case for the signals coming from the chip, also the connected load impedance needs to be de-embedded. Based on these load reflection coefficients the impedance seen by the DUT can be derived.

For this task the six port S-parameters of the PCB (S_{PCB}) were reduced to two port S-parameters (S_T), leaving only the port of the chip (port 6) and port of the load (port 1). For this step, I assumed that the other ports are terminated with a perfect match. This is a valid assumption due to the good matching of the used terminations in combination with the low coupling coefficient between the lines. For the implementation of this process, the load S-parameter was extended to a 2x2 matrix as shown in (4.4). Then the concatenated response was derived by converting the S-parameters to T-parameters followed by a concatenation. The result of this concatenation yields the impedance presented to the chip.

$$S_{PCB} = \begin{bmatrix} S_{11} & \cdots & S_{16} \\ \vdots & \ddots & \vdots \\ S_{61} & \cdots & S_{66} \end{bmatrix} \rightarrow S_T = \begin{bmatrix} S_{66} & S_{61} \\ S_{16} & S_{11} \end{bmatrix} \quad (4.3)$$

$$S_L = S_{L11} \rightarrow S_L = \begin{bmatrix} S_{L11} & 0 \\ 0 & 0 \end{bmatrix} \quad (4.4)$$

4.1.3 De-Embedding Results

To validate the derived de-embedding approach, the residual error after de-embedding and synchronization was quantified. Therefore, the de-embedded signals of all ports measuring the forward traveling waves were compared to each other. Figure 4.12 presents the comparison of these signals. The signals of one line show a maximum amplitude difference of up to 5 % or 0.45 dB. The time delay between the signals was compensated to a value below 10 ps. For this calculation the mean of eleven pulses of the same preamble were used. Figure 4.13 shows a comparison of the signal measured at port 2 before and after de-embedding. In Figure 4.13 the magnitudes of the voltages of the de-embedded signals are scaled by a factor of about 10 relative to the original signals. This scaling corresponds to the chosen coupling factor of -20 dB. The result of measuring the signals at ports 1, 2 and 4 directly without de-embedding is shown in Figure 4.14. Figure 4.15 visualizes how the load impedance at port 1 (i.e. the input impedance of the corresponding oscilloscope channel) transforms to the reference plane of the chip. The area outside the transformed black smith chart represents impedances, which cannot be created at the chips reference plane, no matter which termination is used at the port. This is due to insertion loss of the PCB and connectors.

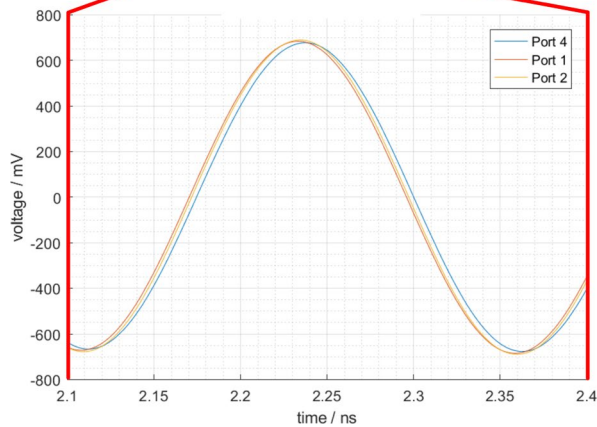
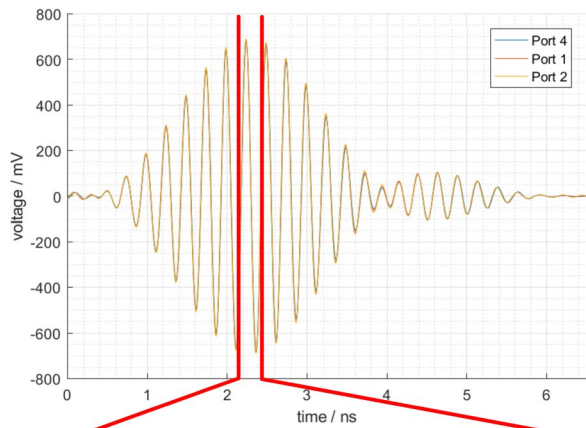


Figure 4.12. Comparison of different de-embedded signals as I presented in [67].

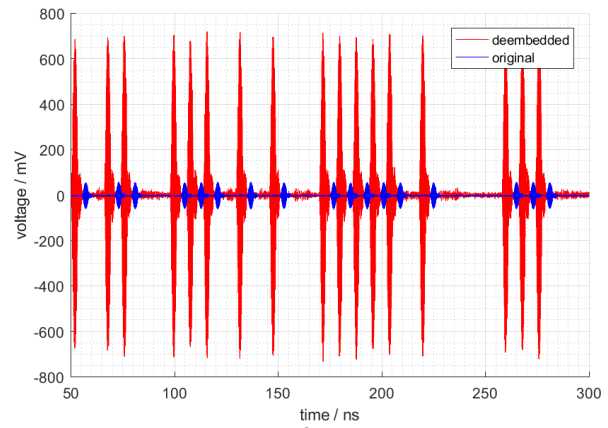


Figure 4.13. Comparison of signal measured at port 2 before and after de-embedding.

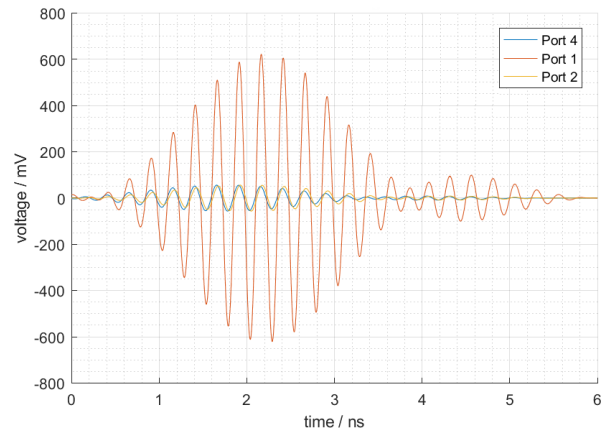


Figure 4.14. Comparison of signals at ports 1, 2 and 4 like I showed in [67].

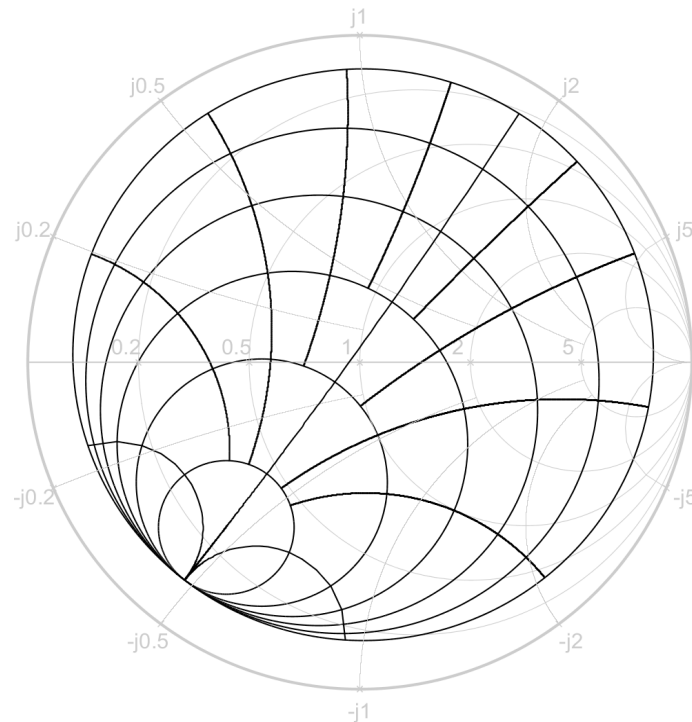


Figure 4.15. Transformation of load impedance from port 1 to the reference plane of the chip at 4.2 GHz. The grey lines show the impedance connected at the port, while the black lines show the impedance seen at the chip, as I showed in [67].

4.2 Mixed-Mode Load-Pull

When talking about mixed-mode load-pull the author talks of a load-pull setup capable of presenting different common mode and differential mode reflection coefficients to a DUT simultaneously. This might not be important for all devices, but for some the differential output signal depends on the common mode impedance presented to the device. This is caused by an unwanted common mode signal produced by the DUT, which is reflected to the DUT where it interacts with the device's output stage.

To fulfill the different characterization needs a variety of different approaches to this problem can be found in literature. For example the systems proposed in [10] and [11], use tuners at the output of the device under test (DUT) and a 180° hybrid at the differential input signal. Other approaches like in [12] or [13] use 180° hybrids also at the output of the device, but only to tune the differential mode load. Real mixed-mode load-pull measurement setups employing 180° hybrids can be found in [14] and [15]. As mentioned, passive load-pull systems are restricted in the available tuning range by the insertion loss in the load. Therefore, using a 180° hybrid in the load reduces the available load tuning range, resulting in mostly active mixed-mode load-pull systems being proposed showing all the benefits and disadvantages of an active load-pull system [16]. The author of this thesis presented a new approach to mixed-mode load-pull in [80] and [81]. This approach is discussed in Section 4.2.1. In Section 4.2.2 I present the impact of non-ideal 180° hybrids on mixed-mode load-pull setups. The measurement setups used to validate these analytical derivations are introduced in Section 4.2.3, followed by the measurement results in the Sections 4.2.4 and 4.2.5.

4.2.1 Load Configurations

In this section different load configurations for load-pull systems for differential devices are analyzed and compared using analytical derivations. For the following derivations generalized mixed-mode scattering parameters as summarized in [37] were used. Let us consider a setup that consists of a device under test (DUT), some connection network S_c and a load network S_L as depicted in Figure 4.16.

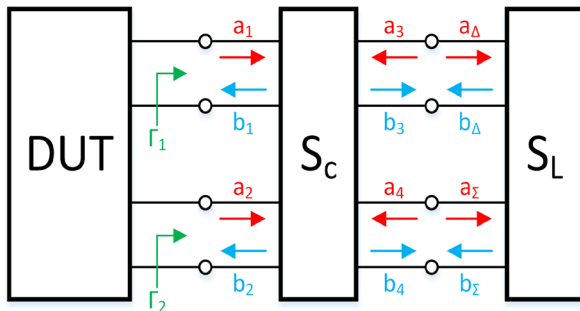


Figure 4.16. Block diagram of a generalized load network for devices with differential outputs, as I presented in [80].

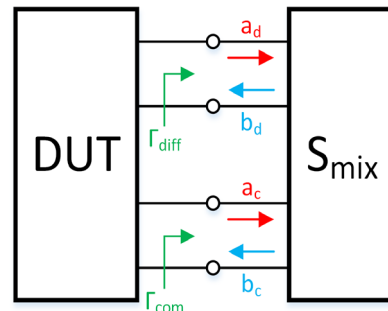


Figure 4.17. Block diagram of a load network for a device with differential output, simplified by using mixed-mode port representation, as I presented in [80].

The two waveguides connecting the differential output of the device form two ports. These two ports can either be represented by a differential mode port seeing a differential mode reflection coefficient Γ_{diff} and a common mode port seeing a common mode reflection coefficient Γ_{com} . In an equal manner, these two ports can be interpreted as two single ended ports seeing reflection coefficients Γ_1 and Γ_2 . For simplicity all single ended port reference impedances are chosen to be Z_0 . Differential port reference impedances are $Z_d = 2 \cdot Z_0$, and common mode port reference impedances are $Z_c = Z_0/2$. Furthermore, Z_0 is real and positive. The load network S_L has only two single ended ports named port Δ and port Σ as they will represent the impedance tuners connected to the Δ and Σ output ports of the

180° hybrid. For the observations in Sections 4.2.1a and 4.2.1b the tuners are terminated with a match and not connected to each other, resulting in a transmission coefficient with magnitude of zero in the load.

$$\underline{S}_L = \begin{bmatrix} S_\Delta & 0 \\ 0 & S_\Sigma \end{bmatrix} \quad (4.5)$$

Initially the connection network S_c is assumed to be a general 4-port network like shown in (4.6).

$$\underline{S}_c = \begin{bmatrix} S_{11} & S_{12} & S_{13} & S_{14} \\ S_{21} & S_{22} & S_{23} & S_{24} \\ S_{31} & S_{32} & S_{33} & S_{34} \\ S_{41} & S_{42} & S_{43} & S_{44} \end{bmatrix} \quad (4.6)$$

To concatenate two S-parameter blocks the multiport T-parameter transformation from [82] was used to get $\underline{S}_c, \underline{S}_L \rightarrow \underline{T}_c, \underline{T}_L$. The concatenated S-parameter block was then calculated by $\underline{T} = \underline{T}_c \cdot \underline{T}_L \rightarrow \underline{S}$

a. Directly Connected Tuners

Now let us consider three different ways of connecting tuners to a device under test. First, we look at the approach used in [10] and [11] where tuners are connected directly to a device under test. For this approach we assume that the connection network S_c is a direct connection from port 1 to port 3 and port 2 to port 4. The connection network is perfectly matched, reciprocal, lossless and has zero length. This results in the simplifications shown in (4.7).

$$\begin{aligned} S'_{11} &= S'_{22} = S'_{33} = S'_{44} = 0 \\ S'_{12} &= S'_{21} = S'_{34} = S'_{43} = 0 \\ S'_{14} &= S'_{41} = S'_{23} = S'_{32} = 0 \\ S'_{13} &= S'_{31} = S'_{24} = S'_{42} = 1 \end{aligned} \quad (4.7)$$

Using \underline{S} of the concatenated network and generalized mixed-mode scattering S-parameters from [37] we get the structure depicted in Figure 4.17 where \underline{S} has been transformed to its mixed mode representation \underline{S}_{mix} . This is exactly what we are really interested in, namely the differential and common mode reflection coefficients the device under test sees. If we put my simplifications from (4.7) into this new representation we arrive at the result shown in (4.8) and (4.19).

$$\underline{S}'_{mix} = \frac{1}{2} \cdot \begin{bmatrix} S_\Delta + S_\Sigma & S_\Delta - S_\Sigma \\ S_\Delta - S_\Sigma & S_\Delta + S_\Sigma \end{bmatrix} = \begin{bmatrix} S'_{dd} & S'_{dc} \\ S'_{cd} & S'_{cc} \end{bmatrix} \quad (4.8)$$

$$\Gamma'_{diff} = \Gamma'_{com} = S'_{dd} = S'_{cc} = \frac{S_\Delta + S_\Sigma}{2} \quad (4.9)$$

The matrix entries S'_{dd} and S'_{cc} of \underline{S}'_{mix} correspond to the differential and common mode reflection coefficients the device sees. S'_{dc} and S'_{cd} show the mode conversion that is introduced by the load. Because S'_{dd} and S'_{cc} are equal, the common and differential mode loads are always the same. This is not the desired behavior of a mixed-mode load-pull system as no independent tuning of the common and differential mode responses is possible. Additionally, mode conversion is introduced if S_Δ and S_Σ are not equal.

b. Connection Via a 180° Hybrid

To overcome the issues mentioned in the last paragraph we now look at a different approach. Here, the assumptions made for the connection network S_c have changed. This time we assume that the connection network is an ideal 180° hybrid as defined in (4.10). The results from (4.11) to (4.13) show

that differential and common mode reflection coefficients are completely independent of each other. Besides, they simply reduce to the reflection coefficients of the tuners and no matter how those are chosen mode conversion is never caused by the load. Another practical advantage is that measurements of the differential and common mode signals can be performed independently of each other at the corresponding port. If the common mode signal is not of interest, the output of the Σ -tuner can be terminated with a match and only the output of the Δ -tuner is measured to capture the differential mode signal. The disadvantage is an additional insertion loss of a real hybrid which reduces the tuning range for passive systems. Also the mode conversion is not zero due to the phase and amplitude imbalance in a real hybrid. Further information about the impact of a real hybrid is provided in Section 4.2.2.

$$\begin{aligned} S''_{11} &= S''_{22} = S''_{33} = S''_{44} = 0 \\ S''_{12} &= S''_{21} = S''_{34} = S''_{43} = 0 \\ S''_{13} &= S''_{31} = S''_{14} = S''_{41} = S''_{24} = S''_{42} = \frac{1}{\sqrt{2}} \end{aligned} \quad (4.10)$$

$$\begin{aligned} S''_{23} &= S''_{32} = -\frac{1}{\sqrt{2}} \\ \mathbf{S}''_{mix} &= \begin{bmatrix} S_{\Delta} & 0 \\ 0 & S_{\Sigma} \end{bmatrix} = \begin{bmatrix} S''_{dd} & S''_{dc} \\ S''_{cd} & S''_{cc} \end{bmatrix} \end{aligned} \quad (4.11)$$

$$\Gamma''_{diff} = S''_{dd} = S_{\Delta} \quad (4.12)$$

$$\Gamma''_{com} = S''_{cc} = S_{\Sigma} \quad (4.13)$$

c. Coupled Tuners

A third way of mixed-mode load-pull is to connect the outputs of the tuners to each other while the inputs are connected directly to the differential output of the device under test. This approach was first presented by the author in [80]. The resulting load matrix \underline{S}'_L provides non-zero transmission coefficients S_T as highlighted in (4.14). Performing the same calculations as before using the assumptions from (4.7) and (4.14) results in the mixed-mode network \underline{S}'''_{mix} summarized in (4.15) to (4.17). Compared to the results in Section 4.2.1a now different differential and common mode reflection coefficients can be realized. Yet, they cannot be selected independently from each other. The degree in which they are depending on each other can be tuned by the transmission coefficient S_T . Hence, it is more complicated achieving a specific combination of differential and common mode loads compared to the load-pull approach as discussed in Section 4.2.1b. Especially for manual tuners this is a problem because the parameters for a wanted pair of reflection coefficients cannot be found easily. On the one hand, setting the correct impedance at presented approach is more difficult. On the other hand, we do not need a 180° hybrid between the tuners and the chip. Additional tuning range can be traded in for ease of use.

$$\mathbf{S}'_L = \begin{bmatrix} S_{\Delta} & S_T \\ S_T & S_{\Sigma} \end{bmatrix} \quad (4.14)$$

$$\mathbf{S}'''_{mix} = \frac{1}{2} \begin{bmatrix} S_{\Delta} + S_{\Sigma} - 2 \cdot S_T & S_{\Delta} - S_{\Sigma} \\ S_{\Delta} - S_{\Sigma} & S_{\Delta} + S_{\Sigma} + 2 \cdot S_T \end{bmatrix} \quad (4.15)$$

$$\Gamma'''_{diff} = \frac{S_{\Delta} + S_{\Sigma}}{2} - S_T \quad (4.16)$$

$$\Gamma'''_{com} = \frac{S_{\Delta} + S_{\Sigma}}{2} + S_T \quad (4.17)$$

4.2.2 Impact of Non-Ideal 180° Hybrids

A non-ideal 180° hybrid featuring return loss, insertion loss, phase and magnitude imbalance as well as finite isolation causes a change of tuning range and is a source of mode conversion. In this section I discuss how each of the mentioned parameters affects the load tuning. For this discussion the differential input ports of the 180° hybrid are port 1 and port 2, the difference port is port 3 and the sum port is port 4, as it was already defined in (6). For demonstration of the impact I chose a reflection coefficient of $S_{\Sigma} = 0.6 \angle 20^\circ$ for the common mode tuner and a reflection coefficient of $S_{\Delta} = 0.8 \angle \varphi$ with $\varphi = 0 \dots 360^\circ$ for the differential mode tuner. A comparison of hybrid imperfection values used for figures and values taken from real devices can be found in Table 4.1. Please note that for the sake of demonstrating the impact of each individual parameter not all chosen values have practical relevance, but were chosen to deliver readable plots.

Table 4.1. 180° hybrid imperfection values used for the following graphs compared with real values [83]. Table contains values for insertion loss (IL), return loss (RL), isolation (ISO), magnitude imbalance and phase imbalance. Initially presented by me in [81].

	IL [dB]	RL [dB]	ISO _{DUT} [dB]	ISO _{Load} [dB]	Mag. Imb. [dB]	Phase Imb. [°]
values for plots	0.9	15	15	5	0.6	6
real values	0.2 – 1.9	15 - 25	23 - 35	23 - 35	0.1 – 0.8	2 - 6

a. Impact of Insertion and Return Loss

The first parameters I discuss are insertion loss (IL) and return loss (RL). The impact of insertion loss is visualized by the magenta colored arrows in Figure 4.18. As shown in (4.11), for an ideal 180° hybrid the differential and common mode impedances seen by the DUT (S_{dd} , S_{cc}) are equal to the impedances set at the corresponding tuners (S_{Δ} , S_{Σ}). Insertion loss reduces the magnitude of the set reflection coefficients S_{Δ} and S_{Σ} , thereby limiting the available tuning range. The light blue coloured arrows in Figure 4.18 demonstrate the influence of symmetric return loss at the ports facing the DUT. In this context symmetric means that the return losses at port 1 and port 2 have the same magnitude and phase ($S_{11} = S_{22}$). These return losses introduce additional reflections, which add to the reflections produced by the tuners, causing a shift of S_{dd} and S_{cc} which depends on the magnitude and phase of the return losses. As long as S_{11} and S_{22} are equal, no mode conversion occurs, and the impedance shift can be compensated by changing the values of S_{Δ} and S_{Σ} accordingly. The same behavior is caused by return loss at the ports facing the tuners. This again can be compensated by changing the tuner settings of each individual tuner.

Figure 4.19 shows the impact non-symmetric return loss ($S_{11} = -S_{22}$), which means the return losses at port 1 and port 2 are 180° out of phase. This influence is depicted by the magenta colored arrow. A 180° phase difference of the return losses causes a differential mode signal to be reflected as a common mode signal and vice versa. This causes mode conversion but does not directly influence S_{dd} and S_{cc} . The general case where S_{11} and S_{22} have different magnitude and phase causes a mixture of mode conversion and shift of S_{dd} and S_{cc} . Different to the shift of S_{dd} and S_{cc} , this type of mode conversion cannot be influenced by the tuners. Therefore, I refer to this as load independent mode conversion-

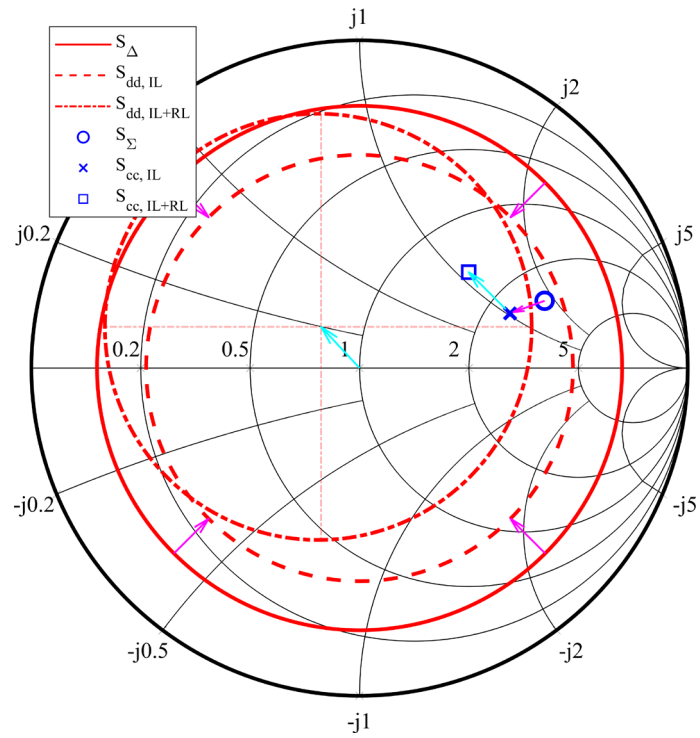


Figure 4.18. Impact of insertion loss and symmetric return loss on load tuning. S_{Δ} (solid red line) and S_{Σ} (blue circle) are the impedances set at the tuners. $S_{dd,IL}$ (dashed red line) and $S_{cc,IL}$ (blue cross) are the differential and common mode impedances seen by the DUT after the impact of insertion loss (IL). $S_{dd,IL+RL}$ (red dash-dotted line) and $S_{cc,IL+RL}$ (blue square) are the impedances seen by the DUT including the impact of insertion loss and symmetric return loss (RL), as in [81].

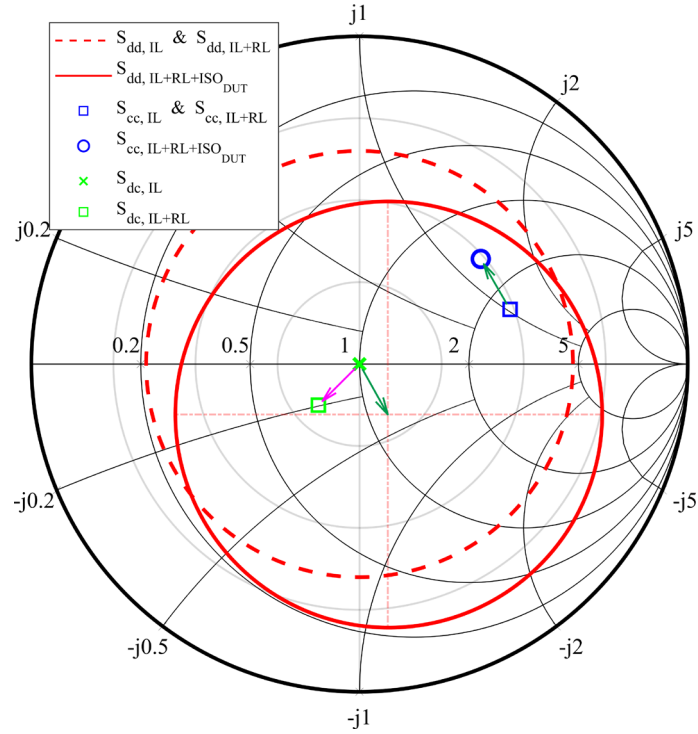


Figure 4.19. Impact of non-symmetric return loss and poor isolation between the ports facing the DUT. $S_{dd,IL}$ & $S_{dd,IL+RL}$ (dashed red line) are the differential mode impedances seen by the DUT including the impact of insertion loss (IL) and non-symmetric return loss (RL) respectively. Similarly $S_{cc,IL}$ & $S_{cc,IL+RL}$ (blue square) is the common mode impedance seen by the DUT including the impact of IL and non-symmetric RL respectively. $S_{dd,IL+RL+ISO_{DUT}}$ (solid red line) and $S_{cc,IL+RL+ISO_{DUT}}$ (blue circle) are the impedances seen by the DUT including the impact of IL, RL and finite isolation between the DUT ports (ISO_{DUT}). $S_{dc,IL}$ (green cross) and $S_{dc,IL+RL}$ (green square) are the mode conversion seen by the DUT considering IL and non-symmetric RL. Note that mode conversion is plotted in the overlying polar plot as it cannot be mapped to an impedance value, as presented in [81].

b. Impact of Finite Isolation

This sub section deals with the impact of finite isolation between the isolated ports of a 180° hybrid. At first the impact of poor isolation between the ports facing the DUT is marked by the green arrows in Figure 4.19. For S_{cc} poor isolation causes the same shift as a symmetric return loss. This is because the incoming signals which make up the common mode signal are equal, therefore a reciprocal transmission from port 1 to port 2 cannot be distinguished from a symmetric return loss with same phase and magnitude. The only parameter changing S_{dd} is the additional 180° phase shift is introduced because the incoming signals at port 1 and port 2 are 180° out of phase. This causes the green arrows in Figure 4.19 to point in opposite directions. This shift of S_{dd} and S_{cc} can be compensated by the tuners in the same way as symmetric return loss. Beside of this effect, there is also the impact of finite isolation between the ports facing the tuners. The influence of this is shown in Figure 4.20. Because of this imperfection, reflections of one tuner carry over to the other tuner, causing a coupling between the two tuners. On the one hand, this causes mode conversion which depends on the tuner settings, later referred to as load dependent mode conversion. And on the other hand, it leads to differential and common mode impedances (S_{dd} , S_{cc}) which now depend on both tuners (S_{Δ} , S_{Σ}). In the example shown in Figure 4.20 this causes S_{cc} to become a circle in the Smith chart if the phase of S_{Δ} is swept from 0 to 2π . In order to compensate for this behavior, one would need to tune both tuners jointly, thereby losing one of the key benefits of using a 180° hybrid. Please note that especially in the case of isolation I chose unrealistic values to produce readable plots. As shown in Table 4.1 isolation values are much better than most other imperfections and often can be neglected.

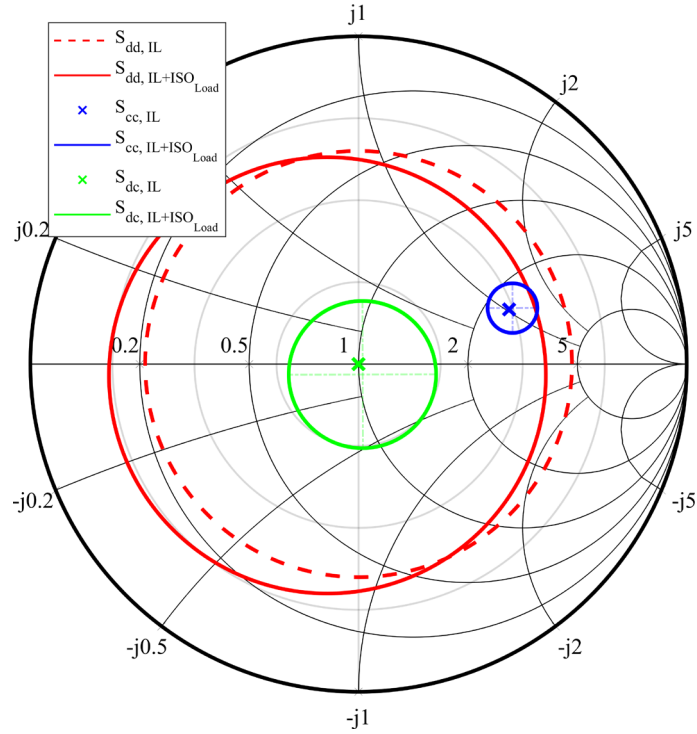


Figure 4.20. Impact of poor isolation between the load ports 3 and 4 of the 180° hybrid. $S_{dd,IL}$, $S_{cc,IL}$ and $S_{dc,IL}$ are the impedances and mode conversion seen by the DUT including the impact of insertion loss. $S_{dd,IL+ISO_{Load}}$, $S_{cc,IL+ISO_{Load}}$ and $S_{dc,IL+ISO_{Load}}$ are the impedances and mode conversion seen by the DUT considering insertion loss and isolation, which were presented by me in [81].

c. Impact of Magnitude and Phase Imbalance

As last point, I discuss the impact of magnitude and phase imbalance between the transmission parameters of a 180° hybrid. A hybrid has four transmission parameters, and in general each of them may have a different magnitude and phase error relative to the ideal value. This makes it impossible to pick a single set of errors representative for all possible combinations and thus forcing us to rely on Monte Carlo simulations. For the simulations, I assumed that the magnitude errors and the phase errors are equally distributed between the given errors bounds mentioned in Table 4.1. This assumption is valid because we are only interested in finding an upper error bound and assume that the specifications are not exceeded. For this investigation I chose a fixed S_Δ of approximately -2 dB and swept the magnitude of S_Σ from -15 dB to 0 dB. The results of this simulation using 5000 different combinations are presented in Figure 4.21. As you can see magnitude and phase imbalance causes mode conversion and a detuning of the set impedances. What you cannot see in this plot is that, like for poor isolation at the ports facing the tuners, imbalance is causing a dependency of the common and differential mode on both tuner settings as well as load dependent mode conversion. Resulting in the need to tune both tuners jointly to compensate the imperfections of the hybrid.

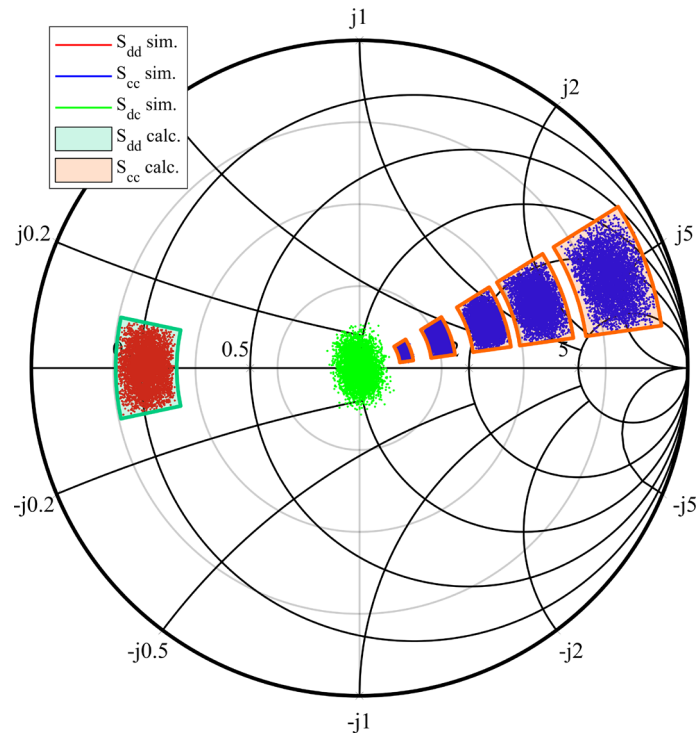


Figure 4.21. Comparison of simulated and calculated impact of magnitude and phase imbalance. S_{dd} and S_{cc} show the differential and common mode impedances seen by the DUT. The appendixes “sim.” or “calc.” indicates the simulated points using Monte Carlo simulation or the calculated area using the simplified formulas (4.18) and (4.19). S_{dc} shows the mode conversion due to magnitude and phase imbalance using Monte Carlo simulation only, as shown in [81].

d. Hybrid Tuning Error Estimation

As already mentioned I deliberately did not always use realistic values for the plots mentioned in the sections above. But in this section, I elaborate on which parameters you need to consider most when purchasing a real 180° hybrid for mixed-mode load-pull measurements. The first parameter I discussed was the insertion loss, which causes a significant decrease in tuning range. Especially for passive load-pull systems, this is a critical value if you aim to achieve high reflection coefficients. Differently symmetric return loss does not decrease your tuning range, but shifts it depending on its phase and magnitude. Inside the available tuning range, this shift can be compensated with the corresponding tuner. Asymmetric return loss causes mode conversion, but with average return losses between 15 dB and 25 dB the reduction in tuning range is not as severe as in the case of insertion loss. The next discussed parameter was the isolation, which may cause impedance shifts, dependency of S_{dd} and S_{cc} on both tuners as well as load dependent mode conversion. However, as average isolation values are rather high in a range from 23 dB to 35 dB they can often be neglected compared to the impact of the other imperfections. Other than isolation, realistic values of magnitude and phase imbalance may have a severe impact on the performance of a 180° hybrid. Imbalance may cause a significant dependency of S_{dd} and S_{cc} on both tuners as well as load dependent mode conversion. To compensate for this a joint tuning of both tuners is needed, making the handling of the tuning setup much more complicated. If a joint tuning is not wished one needs to analyze if the impact of a hybrids imperfections is in an acceptable range. To assist the reader with this decision I derived the simplified formulas (4.18) and (4.19), describing the impact of a 180° hybrid’s imperfections on S_{dd} and S_{cc} , using the afore mentioned considerations. Compared to the ideal results of (4.11) these formulas include the impact of the most important imperfections, which are the insertion loss IL , the magnitude error Δ_m and the phase error Δ_φ , and have been simplified to achieve an easily useable rule of thumb. A validation of these formulas is presented in Figure 4.21 and Figure 4.22. To achieve this high degree of simplification

some assumptions were made. At first isolation and return loss were neglected as the impact of isolation is small and impedance shift due to return loss can be easily compensated. Also higher order terms and products were eliminated from the equation. At last, the different error terms were combined in a way to derive an upper error bound. Due to these simplifications, the formula does fail to deliver an upper error bound if the ratio between the magnitudes of the set reflection coefficients at the tuners is becoming larger than 20 dB as shown in Figure 4.22. This is valid for realistic parameters as mentioned in Table 4.1. The reader can now utilize these formulas to calculate areas in the Smith chart by using the four combinations of positive and negative magnitude and phase errors. These areas indicate how S_{dd} might change due to a change of S_{cc} and vice versa. If the resulting area is small enough for the desired application the reader may consider to use the corresponding 180° hybrid and independently tune S_{dd} and S_{cc} by using one tuner for each. Otherwise, a joint tuning of both tuners needs to be performed which is significantly more complicated especially with manual tuners.

$$\tilde{S}_{dd} = S_{\Delta} \cdot (1 + 2\Delta_m) \cdot IL^2 \cdot e^{i2\Delta\phi} \quad (4.18)$$

$$\tilde{S}_{cc} = S_{\Sigma} \cdot (1 + 2\Delta_m) \cdot IL^2 \cdot e^{i2\Delta\phi} \quad (4.19)$$

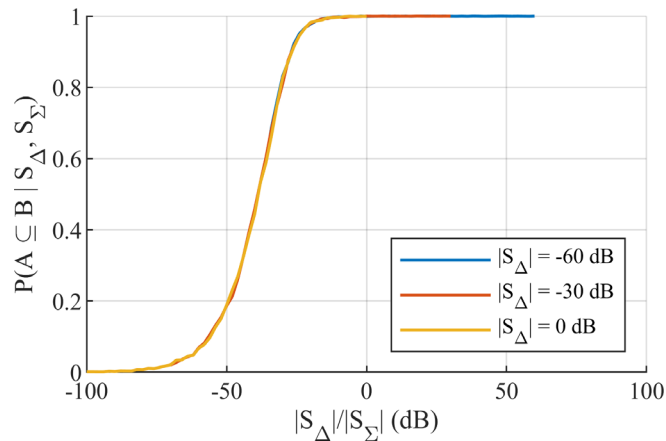


Figure 4.22. Analysis of the probability that the derived rule of thumb in (4.18) and (4.19) covers all possible combinations assuming the errors are uniformly distributed within the specified range. $P(A \subseteq B | S_{\Delta}, S_{\Sigma})$ being the probability that the results of the Monte Carlo simulation (A) are a subset of the area specified by the formula (B) for a given pair of tuner reflection coefficients. For this a larger number of 50 000 realizations of the Monte Carlo simulation were used. The x-axis indicates the difference in magnitude between the reflection coefficients set at the two tuners. To demonstrate the full shape of the curve values down to -100 dB are plotted, although they cannot be realized in a real-world scenario. This was initially presented by me in [81].

4.2.3 Measurement Setups

According to the derivations in Section 4.2.1, the following setups were designed to support the analytical findings with measurement results. The used R&S ZVA 24 VNA was calibrated using a R&S Auto Calibration Unit. The reference planes for the measurements were at the input ports of the load network, which is either at the ports of the tuners or if used at the ports of the 180° hybrid.

a. Setup with Direct Connection

A load-pull setup using directly connected tuners is shown in Figure 4.23. This setup does not use a 180° hybrid, but as derived it is also not able to provide different common mode and differential mode load impedances to the DUT. For the results presented in Section 4.2.4 a VNA was used to measure the load impedance seen by the DUT.

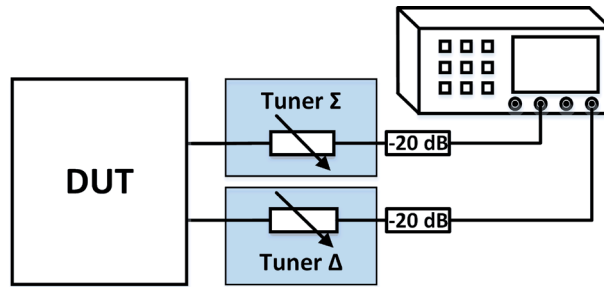


Figure 4.23. Load-pull setup with directly connected tuners and measurement device, as in [81].

b. Setup with 180° Hybrid

The setup in this section utilizes a 180° hybrid as depicted in Figure 4.24, like it was presented in [15] and [80]. As derived in this setup common and differential mode loads can be set independently with the two tuners. For load-pull measurements, the output of the differential mode load tuner would be fed to a spectrum analyzer via an attenuator for better matching. For the measurement results in Section 4.2.4 again a VNA was used to measure the load impedance a DUT would see.

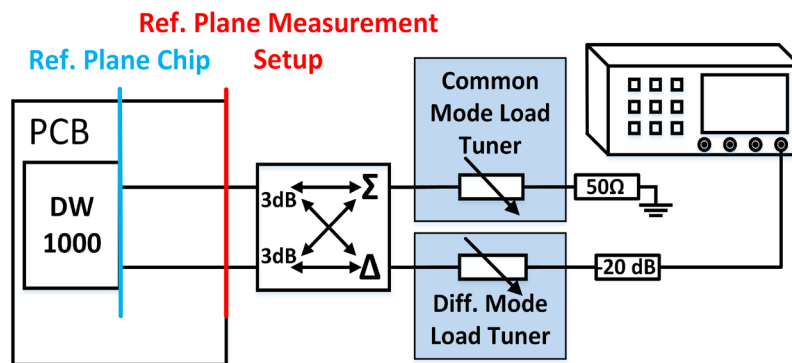


Figure 4.24. Load-pull setup with a 180° hybrid as connection network, as in [81].

c. Setup with Connected Tuners

Figure 4.25 and Figure 4.26 show the measurement setup with connected tuners proposed by the author in [80]. In contrast to the setup depicted in Figure 4.24 no 180° hybrid is used, but the ports of the tuners that do not face the DUT are now connected to each other. This connection can be adjusted in magnitude and phase. Ideally, one would use an adjustable reciprocal phase shifter with low insertion loss or a line stretcher in the connection path between the tuners, but such equipment was not available to us. To circumvent this SMA female-female and male-male adapters were used to adjust the electrical length of the connection between the tuners. As the behavior of the linear load network and not the characterization of some DUT was of interest, an R&S ZVA Vector Network Analyzer (VNA) was used (see Figure 4.25). To perform load-pull measurements with a DUT directional couplers would be needed as shown in Figure 4.26. Note that the additional insertion losses of the directional couplers in Figure 4.26 mainly influence the parameter S_T used to tune the difference between differential mode and common mode reflection coefficient and not the maximum achievable reflection coefficients.

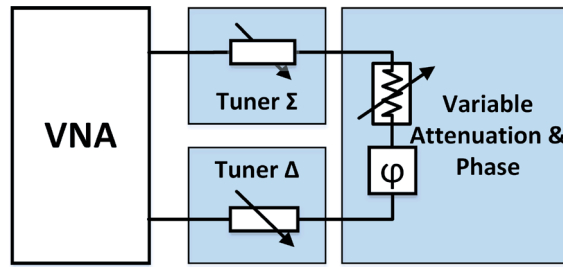


Figure 4.25. Measurement setup used to measure the tuning behavior of the load network with connected tuners, like shown [81].

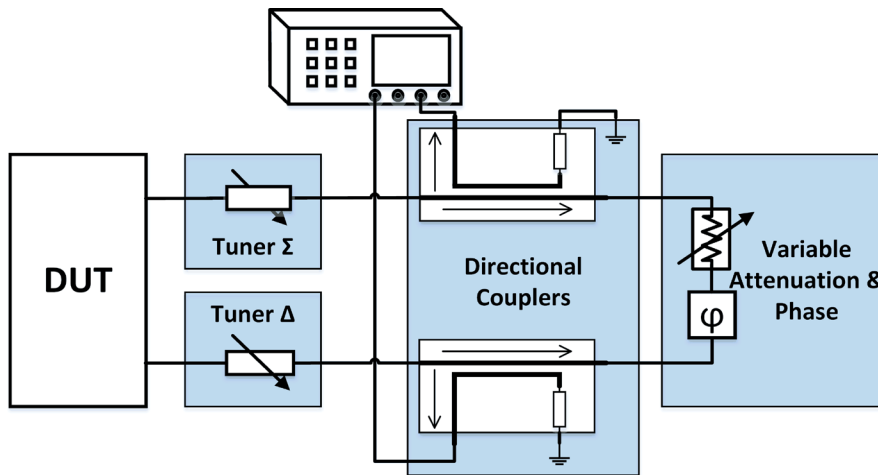


Figure 4.26. Diagram of a load-pull setup utilizing a load network with connected tuners to characterize a DUT, as presented in [81].

4.2.4 Results for Load Networks

In this section, I discuss the tuning range and behavior of each presented setup. For this purpose, the screws used to tune the magnitude of each tuner's reflection coefficient were set to the same values, in a way to achieve the highest possible magnitude of the reflection coefficient. Then the positions of each tuner's slide were swept and the changes to the differential and common mode reflection coefficients were captured. The results are visualized in Smith charts. For every measurement presented in this section a frequency of 4 GHz was used.

Figure 4.27 demonstrates the difference in tuning range between direct connected tuners (see Section 4.2.3a) and a setup using a 180° hybrid (see Section 4.2.3b). The maximum magnitude of the differential mode reflection coefficient for the setup with direct connected tuner is about 0.85. For the setup using a hybrid it reduces to about 0.77. The common mode reflection coefficient without a 180° hybrid is always equal to the differential mode reflection coefficient. With a 180° hybrid the common mode reflection coefficient can be tuned independently and was set to a low reflection coefficient of $S_{cc} = 0.025 + j 0.015$.

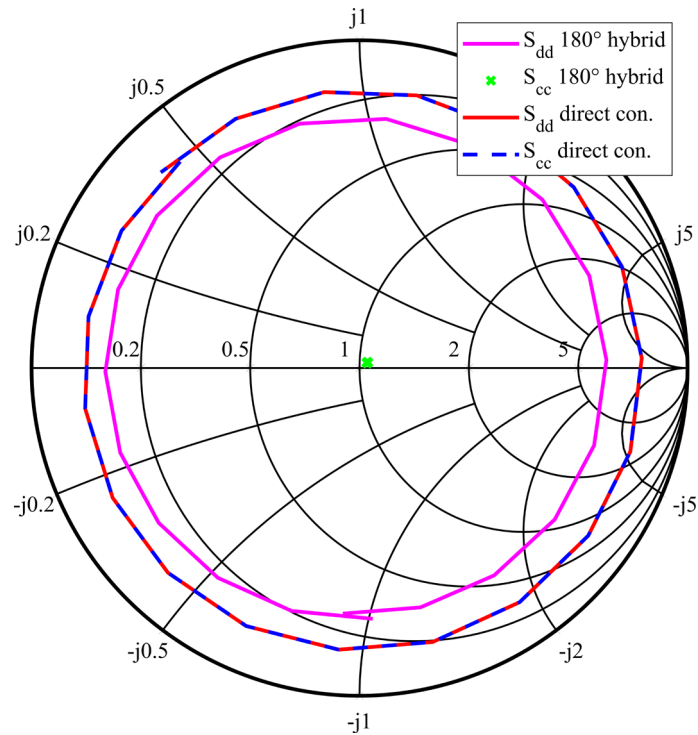


Figure 4.27. Comparison of possible differential and common mode reflection coefficients for the setup with separated tuners and the setup facilitating a 180° hybrid. For the setup using the 180° hybrid the Σ -Tuner was set to achieve a good common mode matching. [81]

The following figures show measurement results of the tuning behavior of the proposed setup using tuners, which are connected to each other. Figure 4.28 shows the impact of a change of attenuation in the connection path. The maximum differential and common mode reflection coefficients which can be achieved with this setup have a magnitude of about 0.94. At the same time, it is possible to set the reflection coefficient of the other mode to a low value. The numbers 1 and 2 in the circles in Figure 4.28 indicate specific tuner slide positions. The positions of the slides on each load were kept the same. If this were not the case, mode conversion would be generated in the load.

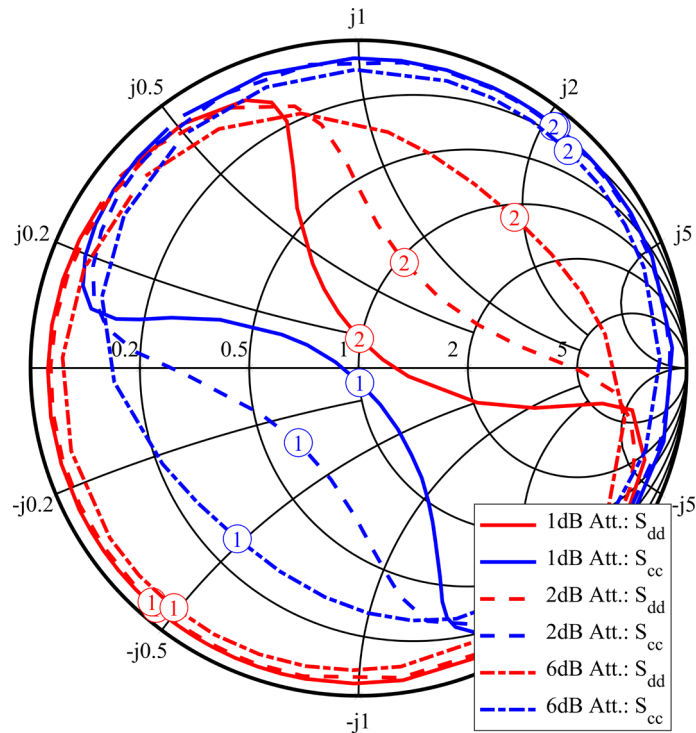


Figure 4.28. Impact of attenuator values on the mixed-mode reflection coefficients. The red lines show the change of the common mode reflection coefficient, while the blue lines show the differential mode reflection coefficients. The solid, dashed and dotted-dashed lines have been captured using different attenuator values in the connection path between the tuners. The circles with the numbers 1 and 2 indicate specific slide positions of the tuner. [81]

The impact of a phase or delay change in the connection path between the tuners is shown in Figure 4.29. As we are only looking at one frequency, a change in delay has the same effect as a phase shift. An increase in delay causes the Smith chart to rotate clockwise. Each extension also introduces some attenuation, changing the magnitude of the mixed-mode reflection coefficients.

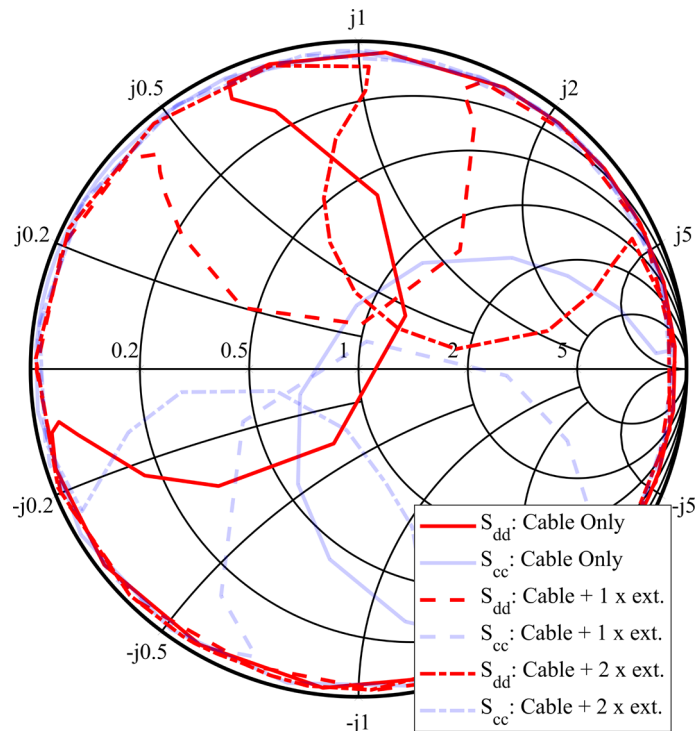


Figure 4.29. In this plot the electrical length of the connection path between the tuners was changed. The solid line shows the result for an SMA cable, for the dashed line the cable was extended with a female-female and male-male adapter. An additional extension was added for the dotted-dashed line. [81]

a. Discussion of Load Network Results

The maximum achievable reflection coefficients of the proposed setup depend on the chosen attenuation value in the connection path. By comparing Figure 4.27 and Figure 4.28 it can be observed that the setup with connected tuners achieves higher magnitude reflection coefficients compared to the setup with directly connected separated tuners. In all presented cases, the maximum achievable reflection coefficients of the proposed setup were higher than what could be reached with traditional setups, while maintaining the possibility to tune the reflection coefficient of the other mode. For example, it can achieve low reflection coefficients for the other mode, similar to the setup with the 180° hybrid shown in Figure 4.27. As shown in Figure 4.29 the phase of the reflection coefficients can be tuned by adjustment of the delay or phase shift in the transmission path between the tuners. As long as the attenuation in the transmission path is not changed, the magnitude of the reflection coefficients is not influenced. The disadvantage compared to a setup using a 180° hybrid is that the reflection coefficients cannot be tuned independently, and achieving reflection coefficients in the other half of the Smith chart is limited by the minimum attenuation value in the connection path and the transmission coefficients of the tuners. These two factors mainly influence the magnitude of the transmission coefficient of the load network as described in (4.14)-(4.17), and this transmission coefficient determines the difference between differential and common mode reflection coefficient. Also not all combinations of differential and common mode reflection coefficients can be generated using the proposed setup.

The analytical results presented in (4.14)-(4.17) describe quite well how the setup can be used in practice. Using fixed settings for the tuners, the magnitude of S_T can be controlled via the attenuation value in the setup. The lower the attenuation, the higher the magnitude of S_T and the larger the difference between differential and common mode reflection coefficient. This behavior is presented in Figure 4.28. The phases of the differential and common mode reflection coefficients are directly influenced by the phase of the transmission coefficient. This behavior is represented in Figure 4.29.

A drawback of this setup is that the tuning process is more complicated because of the two additional parameters (attenuation and phase) in the connection path. Nevertheless, if the tuning behavior as shown in Figure 4.28 and Figure 4.29 is known to the user, also manual tuners can be used in combination with this setup with only a minimum of additional effort. If automatic tuners are available, a pre-characterization of the setup significantly speeds up the tuning process for follow-up measurements. The reader should also keep in mind, that this setup does not produce any mode-conversion if the two tuners' settings are equal. This behavior is the same as it was derived for the setup with directly connected tuners in (4.8).

4.2.5 Results of Mixed-Mode Load-Pull Measurements

This section presents load-pull measurement results using the Decawave® DW1000 chip as DUT. The first measurements were conducted at $100\ \Omega$ differential and variable common mode load. The differential mode output power of the chip changed by a maximum of 0.15 dB for any provided common mode load. The second set of measurements was done using a $25\ \Omega$ common and variable differential mode load. Table 4.2 shows measurement results for each frequency. The column named channel corresponds to the channels as they are listed in [55] while the mentioned frequencies are the center frequencies of these channels as well as the frequencies of the used continuous wave signal. The power values are the maximum achievable power compared to the power when using a $100\ \Omega$ differential load. Z_{diff} is the differential impedance at the reference plane of the chip for which the maximum output power has been measured. No extrapolation was applied on the measured data. Figure 4.30 and Figure 4.31 show results of load-pull measurements for channel 1 and channel 2. Small grey crosses indicate the measured impedance points at the reference plane of the chip.

The influence of the common mode load on the differential mode signal is below 0.15 dB. Therefore, the impact of common mode load on this device is not further discussed. It has to be mentioned, that this is only valid for this device and that there may be devices that react sensible to different common mode loads. Looking at the differential mode load-pull measurements we notice that the chip is not matched exactly to 100Ω differential. The reflection coefficient resulting in the highest output power for channel 1 can be found easily, because it is inside the available tuning range. For channel 2 and channel 3 they are outside the tuning range. But even the best points that could be measured yield an increase in output power of 1.27 dB for channel 1 up to 5.12 dB for channel 3. To find the optimum load the insertion loss needs to be decreased by placing the chip on a printed circuit board without other unnecessary structures. Due to this additional insertion loss of the PCB and the little impact of different common mode loads, this DUT is not the best choice to support the analytical results derived in Section 4.2.1, nevertheless it could be shown the provided results show that additional off-chip matching can be beneficial.

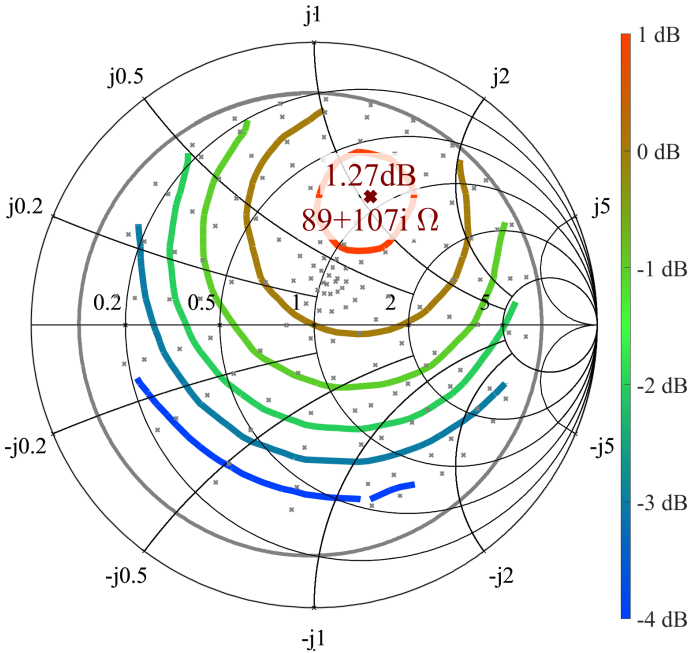


Figure 4.30. Load-pull contour plot of a DW1000 chip for channel 1. The matching point is inside the tuning range of the load-pull setup, as I presented in [80].

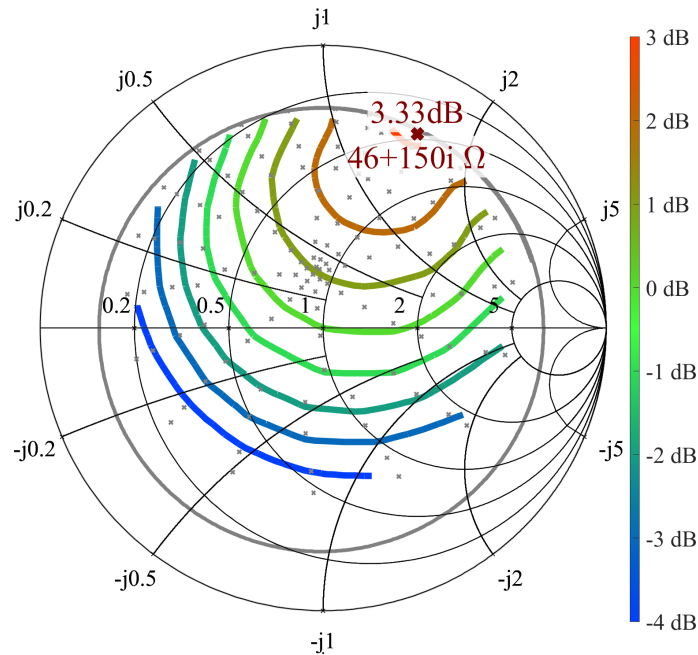


Figure 4.31. Load-pull contour plot of a DW1000 chip for channel 2. The optimum matching point is not inside the tuning range of the load-pull setup, as I showed in [80].

Table 4.2. Load-pull measurement results of the DW1000 chip in CW mode for three different frequencies. Max. Power is the maximum power gain, which can be achieved with an additional matching network instead of a 100 Ohm differential matching. [80]

Channel	Center Frequency [MHz]	Max. Power [dB]	Zdiff [Ω]
1	3494.4	1.27	89 + 107i
2	3993.6	3.33	46 + 150i
3	4492.8	5.13	50 - 90i

4.3 Wideband Load-Pull

In the last two sections, I showed how mixed-mode load-pull measurements can be performed for continuous wave (CW) signals. As the topic of this thesis is UWB-IR, which uses short wideband pulses, I was curious about how appropriate it is to characterize such a device using CW signals. It might come to one's mind that multiple independent CW load-pull measurements spanning the frequency band utilized by the DUT can be combined to achieve the same result as if wideband signals were used. There is a simple example, which demonstrates that this is not necessarily the case. Consider a DUT connected to some load via an ideal transmission line with a length of 0.5 m. For simplicity we assume a propagation along the line with the speed of light. If the DUT sends an UWB pulse with a length of 2 ns, the corresponding length in space is about 60 cm. The distance to the load and back to the DUT is 1 m. This means, the DUT already stopped generating the pulse before the reflection from the load even arrived at the DUT's output. Assuming that the time between pulses is much higher than the pulse duration the DUT will always see a perfect match while transmitting a pulse. Of course, in most real-world applications, the distance from the chip to the antenna is much shorter, but under laboratory conditions, for example by using the load-pull setups presented in the last two sections (see Figure 4.5 and Figure 4.8), I was able to reproduce this behavior. This brought me to the question, I

would like to answer in this section: How can wideband load-pull measurements be performed under laboratory conditions?

4.3.1 Keeping Distances Short

One approach to solve this problem is keeping the electrical distances between the DUT and load as short as in the final application. For this investigation, I was not able to use the existing DUT featuring rather long lines on the PCB (see Figure 4.8) and mechanical tuners (Figure 4.2) with a physical dimension of about 30 cm. Instead, a HMC311SC70 amplifier from Analog Devices® was placed on a PCB made of RO4350B substrate as shown in Figure 4.34 and used as DUT. The thin stub line you can see in Figure 4.34 was not used for the following measurements and therefore was terminated with a match. To adjust the load reflection coefficient Γ and T matching networks on FR4 substrate were used, which are placed in between the DUT's output and the oscilloscope. A block diagram of this setup is shown in Figure 4.32. The baseband signal is generated by a Tektronix AWG7102 arbitrary waveform generator (AWG), using a 20 GS/s sample rate with 10-bit resolution. The baseband signal is mixed to a chosen center frequency and adjusted in power using a R&S SMBV100 signal generator. The generated bandpass signal is then split using a 6 dB power splitter, one part of the signal is then fed directly to a R&S RTO1044 real-time oscilloscope as a reference signal, while the other part is used as input signal for the DUT. Knowing that the power splitter is electrically small and highly symmetrical I consider the captured reference waveform to be equal to the waveform at the input of the DUT. The output of the combination of DUT and matching network is then also fed to the oscilloscope. The peak output power at the signal generator was set to 0 dBm. After the splitter and connections this results in a peak power level of about -7 dBm at the amplifier. With a $P_{1dB_{input}}$ of 0 dBm the amplifier operates in its linear range. This power level was also chosen to operate in the higher sensitivity input range of the oscilloscope resulting in better SNR for the measurements. Figure 4.33 shows a photo of the measurement setup and Figure 4.34 shows a photo zoomed in to the connection between DUT and matching network. The connection between the DUT and load (in this case the matching network) is only 5 cm. According to this, a signal launched at the DUT's output needs about 0.24 ns to arrive at the load. For this calculation we assumed a propagation velocity of 0.7 times the speed of light. This slowing of the signal is caused by the permittivity of the dielectric inside the used SMA cables. At the load, the signal is reflected taking another 0.24 ns to arrive again at the output of the DUT, resulting in a roundtrip time of about 0.5 ns. By looking at Figure 4.35 it can be seen that the roundtrip time of about 0.5 ns is less than the duration of the pulses envelope, therefore some influence on the DUT due to different loads should be observable.

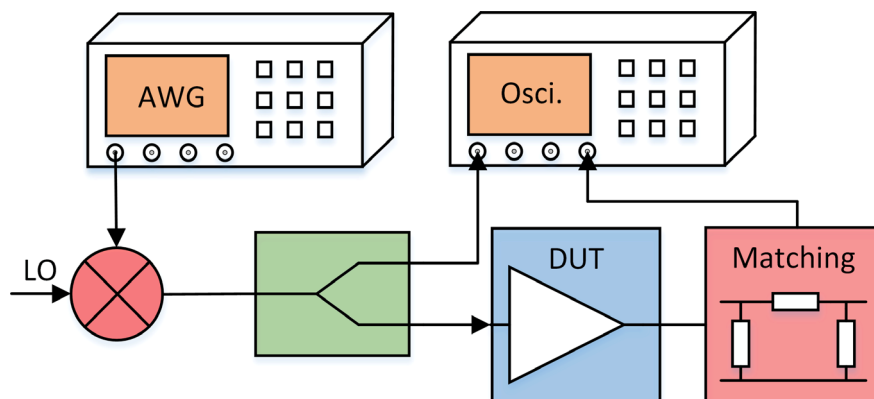


Figure 4.32. Block diagram of the measurement setup used to perform load-pull measurements with short electrical length between DUT and load / matching network.

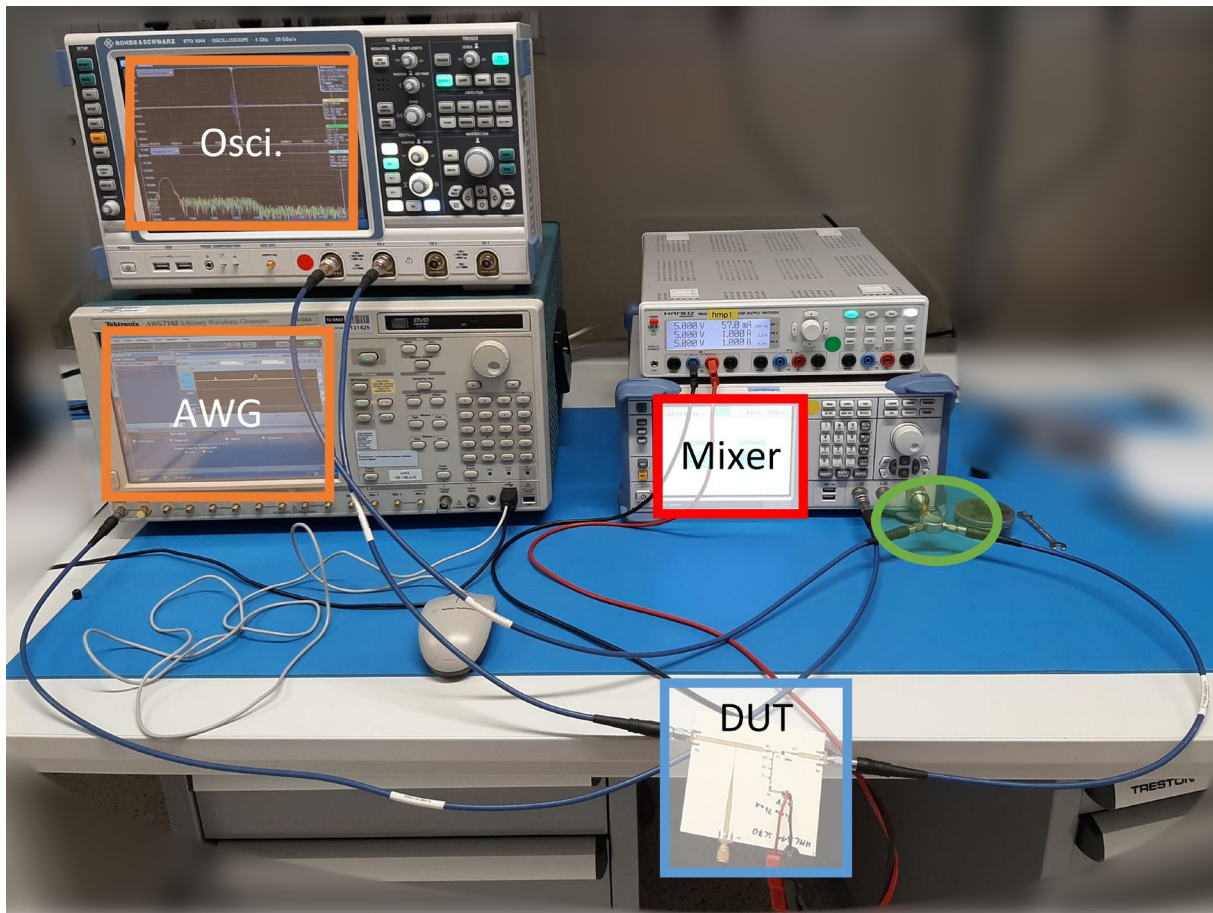


Figure 4.33. Photo of real measurement setup used to perform load-pull measurements with short electrical distance to load. This image does not show a matching network as it was the setup used to measure the DUT's behavior with a $50\ \Omega$ match. To see how the DUT is connected to the matching network please look at Figure 4.34.

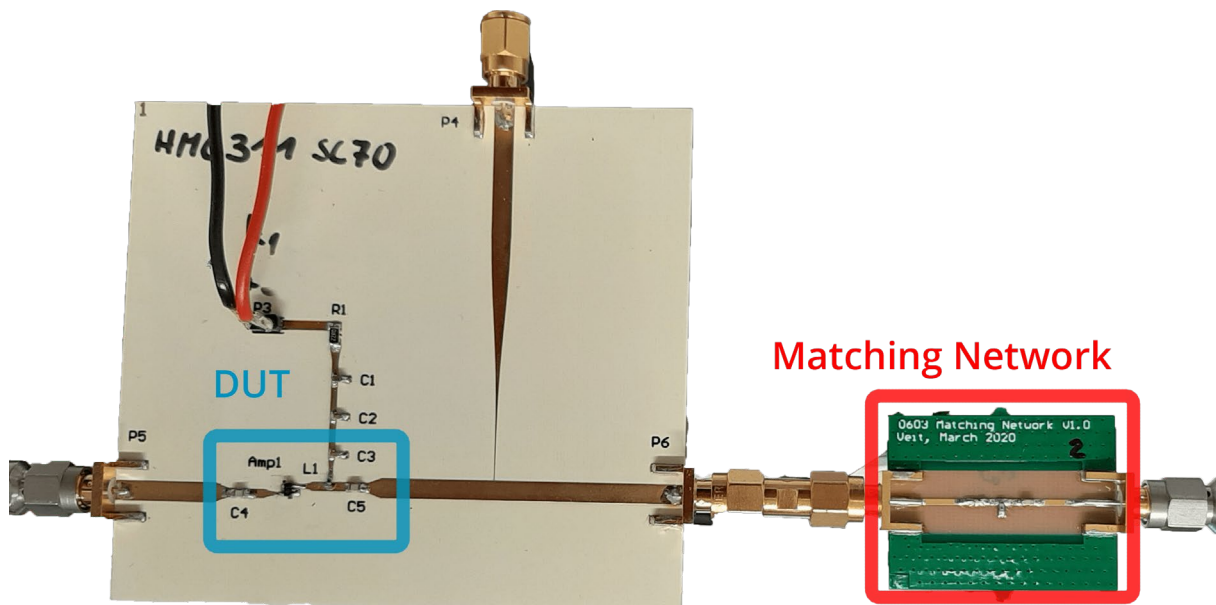


Figure 4.34. DUT and matching network for load-pull measurements with short electrical length to load.

a. Measurement Results

At first, I would like to mention that for the following measurements an UWB pulse shape resulting in a bandwidth of 500 MHz at a center frequency of 1.5 GHz was chosen. Figure 4.35 shows the result

obtained from a single measurement realization consisting of the transmission of a single pulse. The green line indicates the waveform provided to the AWG, the red lines show the bandpass signal and envelope of the reference waveform going from the power splitter to the oscilloscope and the blue lines are the bandpass signal and envelope obtained from the DUT's output. In a post processing step the waveforms were aligned on the time axis according to the maximum of their calculated envelope for easier comparison.

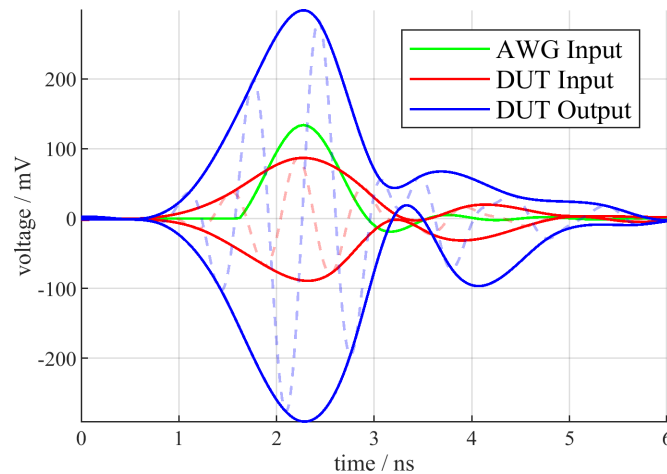


Figure 4.35. Comparison of different time domain waveforms for matching network #6. The green line is the digital waveform passed to the arbitrary signal generator. The solid red line is the envelope of the bandpass signal at the input of the DUT, the dashed red line is the bandpass signal itself. In comparison the blue lines indicate the corresponding signals at the output of the DUT.

To analyze the stability of the whole setup Figure 4.36, Figure 4.37 and Figure 4.38 show histograms of the fidelity factor, RMS power gain and peak power gain for 100 measurement realizations each using a single pulse. This evaluation was performed for each of the nine setups, where setup 1 is a direct connection from DUT to the oscilloscope (see Figure 4.33) and the other setups are using different matching networks (see Figure 4.34). Smith Charts showing the reflection coefficients corresponding to the used matching network are shown later. Figure 4.36 presents the results for the fidelity factor calculated as in (3.28) using the bandpass reference signal (dashed red line) and the bandpass output signal (dashed blue line). It can be observed that the results show a variance of about 0.1 for fidelity factors of 0.9 and above. For lower fidelity factors the variance increases. Matching networks 3 and 4 resulted in such low power values that they are not shown in the histograms and removed from the analysis of wideband signals, but they are shown in Figure 4.41 for comparison with CW signals.

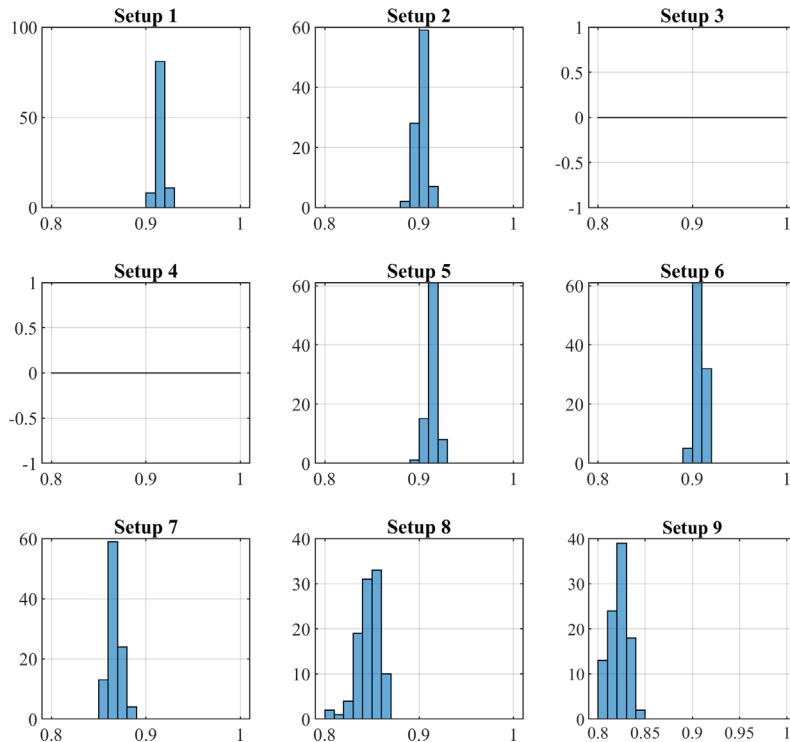


Figure 4.36. Statistical analysis of the fidelity factor for different matching networks using a center frequency of 1.5 GHz and a 500 MHz pulse as described in Figure 4.35.

Figure 4.37 shows the same statistical evaluation for the RMS power gain while Figure 4.38 presents the results for the peak power gain. Both figures show a similar variance of about 0.5 dB to 1 dB with nearly identical mean values.

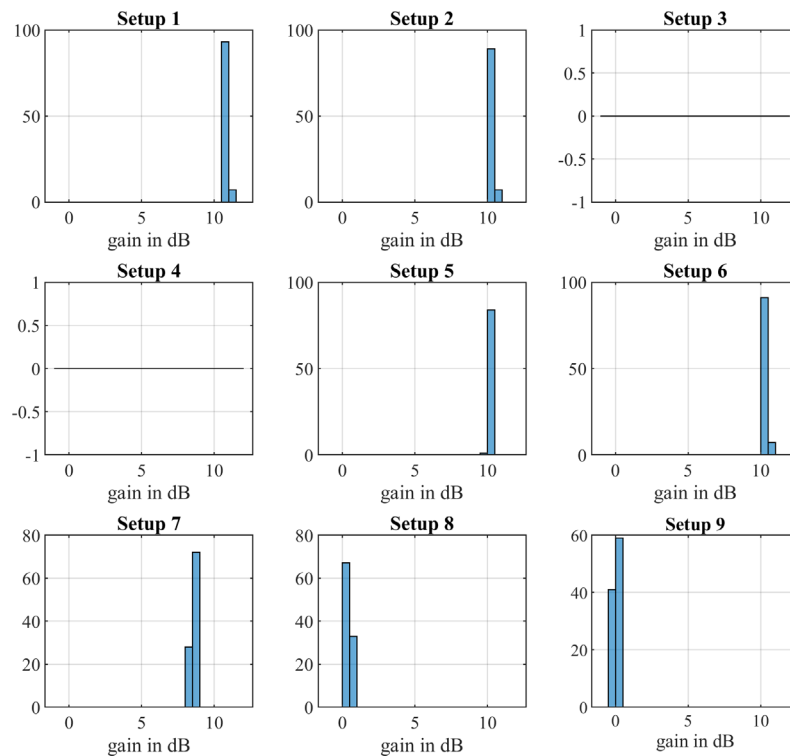


Figure 4.37. Statistical analysis of the RMS power gain for different matching networks using a center frequency of 1.5 GHz and a 500 MHz pulse as described in Figure 4.35.

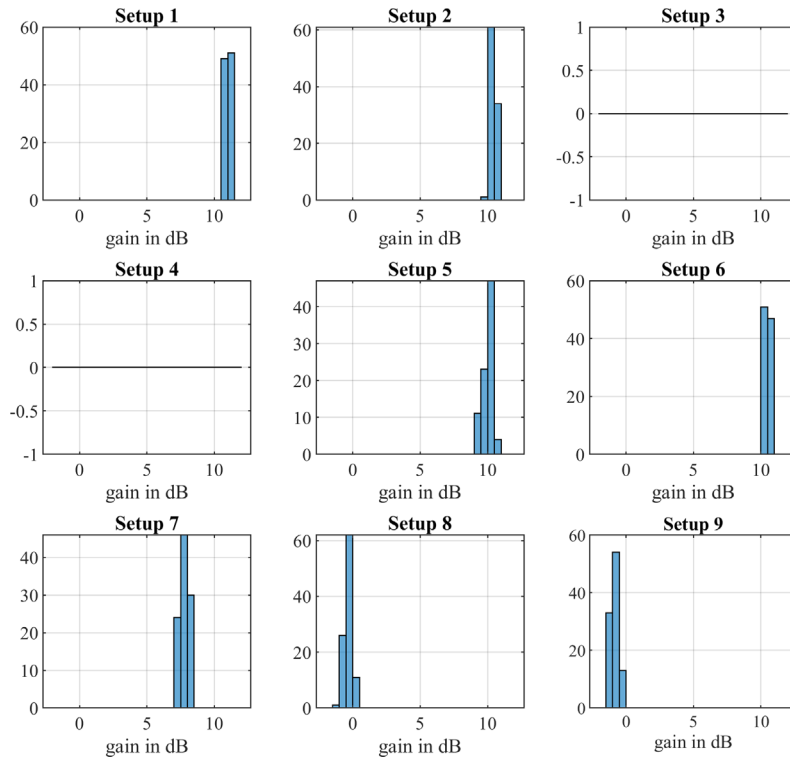


Figure 4.38. statistical analysis of the peak power gain for different matching networks using a center frequency of 1.5 GHz and a 500 MHz pulse as described in Figure 4.35.

Figure 4.39 and Figure 4.40 map the fidelity factor and power gain to the corresponding reflection coefficients using Smith Charts. Each line corresponds to the reflection coefficient at the reference plane of the DUT over the 500 MHz band accommodating the signal. The center frequency of 1.5 GHz is indicated with a magenta colored cross and a number showing the used matching network.

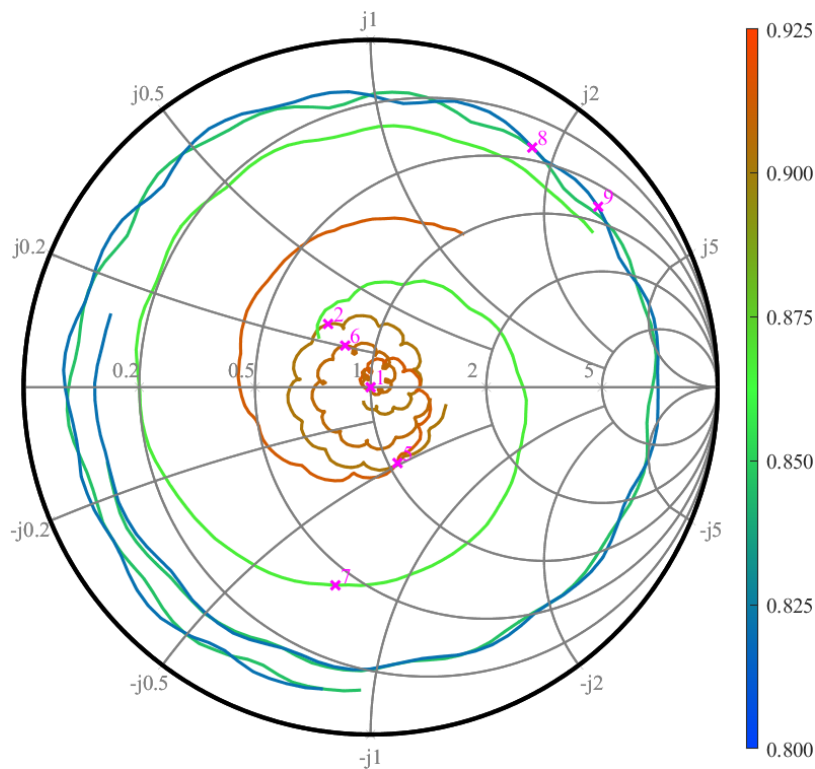


Figure 4.39. Smith Chart showing the fidelity factor for different matching networks using pulsed signals. Each line represents the impedances seen by the DUT in the used frequency band. The magenta colored crosses indicate the center frequency of 1.5 GHz and their caption shows the used matching network.

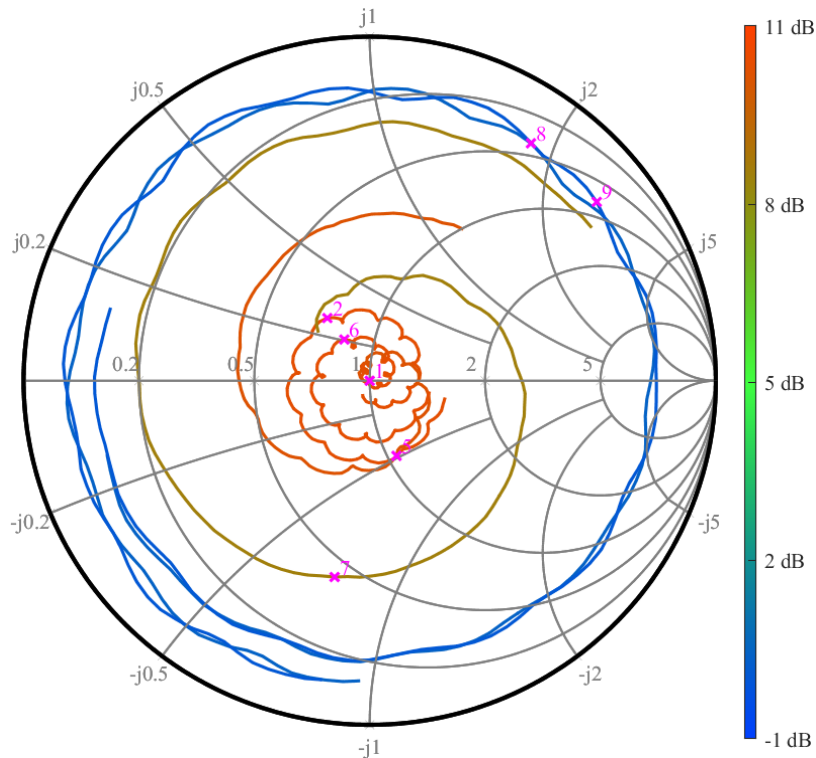


Figure 4.40. Smith Chart showing the RMS power gain in dB for different matching networks using pulsed signals. Each line represents the impedances seen by the DUT in the used frequency band. The magenta colored crosses indicate the center frequency of 1.5 GHz and their caption shows the used matching network.

Figure 4.41 shows the gain measured using a 1.5 GHz CW signal. As only a single frequency is being analyzed a contour plot using linear interpolation can be used to provide information about the DUTs behavior. Magenta colored crosses and numbers indicating the used matching network represent the points, which were actually measured.

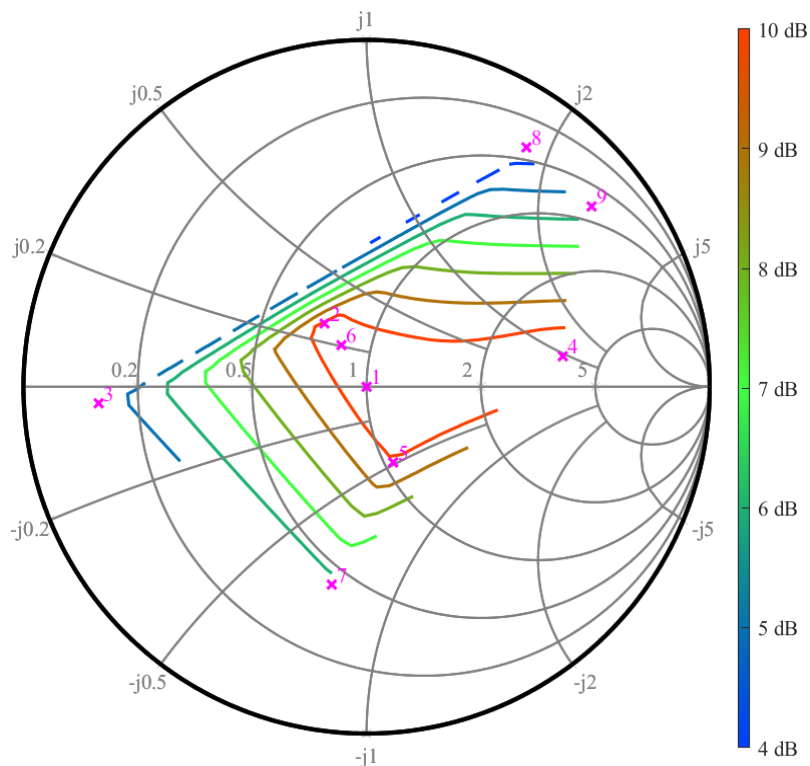


Figure 4.41. Smith Chart showing the measured power gain in dB using a 1.5 GHz CW signal. Linear interpolation was used to calculate the points of the contour plot. No extrapolation was applied.

b. Discussion of Measurement Results

By looking at Figure 4.35 it can be observed that the reference waveform (red) already differs quite strongly from the digital waveform passed to the AWG (green). This is not because of the AWG, but because of the frequency response of the signal generator used to mix the baseband signal up to 1.5 GHz. For my investigations, this does not pose a problem as I capture the input signal and output signal of the DUT using a power splitter. The histogram plots show the stability of the measurement results between pulses. In my case, it was important to analyze this behavior as the baseband signal generated by the AWG is not synchronous to the local oscillator signal in the signal generator which is used to generate, the bandpass signal. This results in different phase relations between envelope and carrier signal for each pulse, even if both devices are supplied with the same 10 MHz reference. Fortunately, the histograms in Figure 4.36, Figure 4.37 and Figure 4.38 reveal that this has no major influence on the load-pull behavior of the setup. Furthermore, they show that the RMS power gain and peak power gain of the DUT are nearly identical. This is because the amplifier operates in its linear range as the input signal is about -7 dB below the $P_{1dB_{input}}$ in peak power. It is important to use the peak power because the used signal has a high peak-to-average power ratio of about 18 dB. The results for peak and RMS power are nearly identical. Hence, in the Smith chart I only presented the results for the RMS power gain.

Figure 4.39 connects the fidelity factor averaged over all realizations and load reflection coefficients for each frequency using a Smith chart. As the reflection coefficients over the whole 500 MHz frequency band vary quite a lot for a single matching network, it is hardly possible to derive any general meaning. The only thing that can be concluded is that the fidelity factor decreases with lower reflection coefficients. The only exception is presented by setup 5 which results in a fidelity factor as high as for the direct connection to the oscilloscope in setup 1. Regarding the gain, higher load reflection coefficients result in a lower gain for all setups as visualized in Figure 4.40. Comparing these results to the measurements using a CW signal shown in Figure 4.41 the only thing I can say is that the DUT seems to be well matched to 50 Ω .

To conclude this discussion, I have to admit that the acquired measurement results presented in this sub-section are far from satisfying. The presented approach to use matching networks with discrete components which are changed between measurements does not allow a fine tuning to specific impedance points nor a good coverage of the Smith chart. Furthermore, it is nearly impossible to design many matching networks featuring the desired frequency responses over such a wide bandwidth. Due to these restrictions, I did not further investigate this approach to perform wideband load-pull measurements and I also discourage others to use this method. Instead, a more promising method is presented in the next section.

4.3.2 The Two-Pulse Method

Knowing that a more flexible approach to wideband load-pull is needed I reconsidered the initial problem. In a final application, a device connected to a load with some transmission line of unknown length. This transmission line will usually be shorter than measurement setups based on off-the-shelf lab components. These components are typically based on SMA connections and slide-screw tuners, resulting in the problem that the setup of the final implementation cannot be reproduced directly under laboratory conditions. However, the actual requirement for load-pull is to change the reflection coefficient seen by the DUT. As summarized in Section 2.3 the reflection coefficient is defined as the ratio of the reflected wave to the incident wave at the reference plane of the DUT. To satisfy this condition the reflected wave does not need to be generated by the incident wave, as it is also used in some active load pull systems. To put it simply, in the case of UWB-IR the reflected wave can be generated by a different pulse than the incident wave currently generated by the DUT. For such an

extension of the reflection coefficient a high correlation between the pulses from the RF carrier and the envelope signal must be assumed. If a DUT is setup to periodically transmit identical pulses the reflection of a previous pulse can be used to adjust the reflection coefficient the DUT sees after the first reflection arrives at the DUT. Luckily, UWB-IR uses periodic pulse sequences to generate the preamble of a frame as described in Section 2.1. To utilize this I came up with the measurement setup presented in Figure 4.42 and Figure 4.43. As DUT I used the same DW1000® UWB-IR chip and PCB as in Section 4.1. At the output ports, I connected a 180° hybrid to allow easy mixed-mode load-pull measurements as they were discussed in Section 4.2. For the investigations in this section, the screws of the probe for the common mode load tuner were fully retracted resulting in a low common mode reflection coefficient. At the Δ port of the 180° hybrid an SMA cable with defined length was used to connect external directional couplers followed by the tuner. The reason I used external directional couplers in this setup is that they provide a much better directivity of >21 dB, compared to the wiggly line microstrip couplers on the PCB presented in Section 4.1.1, which only feature a directivity of >15 dB. A de-embedding as presented in Section 4.1 was applied to calculate the signals at the reference plane of the chip.

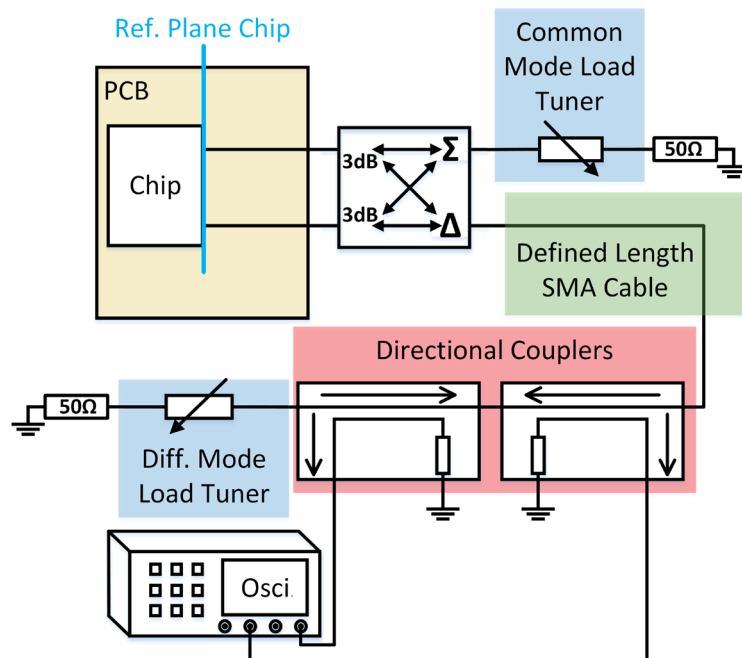


Figure 4.42. Block diagram of the measurement setup used to perform the two-pulse load-pull measurements presented in this section.

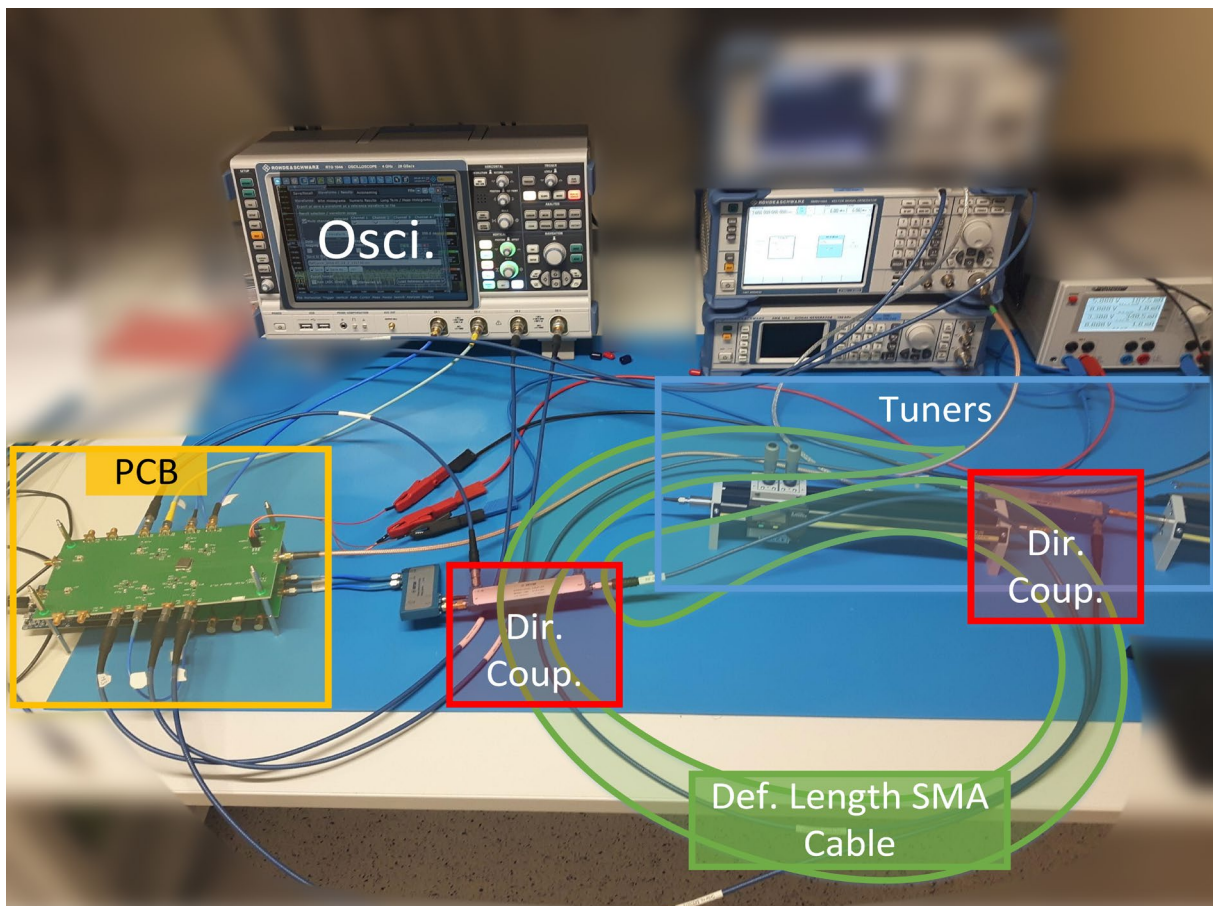


Figure 4.43. Photo of the real measurement setup used to perform the two-pulse load-pull measurements presented in this section. The colors used to indicate the different parts of the setup match the colors used for the block diagram in Figure 4.42. In addition to the component shown in the block diagram, a PCB with mixers (placed over the PCB with the DUT) was used to convert the signal to a center frequency of 2 GHz, which can be captured using a R&S RTO 1044 oscilloscope.

a. Measurement Results

Figure 4.44 and Figure 4.45 show the differential mode forward traveling and reflected waves at the reference plane of the chip for different length SMA connection cables. The differential mode tuner's slide position used for these plots was set to 0 mm, which corresponds to the shortest possible distance to the DUT. The distance between probe and airline was set to 0.5 mm which results in a relatively high reflection coefficient at the tuner.

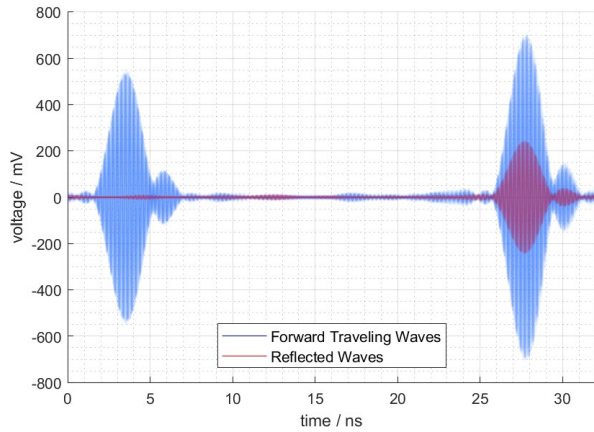


Figure 4.44. Plot showing the forward traveling (coming from the chip) and reflected (coming from the load) differential mode waves at the reference plane of the chip. The plot is generated using 100 realizations which are overlapped.

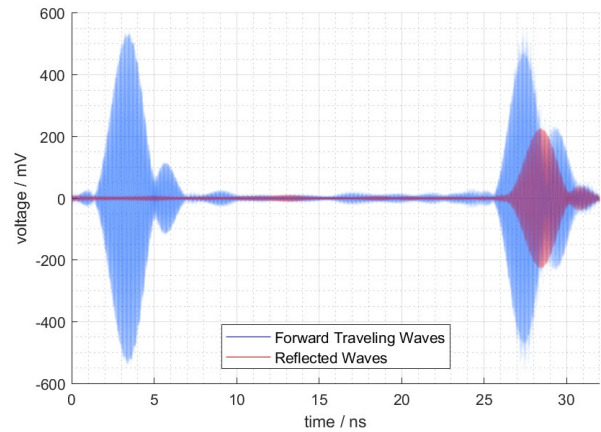


Figure 4.45. Plot showing the forward traveling and reflected differential mode waves at the reference plane of the chip using a longer SMA cable as connection between DUT and tuners. The plot is generated using 100 realizations which are overlapped.

Figure 4.46 and Figure 4.47 show different RMS power levels averaged over 100 measurements for different tuner slide positions using the same probe to airline distance of 0.5 mm as before. The RMS power is calculated over a time of 8 ns for each pulse. The blue lines indicates the power of the incident or forward traveling wave, the red lines the power of the reflected wave and the green lines are the difference between the incident and reflected power resulting in the power dissipated in the load. Because the results are calculated using 100 measurements also the standard deviations are plotted using dashed lines. The averaged RMS output power per pulse varies in a range from 300 mW to 800 mW depending on the tuner setting.

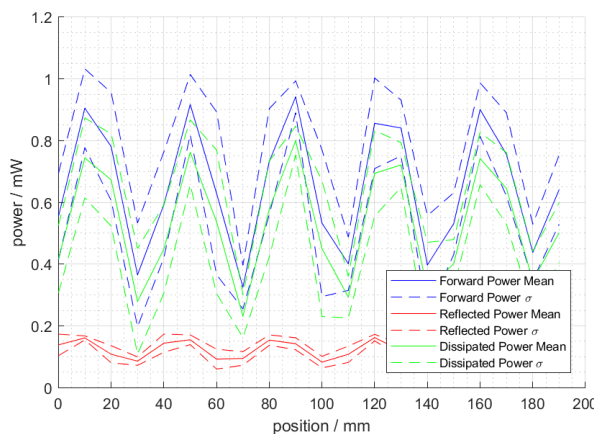


Figure 4.46. Plot of power levels over different tuner slide positions. The position of 0 mm corresponds to the result shown in Figure 4.44. The plot is generated using the mean value of 100 realizations.

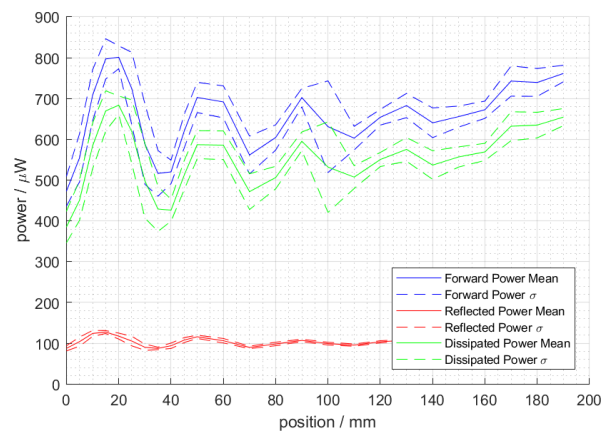


Figure 4.47. Plot of power levels over different tuner slide positions using a longer SMA cable as connection between the DUT and tuners. The position of 0 mm corresponds to the result shown in Figure 4.45. The plot is generated using the mean value of 100 realizations.

Figure 4.48 shows the results of the load pull measurements mapped to the reflection coefficients at the reference plane of the DUT and the center frequency of 4 GHz.

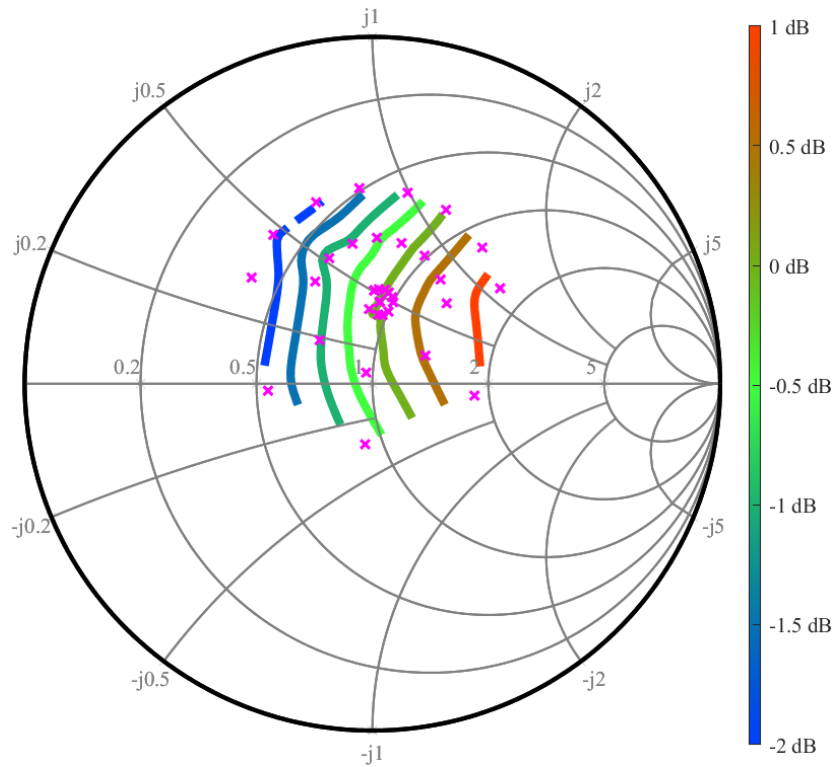


Figure 4.48. Smith chart showing wideband load-pull results mapped to the differential mode impedances seen by the DUT a center frequency of 4 GHz. The chart is normalized to 100Ω . The colors of the contour plot show the gain in output power relative to the output power measured without load-tuning. The magenta colored crosses indicate the measured points while the contour plot was generated using linear interpolation between these points and no extrapolation. The plot is generated using the mean value of 100 realizations.

b. Discussion of Measurement Results

In this sub-section I showed that by using a previous pulse as reflected signal, loads at arbitrarily short distances can be simulated in the lab. By using a shorter SMA cable, as connection one could even simulate negative distances between DUT and load, which of course cannot occur in a real application. For this tuning approach, the length of the connection between DUT and tuner needs to be chosen depending on the pulse repetition frequency. By looking at Figure 4.44 and Figure 4.45 it becomes obvious that not the phase but the electrical distance between DUT and load is what needs to resemble the final application. The reason why looking at the phase works in the special case of a CW signal is that the phase relation repeats periodically for increasing distances. Figure 4.49 shows the relative phase error between different frequency components if the load is placed at different distances of $k_0 \cdot \lambda_0$ from the DUT, where λ_0 is the wavelength at the center frequency on the transmission line. Looking at this figure, it becomes obvious that there are two methods to achieve the same relative phase error. A narrowband signal placed farther away from the DUT results in the same relative phase error as a wideband signal placed close to the DUT.

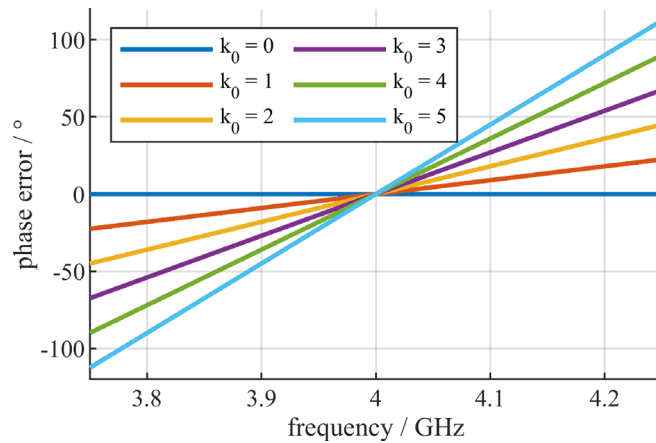


Figure 4.49. Visualization of the relative phase error of different frequency components in comparison to the carrier frequency. The different k_0 values indicate the distance in $k_0 \cdot \lambda_0$ between DUT and load.

Continuing with Figure 4.46 and Figure 4.47 it can be observed that the less the pulses overlap, the less the impact of the tuner setting can be noticed. If the distance between tuner probe and DUT would be further increased the reflected and incident signals would not overlap at all, resulting in a forced match to the differential mode impedance of the transmission line of 100Ω . That this is not the optimum case for the DW1000[®] chip used as a DUT is shown in Figure 4.48. It also shows that the tuning range of this setup is very limited. This is mainly because of the insertion loss caused by the unused directional couplers on the PCB of the DUT (see Figure 4.8), the insertion loss of the 180° hybrid and the two additional directional couplers placed between the tuner and DUT. Nevertheless, the presented setup was able to show that load-pull measurements with pulsed signals can be performed. To significantly increase the tuning range of the setup the following steps can be taken: At first, the DUT needs to be placed on a PCB without the aforementioned directional couplers and with short lines to decrease the insertion loss. Second, the measurement setup shown in Figure 4.26 should be used. In combination with a pre-characterization of the tuners, and of course all other components of the measurement setup, a de-embedding can be performed to acquire the same results as presented in this section. After these steps have been conducted it should be possible to achieve a tuning range similar to what I presented in Section 4.2.4, only limited by the insertion loss of the PCB the DUT is located on, the SMA connections between the PCB and tuners and the tuning range of the tuners.

4.4 Conclusion for Device Characterization

In Section 4.1 a de-embedding approach for multiport networks like they are used for differential load pull was presented. The de-embedding for the presented setup achieves a residual amplitude error below 5 %, and a timing mismatch below 10 ps. The amplitude error is most likely caused by the noise enhancement introduced in the de-embedding process.

Conducting mixed-mode load-pull measurements with a 180° hybrid allows to easily tune differential and common mode load independently of each other, if the magnitude and phase imbalance of the hybrid are in an acceptable range. What an “acceptable range” is needs to be defined for each application. To help the reader with this task a simple formula was derived to estimate the impact of a 180° hybrid’s imperfections.

Simply connecting tuners directly to the device under test decreases the insertion loss, but forces equal differential and common mode loads. The method proposed by us in [80] does not need a 180° hybrid, but still allows unequal differential and common mode loads in exchange for ease of use and limited combinations of differential and common mode reflection coefficients. This method also allows to set

reflection coefficients of higher magnitude compared to a setup with tuners connected directly to the DUT. An increase of $|\Gamma_{dd,max}|$ from 0.85 to 0.94 was possible using the proposed setup with the same tuners. An increased tuning range can be achieved with the same tuners, by adding an adjustable attenuator and phase shifter in the transmission path between the tuners.

As always, I cannot provide a single solution fulfilling all requirements. The setup with tuners directly connected to the DUT and matched at the other port has the lowest hardware effort, features higher tuning range than a system using 180° hybrids, but forces equal differential and common mode reflection coefficients. Setups with 180° hybrids allow easy and independent tuning of the individual reflection coefficients, but the hybrid's insertion loss reduces the maximum achievable reflection coefficients. The proposed setup with tuners directly connected to the DUT and also connected to each other via an adjustable attenuator and phase shifter allows even higher reflection coefficients than the setup with directly connected tuners, and the possibility of having different differential and common mode reflection coefficients. But the combinations of different reflection coefficients are more limited compared to the setup using a 180° hybrid, and the hardware effort is the highest of all discussed setups. In the end, the reader needs to decide which setup is best suited for each individual application.

A passive load-pull system using a 180° hybrid was used to perform measurements for a real device. This demonstrates how simple a passive real mixed-mode load-pull setup could look like, but also the limitations regarding tuning range. The measurements showed that the device under test is not perfectly matched to $100\ \Omega$ differential and an increase in output power of up to 5.13 dB is possible with additional matching.

In Section 4.3 I discussed the problems which arise for load-pull measurements using pulsed signals as they are used for UWB-IR applications. Electrically large measurement setups as they are typically used in the laboratory cannot be used directly to perform load-pull measurements with pulsed signals. In some cases, the DUT may stop pulse generation before the reflection coming from the load arrives at the port of the DUT. Therefore, the DUT only sees the characteristic impedance of the transmission line while generating the pulse, rendering any change of the load impedance ineffective. I presented an approach where I tried to build an electrically short wideband load-pull system using matching networks with discrete components. This approach was all but satisfying as the frequency responses of the matching networks made it nearly impossible to generate meaningful results. A second more promising looking method using periodic transmission of UWB pulses and connections matched to the pulse repetition frequency was presented in Section 4.3.2. By applying the methods to increase the tuning range of passive load-pull setups presented in Section 4.2 this setup could be used to perform passive wideband load-pull measurements for UWB-IR devices with relatively low hardware effort.

5 Final Conclusion

In this section I provide an overview of the findings presented in this thesis followed by an outlook for the future of UWB technology. Detailed conclusions for each of the major topics can be found in Section 3.6 for system level investigations and Section 4.4 for device characterization.

5.1 Findings

With the help of physical layer system simulations, I showed that the impulse response of an antenna has a non-negligible impact on the ranging accuracy of an UWB system. For the presented antennas, the ranging error was about ± 5 cm. I also presented that the peak power of an UWB signal should be used instead of the RMS power, because increasing the power of side lobes does not increase the dynamic of the cross-correlation function, which is especially important for leading edge detection algorithms. Interference simulations showed that by choosing different frame formats the probability of a collision of UWB frames can be traded for robustness in case of a collision. In the future protocol designers can use this information to find the sweet spot for each application. In the second part of this thesis, I presented a new method for mixed-mode load-pull measurements which is able to increase the tuning range of passive load-pull setups. Furthermore, a method for wideband load-pull measurements using pulsed signals was proposed, which allows to characterize an UWB device under real operating conditions instead of using continuous wave signals.

5.2 The Future of UWB

UWB has been around for a long time, but only recently the interest of the industry is really driving new development of this promising technology. One sign of this increased effort is the formation of the UWB Alliance in 2018, which was formed to develop UWB technology and the IEEE 802.15.4z standard. Among the founding members of this alliance are companies like Apple, Hyundai, Kia, Zebra, Decawave, Alteros, Novelda and Ubisense. It is likely that other smartphone manufacturers will follow Apple and build UWB into their devices, leading to lower production cost and better availability of infrastructure. Initially mostly applications that need precise and robust localization either for security or safety reasons will rely on UWB. By using sensor fusion of GNSS and IPS accurate position estimates without disruptions due to multipath conditions in urban environments could be realized, resulting in an improved user experience for all applications relying on location data. This is valid not only for smartphones but also for the automotive industry where UWB will be essential for Keyless-Go systems. Also in the automotive industry new use cases will appear once UWB is commonly applied, as it can be used not only to locate a key, but also smartphones or even other cars equipped with UWB.

Another related topic is the development of UWB radars, which can be combined with UWB communication and ranging. Typically, the requirements for a communication system are different to the requirements of a radar system, but with the increased dynamic range of modern UWB chips and the similarity of the signal shape between conventional UWB and radar systems, building hybrid systems becomes possible. Although the resulting hybrid system will not have the performance of a dedicated radar, short range ranging and detection of objects without an UWB node is possible. Possible applications are the contactless measurement of breath and heart rates of a driver in a car or intrusion detection [84].

In addition to ranging, UWB can also be used to transmit large amounts of data between devices over short distances. With the planned completion of the IEEE 802.15.4z standard in 2022-2024 UWB can be used as a wireless high definition video transmission technology.

Still there is a lot of development needed to refine UWB to the state other technologies like WiFi® or Bluetooth® have already reached. Not only the UWB technology itself can be improved, also sophisticated test environments for UWB systems need to be developed. Due to the technical characteristics and use as ranging technology, such test environments need to be different to traditional communication system test stations. Performing tests using wired connections only will not be sufficient to fully characterize an UWB System, as external circuitry, antennas, housing and the transmission channel may have a non-negligible impact on ranging accuracy. The first hurdle for building test environments being the definition of standardized test cases, which cover a wide range of real-world scenarios, but can still be performed with reasonable effort. With the increasing number of UWB devices proper interference management will become a hot topic in the future. Especially for use cases in harsh multipath environments with many users, interference management is key to success. An example for such an applications is the usage of UWB enabled smartphones as subway tickets. This would allow users to pass through turnstiles without any active interaction, made possible by accurate localization. But simultaneous accurate localization of hundreds of people in the same underground environment is a demanding task, even for UWB technology featuring best in class multipath resolving capabilities.

The foundation is set, now it is up to us engineers to develop this technology to a market-ready state, deliver the best possible user experience, and hopefully change the world for the better.

References

- [1] G. Giancola and M.-G. Di Benedetto, "A novel approach for estimating multi-user interference in impulse radio UWB networks: The pulse collision model," in *Signal Processing - Signal processing in UWB communications, Vol. 86, Iss. 9*, 2006, pp. 2185-2197.
- [2] G. Durisi and G. Romano, "On the validity of Gaussian approximation to characterize the multiuser capacity of UWB TH PPM," in *Conference: Ultra Wideband Systems and Technologies*, Baltimore, MD, USA, USA, 2002.
- [3] J. Rousselot and J.-D. Decotignie, "A High-Precision Ultra Wideband Impulse Radio Physical Layer Model for Network Simulation," in *2nd International Conference on Simulation Tools and Techniques*, Brussels, Belgium, 2009 .
- [4] A. Lecointre, A. Berthe, D. Dragomirescu, J. Turbert and R. Plana, "Performance evaluation of Impulse Radio Ultra Wide band Wireless Sensor Networks," in *MILCOM - IEEE Military Communications Conference*, Boston, MA, USA, 2009 .
- [5] K. Nakanishi, V. Niemelä, M. Hämäläinen, J. Linatti and S. Hara, "On IEEE 802.15.6 IR-UWB ED receiver performance in the presence of multiuser interference," in *9th International Symposium on Medical Information and Communication Technology (ISMICT)*, Kamakura, Japan, 2015.
- [6] G. Giancola and M.-G. Di Benedetto, "a collision-based model for multi user interference in impulse radio UWB networks," in *2005 IEEE International Symposium on Circuits and Systems*, Kobe, Japan, 2005.
- [7] R. Merz and J.-Y. Le Boudec, "Conditional bit error rate for an impulse radio UWB channel with interfering users," in *IEEE International Conference on Ultra-Wideband*, Zurich, Switzerland, 2005.
- [8] R. Scholtz, "Multiple access with time-hopping impulse modulation," in *Proceedings of MILCOM '93 - IEEE Military Communications Conference*, Boston, MA, USA, USA, 1993.
- [9] M. Z. Win and R. Scholtz, "Ultra-wide bandwidth time-hopping spread-spectrum impulse radio for wireless multiple-access communications," in *IEEE Transactions on Communications, Vol. 48, Iss. 4*, 2000, pp. 679 - 689.
- [10] D. Köther and J. Berben, "Load-Pull Measurements of Differential Amplifiers," in *67th ARFTG Conference*, San Francisco, CA, USA, 2006.
- [11] W. Liu and C. Tsironis, "Load Pull Characterization System For Differential Devices," in *62nd ARFTG Microwave Measurements*, Boulder, CO, USA, 2003.
- [12] R. Mahmoudi, M. Spirito, P. Valk and J. Tauritz, "A Novel Load and Source Tuning System for Balanced and Unbalanced WCDMA Power Amplifiers," in *54th ARFTG Conference Digest*, Atlanta, GA, USA, 1999.
- [13] M. Spirito, M. Van der Heijden, M. De Kok and L. De Vreede, "A Calibration Procedure for On-Wafer Differential Load-Pull Measurements," in *61st ARFTG Conference Digest*, Philadelphia, PA, USA, 2003.

- [14] V. Teppati, A. Ferrero, M. Garelli and S. Bonino, "A Comprehensive Mixed-Mode Time-Domain Load- and Source-Pull Measurement System," *IEEE Transaction on Instrumentation and Measurement*, vol. 59, no. 3, pp. 616-622, 2010.
- [15] A. Ferrero and V. Teppati, "A Novel Active Differential/Common-Mode Load for True Mixed-Mode Load-Pull Systems," in *IEEE MTT-S International Microwave Symposium Digest*, Philadelphia, PA, USA, 2006.
- [16] S. Mathias, "Microwave Journal," 29 February 2012. [Online]. Available: <http://www.microwavejournal.com/blogs/10-tek-talk/post/17056-load-pull-system-pros-and-cons>.
- [17] L. R. Rabiner, R. W. Schafer and C. M. Rader, "The chirp z-transform algorithm and its application," *The Bell System Technical Journal*, vol. 48, no. 5, pp. 1249-1292, 1969.
- [18] W. Yiding, W. Yirong and H. Jun, "Application of inverse chirp-z transform in wideband radar," in *International Geoscience and Remote Sensing Symposium (IGARSS 2001)*, Sydney, Australia, 2001.
- [19] S. Heuel, "www.localino.net," May 2018. [Online]. [Accessed 2019].
- [20] L. Mearian, "Computerworld," 31 12 2019. [Online]. Available: <https://www.computerworld.com/article/3490037/ultra-wideband-explained-and-why-its-in-the-iphone-11.html>. [Accessed 8 June 2020].
- [21] Geekspin, "Geekspin," January 2020. [Online]. Available: <https://geekspin.co/the-smartphone-is-about-to-replace-your-drivers-license-and-passport/>. [Accessed 8 June 2020].
- [22] IEEE Standards Association, "IEEE802.15.4-2015 (Revision of IEEE Std 802.15.4-2011)," [Online]. Available: <http://standards.ieee.org/>.
- [23] Q. Wangye, H. Luying, G. Lvjian and L. Zhangjin, "A UWB Ranging Algorithm Based on Almost Perfect Autocorrelation Sequences," in *6th International Conference on ITS Telecommunications*, 2006.
- [24] E. Karapistoli, F.-N. Pavlidou, I. Gragopoulos and I. Tsetsinas, "An Overview of the IEEE 802.15.4a Standard," *IEEE Communication Magazine*, vol. 48, no. 1, pp. 47-53, 2010.
- [25] C. Hoene and J. Willmann, "Four-way TOA and Software-Based Trilateration of IEEE 802.11 Devices," in *IEEE 19th International Symposium on Personal, Indoor and Mobile Radio Communications*, Cannes, France, 2008.
- [26] D. Dardari, A. Conti, U. Ferner, A. Giorgetti and M. Z. Win, "Ranging With Ultrawide Bandwidth Signals in Multipath Environments," *Proceedings of the IEEE*, vol. 97, no. 2, pp. 404-426, 2009.
- [27] Decawave, "APS013: The implementation of two-way ranging with the DW1000," 2015. [Online]. Available: https://www.decawave.com/wp-content/uploads/2018/10/APS013_The-Implementation-of-Two-Way-Ranging-with-the-DW1000_v2.3.pdf. [Accessed 15 June 2020].
- [28] S. Gezici, Z. Tian, G. B. Giannakis, H. Kobayashi, A. F. Molisch, H. V. Poor and Z. Sahinoglu, "Localization via Ultra-Wideband Radios," *IEEE Signal Processing Magazine*, vol. 22, no. 4, pp. 70-84, 2005.
- [29] A. M. Orndorff, *Transceiver Design for Ultra-Wideband Communications*, Blacksburg, VA: Virginia Polytechnic Institute and State University, 2004.

- [30] I. Dotlic and R. Miura, "IEEE 802.15.4a-Based Impulse Radio Ultra-Wideband System with Joint Channel Equalization and Decoding," in *IEEE Conference on Ultra-WideBand (ICUWB)*, Paris, 2014.
- [31] E. Leitinger, P. Meissner, C. Rüdissler, G. Dumphart and K. Witrissal, "Evaluation of Position-Related Information in Multipath Components for Indoor Positioning," *IEEE Journal on Selected Areas in Communications*, vol. 33, no. 11, pp. 2313-2328, 2015.
- [32] S. Hinteregger, E. Leitinger, P. Meissner, J. Kulmer and K. Witrissal, "Bandwidth Dependence of the Ranging Error Variance in Dense Multipath," in *European Signal Processing Conference (EUSIPCO)*, Budapest, Hungary, 2016.
- [33] T. Wilding, S. Grebien, U. Mühlmann and K. Witrissal, "Accuracy Bounds for Array-Based Positioning in Dense Multipath Channels," *Sensors*, vol. 18, no. 12, p. 4249, 2018.
- [34] C. Gentile and A. Kik, "A Comprehensive Evaluation of Indoor Ranging Using Ultra-Wideband Technology," *EURASIP Journal on Wireless Communications and Networking*, vol. 2007, no. 1, pp. 1-10, 2007.
- [35] D. Veit, E. Leitgeb, F. Teschl and T. Gigl, "UWB channel measurements for short range radar applications," in *25th International Conference on Software, Telecommunications and Computer Networks (SoftCOM)*, Croatia, Split, 2017.
- [36] W. Sörgel and W. Wiesbeck, "Influence of the Antennas on the Ultra-Wideband Transmission," *EURASIP Journal on Applied Signal Processing*, vol. 3, pp. 296-305, 2005.
- [37] J. A. Dobrowolski, *Microwave Network Design Using the Scattering Matrix*, Warsaw: Artech House, 2010.
- [38] D. E. Bockelman and W. R. Eisenstadt, "Combined Differential and Common Mode Scattering Parameters: Theory and Simulation," *IEEE Trans. Microwave Theory and Techniques*, vol. 43, no. 7, pp. 1530-1539, 1997.
- [39] D. Veit, M. Gadringer and E. Leitgeb, "A Simulation Environment for UWB Hardware Development and Protocol Design," in *The 15th International Conference on Telecommunications*, Graz, Austria, 2019.
- [40] L. O. Chua and A.-C. Deng, "Canonical Piecewise-Linear Modeling," in *IEEE Transactions on Circuits and Systems*, Vol. 33, Iss. 5, 1986, pp. 511 - 525.
- [41] K. M. Gharaibeh, "Behavioral modeling of nonlinear power amplifiers using threshold decomposition-based piece wise linear approximation," in *IEEE Radio and Wireless Symposium*, Orlando, FL, USA, 2008.
- [42] M. Lázaro, I. Santamaría, C. Pantaleón, A. Mediavilla Sánchez, A. T. Puente and T. Fernández, "Smoothing the Canonical Piecewise-Linear Model: An Efficient and Derivable Large-Signal Model for MESFET/HEMT Transistors," in *IEEE TRANSACTIONS ON CIRCUITS AND SYSTEMS*, Vol. 48, Iss. 2, 2001, pp. 184 - 192.
- [43] J. Karedal, S. Wyne, P. Almers, F. Tufvesson and A. F. Molisch, "A Measurement-Based Statistical Model for Industrial Ultra-Wideband Channels," *IEEE Transactions on Wireless Communications*, vol. 6, no. 8, pp. 3028-3037, 2007.
- [44] A. F. Molisch, K. Balakrishnan, D. Cassioli, C.-C. Chong, S. Emami, A. Fort, J. Karedal, J. Kunisch, H. Schantz, U. Schuster and K. Siwiak, "IEEE 802.15.4a channel model - final reportt, Tech. Rep. Document IEEE 802.15-04-0662-02-004a," 2005.

- [45] A. A. M. Saleh and R. A. Valenzuela, "A Statistical Model for Indoor Multipath Propagation," *IEEE Journal on Selected Areas in Communications*, vol. 5, no. 2, pp. 128-137, 1987.
- [46] M. Kortmann and A. Martin, "mksqlite," Sourceforge, 4 26 2017. [Online]. Available: <http://mksqlite.sourceforge.net/>. [Accessed 2019].
- [47] D. Veit, M. Gadringer and E. Leitgeb, "Impact of UWB Antennas on Ranging Accuracy," in *European Conference on Antennas and Propagation (EuCAP)*, Copenhagen, Denmark, 2020.
- [48] W. Kong, Y. Zhu and G. Wang, "Effects of pulse distortion in UWB radiation on UWB impulse communications," in *International Conference on Wireless Communications, Networking and Mobile Computing*, Wuhan, China, 2005.
- [49] V. Sipal, B. Allen and D. Edwards, "Impact of Antennas on Practical UWB Signals," in *7th European Conference on Antennas and Propagation (EuCAP)*, Gothenburg, Sweden, 2013.
- [50] E. Pancera, T. Zwick and W. Wiesbeck, "Spherical Fidelity Patterns of UWB Antennas," *IEEE Transactions on Antennas and Propagation*, vol. 59, no. 6, pp. 2111-2119, 2011.
- [51] J. S. McLean, H. Foltz and R. Sutton, "Pattern Descriptors for UWB Antennas," *IEEE Transactions on Antennas and Propagation*, vol. 53, no. 1, pp. 553-559, 2005.
- [52] M. G. Nabi Alsath and M. Kanagasabai, "Compact UWB Monopole Antenna for Automotive Communications," *IEEE Transactions on Antennas and Propagation*, vol. 63, no. 9, pp. 4204-4208, 2015.
- [53] M. Mokhtaari and J. Bornemann, "Directional Ultra-Wideband Antennas in Planar Technologies," in *38th European Microwave Conference*, Amsterdam, Netherlands, 2008.
- [54] G. S. Reddy, S. Kharche and J. Mukherjee, "Ultra Wideband Printed Monopole Antenna with Curve shaped Extended Asymmetric CPW Ground Plane for Stable Unidirectional Radiation Pattern," in *IEEE Antennas and Propagation Society International Symposium (APSURSI)*, Memphis, USA, 2014.
- [55] IEEE Standards Association, IEEE Standard for Local and metropolitan area networks - Part 15.4: Low-Rate Wireless Personal Area Networks (LR-WPANS), New York, USA: IEEE, 2011.
- [56] D. Lamensdorf and L. Susman, "Baseband-pulse-antenna techniques," *IEEE Antennas and Propagation Magazine*, vol. 36, no. 1, pp. 20-30, 1994.
- [57] D. Veit, M. Gadringer and E. Leitgeb, "On UWB Pulse Distortion Caused by Amplifiers and Mismatched Antennas," in *6th annual IEEE International Conference on Microwaves for Intelligent Mobility*, Linz, 2020.
- [58] IEEE, IEEE Std. 802.15.4-2015, Standard for Low-Rate Wireless Networks, 2015.
- [59] FCC, "Commission's Rules Regarding Ultra-Wideband Transmission Systems (FCC 02-48)," Federal Communications Commission (FCC), Washington, D.C., 2002.
- [60] M. S. Mohammadi, Q. Zhang, E. Dutkiew and X. Huang, "Optimal Frame Length to Maximize Energy Efficiency in IEEE 802.15.6 UWB Body Area Networks," *IEEE Wireless Communications Letters*, vol. 3, no. 4, pp. 397 - 400, 2014.
- [61] DecaWave, "Characterisation of the NLOS Performance," [Online]. Available: <https://www.decawave.com/sites/default/files/resources/research.pdf>. [Accessed 8 March 2019].

- [62] Maury Microwave, "A Beginner's Guide To All Things Load Pull," 3 2015. [Online]. Available: <https://www.maurymw.com/pdf/datasheets/5A-062.pdf>. [Accessed 12 3 2018].
- [63] Agilent, "Agilent AN 154 - S-Parameter Design," Agilent Technologies, 2006.
- [64] Anritsu, "Application Note - Embedding/De-embedding," Anritsu, 2002.
- [65] H. Arthaber, M. L. Mayer, A. Gafni, M. Gadringer and G. Magerl, "A Time-Domain Large-Signal Measurement Setup," *International Journal of RF and Microwave Computer-Aided Engineering*, vol. 15, no. 1, pp. 3-12, 2005.
- [66] Keysight Technologies, "Power Amplifier Design and Load Pull Measurements in Practice," 2013. [Online]. Available: https://www.keysight.com/upload/cmc_upload/All/CollectingMeasurementData.pdf. [Accessed 12 3 2018].
- [67] D. Veit, M. Gadringer and E. Leitgeb, "A Compact Ultra-Wideband Load-Pull Measurement System," in *2018 International Conference on Broadband Communications for Next Generation Networks and Multimedia Applications (CoBCom)*, Graz, Austria, 2018.
- [68] DecaWave, "DW1000 Datasheet," 2015. [Online]. Available: <https://www.decawave.com/sites/default/files/resources/dw1000-datasheet-v2.09.pdf>. [Accessed 23 2 2018].
- [69] IEEE Standards Association, "IEEE802.15.4-2011 (Revision of IEEE Std 802.15.4-2006)," [Online]. Available: <http://standards.ieee.org/>.
- [70] A. Podell, "A High Directivity Microstrip Coupler Technique," in *Microwave Symposium, G-MTT 1970 International*, 1970.
- [71] S. Uysal and H. Aghvami, "Synthesis, Design, and Construction of Ultra-Wide-Band Nonuniform Quadrature Directional Couplers in Inhomogeneous Media," *IEEE Transactions on Microwave Theory and Techniques*, vol. 37, no. 6, pp. 969-976, 1989.
- [72] J.-L. Chen, S.-F. Chang and C.-T. Wu, "A High-Directivity Microstrip Directional Coupler With Feedback Compensation," in *Microwave Symposium*, Seattle, 2002.
- [73] R. Phromlounsri, V. Chamnanphrai and M. Chongcheawchamnan, "Design high-directivity parallel-coupled lines using quadrupled inductive-compensated technique," in *APMC 2006*, Yokohama, 2006.
- [74] A. Golaszewski and A. Abramowicz, "High Directivity Microstrip Couplers," in *Microwave, Radar and Wireless Communications Conference*, Krakow, 2016.
- [75] S.-F. Chang, J.-L. Chen, Y.-H. Jeng and C.-T. Wu, "New High-Directivity Couplers Design With Coupled Spurlines," *IEEE Microwave and Wireless Components Letters*, vol. 14, no. 2, pp. 65-67, 2004.
- [76] Keysight Technologies, "De-Embedding and Embedding S-Parameter Networks Using a Vector Network Analyzer," 2017.
- [77] Agilent, "Agilent AN 154: S-Parameter Design".
- [78] D. C. DeGroot, J. A. Jargon and R. B. Marks, "Multiline TRL Revealed," in *ARFTG Conference Digest*, Washington DC, 2002.
- [79] R. Walton, *Mason.m*, Matlab Central, 2016.

- [80] D. Veit, M. Gadringer and E. Leitgeb, "About Different Load Configurations for Mixed-Mode Load-Pull Measurements," in *2019 European Microwave Conference in Central Europe (EuMCE)*, Prague, 2019.
- [81] D. Veit, M. Gadringer and E. Leitgeb, "About Different Load Configurations for Mixed-Mode Load-Pull Measurements, Hybrid Imperfections and Tuning Range," *International Journal of Microwave and Wireless Technologies (IJMWT)*, 2020.
- [82] J. Frej, X.-D. Cai and S. Muller, "Multiport S-Parameter and T-Parameter Conversion With Symmetry Extension," *IEEE Transactions on Microwave Theory and Techniques*, vol. 56, no. 11, pp. 2493-2504, 2008.
- [83] Mini-Circuits, [Online]. Available: <https://www.minicircuits.com/>. [Accessed 25 11 2019].
- [84] D. Veit, A Feasibility Study of Novel Applications in Automotive UWB Radar Systems, Graz: Graz University of Technology, 2016.
- [85] J. Kulmer, S. Hinteregger, B. Großwindhager, M. Rath, M. S. Bakr, E. Leitinger and K. Witrisal, "Using DecaWave UWB Transceivers for High-accuracy Multipath-assisted Indoor Positioning," in *2017 IEEE International Conference on Communications Workshops (ICC Workshops)*, Paris, 2017.
- [86] M. Z. Win and R. Scholtz, "Characterization of ultra-wide bandwidth wireless indoor channels: a communication-theoretic view," in *IEEE Journal on Selected Areas in Communications*, Vol. 20, Iss. 9, 2002, pp. 1613 - 1627.
- [87] Maury Microwave, "A Beginner's Guide To All Things Load Pull," March 2015. [Online]. Available: <https://www.maurymw.com/pdf/datasheets/5A-062.pdf>. [Accessed 26 May 2020].
- [88] D. Giuseppe and R. Giovanni, "On the Validity of Gaussian Approximation to Characterize the Multiuser Capacity of UWB TH PPM," in *2002 IEEE Conference on Ultra Wideband Systems and Technologies*, Baltimore, MD, USA, 2002.

List of Own Publications

Consistent Scaling for the Inverse Chirp-Z Transformation; David Veit, Michael Vorderderfler, Michael Gadringer, Erich Leitgeb; 2020, IEICE Information and Communication Technology Forum (ICTF 2020), Submitted

On Different Load Configurations for Mixed Mode Load-Pull Measurements, Hybrid Imperfections and Tuning Ranges; David Veit, Michael Gadringer, Erich Leitgeb; 2020, International Journal of Microwave and Wireless Technologies; Special Issue EuMCE 2019

On UWB Pulse Distortion Caused by Amplifiers and Mismatched Antennas; David Veit, Michael Gadringer, Erich Leitgeb; 2020, 6th International Conference on Microwaves for Intelligent Mobility; Accepted

Impact of UWB Antennas on Ranging Accuracy; David Veit, Michael Gadringer, Erich Leitgeb; 2020, 14th European Conference on Antennas and Propagation (EuCAP)

About Different Load Configurations for Mixed-Mode Load-Pull Measurements; David Veit, Michael Gadringer, Erich Leitgeb; 2019, European Microwave Conference in Central Europe (EuMCE); 2nd Place: Best Student Paper Award

A Simulation Environment for UWB Hardware Development and Protocol Design; David Veit, Michael Gadringer, Erich Leitgeb; 2019, 15th International Conference on Telecommunications (ConTEL)

A Compact Ultra-Wideband Load-Pull Measurement System; David Veit, Michael Gadringer, Erich Leitgeb; 2018, International Conference on Broadband Communications for Next Generation Networks and Multimedia Applications (CoBCom)

UWB Channel Measurements for Short Range Radar Applications; David Veit, Erich Leitgeb, Franz Teschl, Thomas Gigl; 2017, 25th International Conference on Software, Telecommunications and Computer Networks (SoftCOM)

A Feasibility Study of Novel Applications in Automotive UWB Radar Systems; Master Thesis of David Veit; 14.12.2016, Institute of Microwave and Photonic Engineering, Graz University of Technology

Appendix

The appendix contains additional information that would interrupt the flow of the thesis if placed directly in its main sections. At specific points in the thesis parts of the appendix are referenced for the reader interested in specific details.

Appendix A: Chirp Z-Transformation and Correct Normalization

The Chirp-Z Transformation (CZT) is a generalized form of the Discrete Fourier Transformation (DFT) and can be used for efficient frequency-time-domain conversions. It is very flexible as, in contrast to the DFT and Inverse Discrete Fourier Transformation (IDFT) target frequency and time vectors can be provided for the transformation. This allows efficient conversion of sparse signals and interpolation in a single transformation step [17] [18]. In my opinion, one of the biggest practical advantages of the Inverse Chirp-Z Transformation (ICZT) is that the input frequency vector does not have to start at DC (0 Hz) to generate a real valued time domain signal out of a symmetric spectrum. This is of practical importance as vector network analyzers are usually not able to perform measurements down to DC. With this flexibility comes a problem, which is most often not mentioned in literature. If the transformation is performed with different time or frequency vectors, the output signals will be scaled differently. To understand why this happens please think about the following example. For this example, I use an implementation of the CZT, which conserves the energy of the signal on both sides of the transformation. If you now perform two ICZTs using the same input frequency domain signal, but time domain vectors with different sampling frequencies, the available energy is spread over a different number of samples. This results in the case that the magnitude of the time domain signal with lower sample rate will be higher than the magnitude of the time domain signal with higher sample rate, although they were calculated from the same frequency domain signal. If this effect is not understood this might lead to misinterpretations of measurement results. The whole situation becomes even more complicated because not only the sample rate, but also the start and end time points of the time vector can vary, as well as the input frequency vectors. To deal with this problem I present my Matlab[®] implementation of the ICZT which provides an additional scaling factor as output of the transformation. By applying this scaling factor to the time domain signal the user can correct for the above-mentioned effect.

A.1 Results

In this section, I show results obtained by using my implementations of the CZT and ICZT. I compare them to the DFT and IDFT and show their limitations. For this I used the test signals shown in Figure A.1, which are generated by multiplying a 1 ns rectangular window with a 10 GHz carrier as shown in (A.1) to (A.4). The sampled signal $s[n]$ uses a sampling frequency of 28 GHz. These test signals are well suited for demonstration of the CZT as they are sparse in time allowing to demonstrate the time windowing property of the ICZT.

$$s_c(t) = w(t) \cdot \cos(2\pi t f_c) \quad (\text{A.1})$$

$$w(t) = \begin{cases} 1 & 29.5 \text{ ns} < t < 30.5 \text{ ns} \\ 0 & \text{otherwise} \end{cases} ; f_c = 10 \text{ GHz} \quad (\text{A.2})$$

$$\underline{s} = s[n] = s_c(nT) = s_c(n \cdot 1/F_s) \quad (\text{A.3})$$

$$\underline{t} = t[n] = nT \quad (\text{A.4})$$

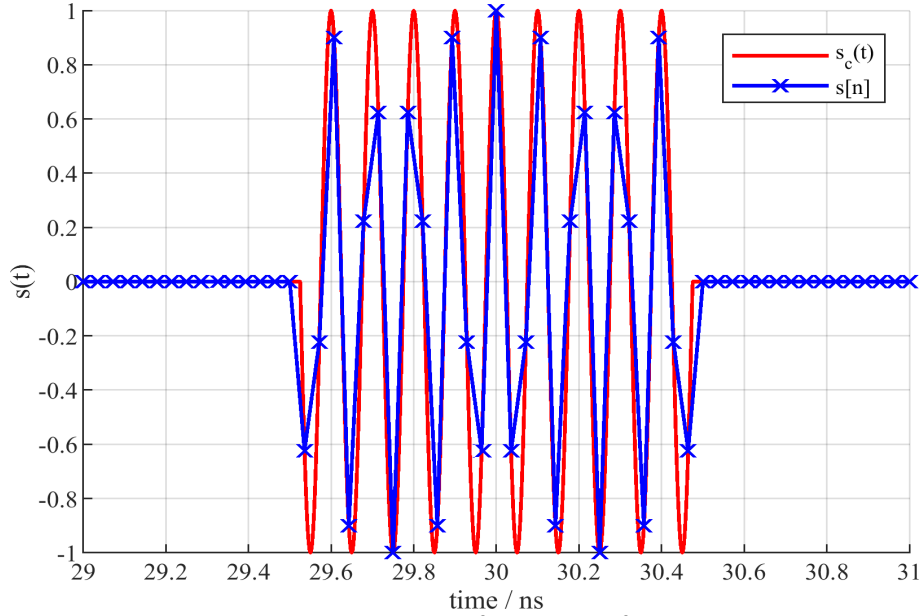


Figure A.1. input signals used for analysis of CZT and ICZT.

In a first step, we need to calculate the complex spectrum of the signal in order to test the ICZT. For this purpose, I used the built in FFT function of Matlab® in (A.5) and my implementation of the CZT in (A.8). As mentioned, the CZT needs the source time vector and target frequency vector as additional inputs. If the frequency vector is chosen to be identical to the one of the FFT, the CZT and FFT yield identical results. This is visualized in Figure A.2. Using the calculated spectrum, we can now apply the ICZT to get back the time domain signal. If the same time vector is used, the ICZT yields the original signal s as shown in Figure A.3 and (A.7). For (A.8) I selected, a different time vector t'' , which uses the same number of samples but starts at 29.2 ns and ends at 30.8 ns. Because I used the same number of samples for a shorter time interval, the ICZT now inherently performs an interpolation of the time domain signal, which can be seen in Figure A.3. As transformation and interpolation is performed in the same step this is a very efficient implementation, and it can be reversed using the corresponding inverse function with the same time and frequency vectors. To achieve the correct magnitude for the interpolated signal s'' , the signal in Figure A.3 was multiplied by the magnitude correction factor A'' . The matching frequency domain representation was calculated in (A.9). Please note that for this s'' was divided by A'' before the transformation. As the CZT is a linear transformation the scaling could be performed at a different position, but I chose to apply it to the time domain signal before the transformation. The result of (A.9) is plotted in Figure A.2. You can observe that because of the interpolation the sampling frequency of the signal is much higher than for the original signal, but due to the number of points is the same, the frequency spacing between points in the spectrum increased. By using this interpolation, the signal s'' in Figure A.3 looks very similar to the analog signal $s(t)$. Only at the edges of the rectangular window, the signal could not follow the quick change because of the missing bandwidth.

$$\underline{S}_{FFT} = FFT\{s\} \quad (A.5)$$

$$\underline{S}_{CZT} = myCZT\{\underline{t}, \underline{s}, f\} \quad (A.6)$$

$$\underline{s}' = myICZT(f, \underline{S}_{CZT}, \underline{t}) = \underline{s} \quad (A.7)$$

$$[\underline{s}'', A''] = myICZT(f, \underline{S}_{CZT}, \underline{t}'') \quad (A.8)$$

$$\underline{S}_{CZT}'' = myCZT\left(\underline{t}'', \frac{\underline{s}''}{A''}, f''\right) \quad (A.9)$$

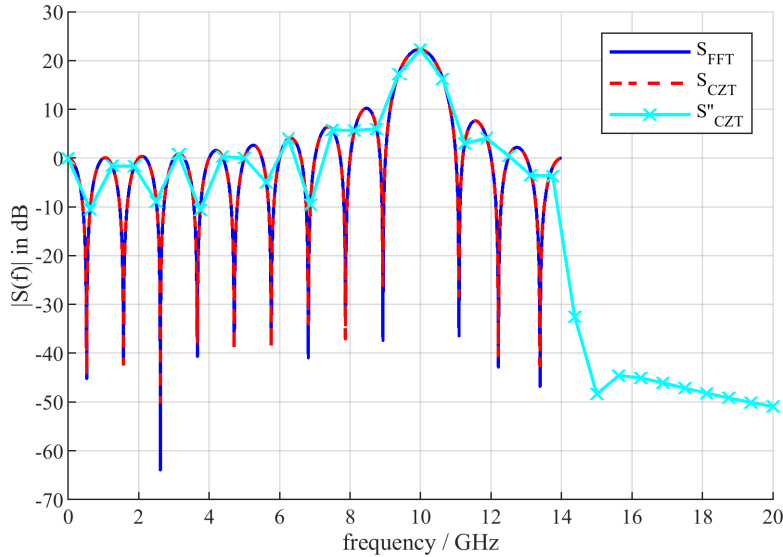


Figure A.2. Frequency domain representation of the sampled test signal using Fast Fourier Transformation (blue line), CZT (dashed red line) and CZT of the time windowed signal, which was created using the ICZT on the FFT result of the sampled signal.

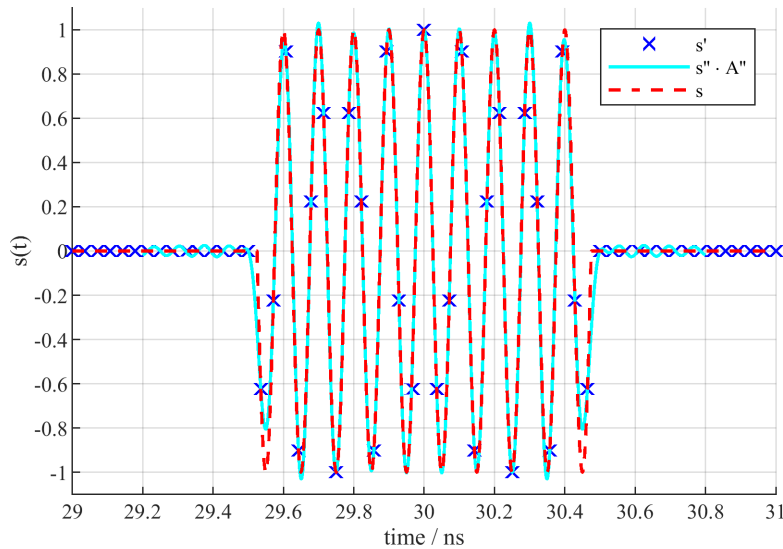


Figure A.3. Time domain representation of the analog reference signal (red), a signal calculated using ICZT with the original time vector \underline{t} (blue) and a signal calculated using a truncated time vector with higher sample rate \underline{t}'' (cyan).

Until now, I only showed transformations for spectra starting at DC, which could as well be transformed using the IDFT. In Figure A.4 and Figure A.5 I show the impact of applying the ICZT to spectrum data ranging from 3 GHz to 14 GHz. The calculation of the blue spectrum in Figure A.4 is shown in (A.10) and (A.11), and simply is the truncated spectrum of the original sampled signal. By applying the ICZT in (A.12) a real valued time domain signal can be calculated from this spectrum, which is shown as cyan

colored line in Figure A.5. Using the same time and frequency vectors as in (A.9) the frequency domain representation of this signal (S'_{NoDC}), which now contains frequency components down to DC, is calculated in (A.13) and also presented in the spectrum plot. What happens if a frequency vector extending over the alias free range is supplied for the CZT is presented in (A.14) and Figure A.4. To discuss this case, the original signal s was transformed into frequency domain using the frequency vector of the interpolated signal, which causes aliasing. The same occurs for the ICZT if a time vector exceeding the alias free time is supplied for the transformation. My implementation of the CZT and ICZT will provide you with a warning in such a case.

$$f_{NoDC} = f|_{3\text{ GHz} < f < 14\text{ GHz}} \quad (\text{A.10})$$

$$\underline{S}_{NoDC} = S_{FFT}|_{f_{NoDC}} \quad (\text{A.11})$$

$$[\underline{S}_{NoDC}, A_{NoDC}] = \text{myICZT}(\underline{f}_{NoDC}, \underline{S}_{NoDC}, \underline{t}'') \quad (\text{A.12})$$

$$\underline{S}'_{NoDC} = \text{myCZT}\left(\underline{t}'', \frac{\underline{S}_{NoDC}}{A_{NoDC}}, \underline{f}''\right) \quad (\text{A.13})$$

$$\underline{S}''_{NoDC} = \text{myCZT}(t, \underline{s}, \underline{f}'') \quad (\text{A.14})$$

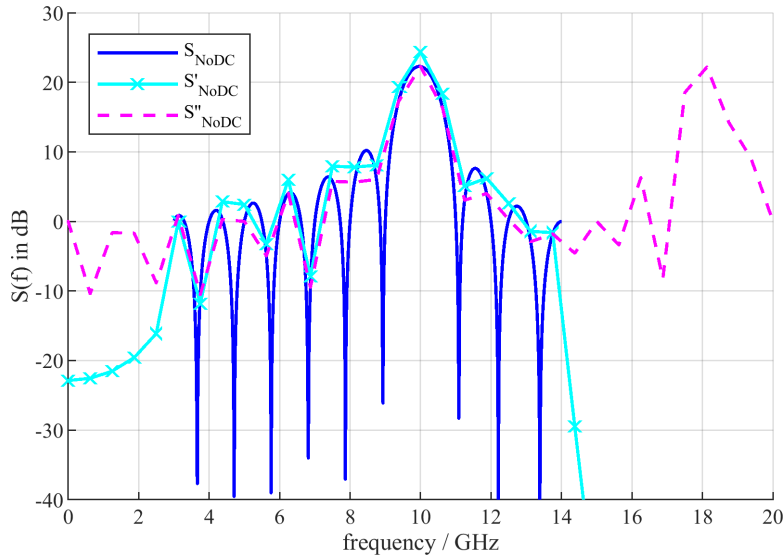


Figure A.4. Plot of a spectrum with missing lower frequency components (blue), the spectrum of a signal after the missing components where extrapolated using ICZT (cyan) and spectrum of the original signal s with extrapolation of higher frequency components above the alias free range using CZT (dashed magenta).

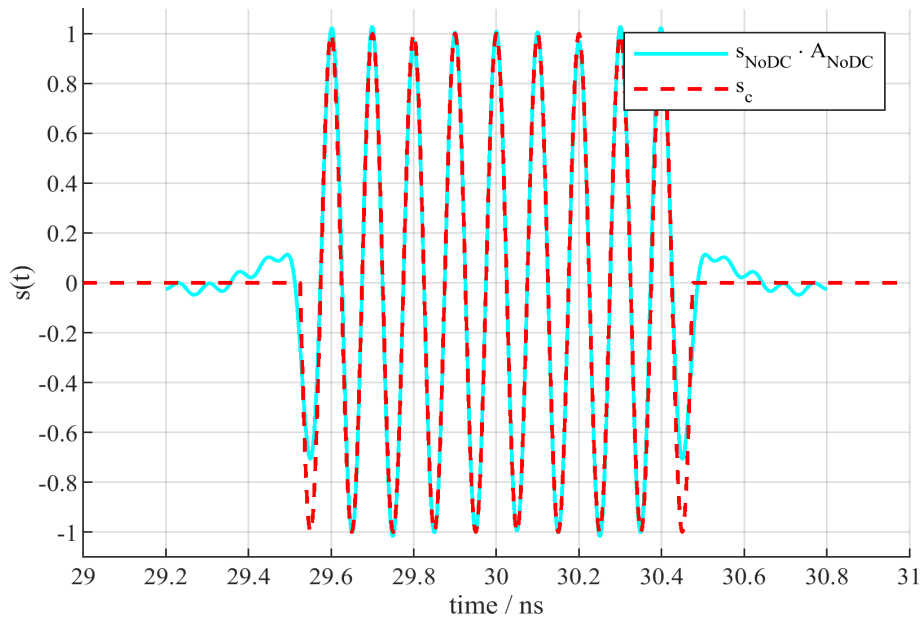


Figure A.5. Time domain signal calculated from a spectrum with missing lower frequency components using ICZT (cyan) and reference signal (red).

In this section, I presented my approach to normalizing the time domain signals generated by the ICZT. For this normalization, it is mandatory that the provided time and frequency vectors contain equally spaced samples. This is not a formal requirement for the CZT or ICZT itself. For example, two spectra with different frequency ranges and frequency spacing could be combined using ICZT. In such a case the mentioned normalization factor will not be correct and should be omitted. At this point, I would also like to mention that if the time and frequency vectors are constant for all measurements, the scaling factor will also be constant, allowing a comparison of the measurements without applying any scaling factors.

A.2 CZT Implementation

As transformations come in pairs, I show my implementation of the CZT first.

```

% Author: David Veit
% Date: 03.06.2020
function [f, X] = myCZT(t, x, f)
%myCZT computes the Chirp-Z Transform from the given time signal for the
%provided frequency points. The result should be equal to the result of FFT
%if the same frequency vector is used. Like the FFT the output is not
%normalized by the length of the frequency vector resulting in an output
%independent of the vector length.
% input:
% t ... time vector
% x ... time signal
% f ... desired frequency grid
% output:
% f ... frequency vector
% X ... complex spectrum vector

%% Input argument check
if nargin < 2
    error('Not enough input arguments.')
end

T = mean(t(2:end) - t(1:end-1)); % in case t is not exactly equally spaced
Fs = 1 / T;
if nargin < 3
    f = linspace(-Fs/2, Fs/2, length(t));
else
    if max(abs(f)) > Fs/2
        warning('Specified frequency vector exceeds alias free range.')
    end
end

f = f(:)';
x = x(:);
t = t(:);

if size(t) ~= size(x)
    error('Dimensions of time vector and signal do not match.')
end
end

```

```

%% Calculate transformation
x_matrix = repmat(x, 1, length(f));
X = sum(x_matrix .* exp(-1i * 2*pi * t * f) ,1);

X = X(:);

end

```

A.3 ICZT Implementation

```

% Author: David Veit
% Date: 03.06.2020
function [t, x, magnitude_scaling_factor] = myICZT(f, X, t, spectrum_type, supress_warning)
%myICZT computes the Inverse Chirp-Z Transform
% Computes the inverse Chirp Z transform of the given frequency spectrum.
% The advantage is that the frequency grid does not need to be uniform or
% extend down to DC.
% input:
% f ... frequency vector
% X ... complex spectrum vector
% t ... desired time vector of the transformed time signal. If set to 0
% the default time vector will be used. (identical to IFFT)
% spectrum_type ... "single" or "double". Type of the supplied spectrum.
% Default value is single sided spectrum.
% supress_warning ... supress warning if energy of input and output
% signals are not equal if true. This can be used if parts of the
% signal are cut away intentionally.
% output:
% t ... time vector of transformed signal
% x ... time domain signal
% magnitude_scaling_factor ... the ICZT conserves the energy of a signal.
% If interpolation is used the magnitude is lowered because the power per
% sample declines. x * magnitude_scaling_factor results in the signal
% having the same amplitude as before the interpolation but changes the
% energy.

%% Input argument check
if nargin < 2
    error('Not enough input arguments.')
end

f = f(:);
f_low = min(abs(f));
f_high = max(abs(f));
X = X(:);
t = t(:)';
if size(f) ~= size(X)
    error('Dimensions of frequency vector and spectrum do not match.')
end

% Generate frequency grid
if nargin < 3
    spectrum_type = 'single';
end

if nargin < 4
    spectrum_type = 'single';
end

if nargin < 5
    supress_warning = 0;
end

switch spectrum_type
    case 'single'
        if f(1) > 0
            f = [-f(end:-1:1); f];
            X_two_sided = [conj(X(end:-1:1)); X];
        elseif f(1) == 0
            f = [-f(end:-1:2); f];
            X_two_sided = [conj(X(end:-1:2)); X];
        elseif f(1) < 0
            error('Frequency vector must be positive for single sided spectra.')
        end
    case 'double'
        X_two_sided = X;
    otherwise
        error('Spectrum type not recognized. Valid values are "single" and "double".')
end

% Generate time vector
T_alias = 1 / abs(f(2) - f(1));
if nargin < 3 || length(t) <= 1
    Td = 1/(max(abs(f))*2);
    t = 0:Td:T_alias;
end

%% Check time vector
if t(end) > T_alias + eps
    warning('Provided time vector exceeds alias free time.')
end

time_vector_power_correction_factor = sqrt((t(end)-t(1)) / T_alias) ;

%% Calculate transformation
X_matrix = repmat(X_two_sided, 1, length(t));
x = conj(1/sqrt(length(t)*length(f)) * sum(X_matrix .* exp(1i * 2*pi * f * t) ,1));

% Correct power error due to time window

```

```

x = x * time_vector_power_correction_factor;

% magnitude scaling factor
% account for windowing of time vector
time_vector_factor = sqrt(length(t)/length(f)) / time_vector_power_correction_factor;
% account for banded frequency vector
frequency_vector_factor = (f_high - f_low) / f_high

magnitude_scaling_factor = time_vector_factor * frequency_vector_factor;

%% Energy comparison
E_t = sum(x .* conj(x));
E_f = sum((X_two_sided .* conj(X_two_sided)) / length(X_two_sided));
energy_error = abs(E_t - E_f)/E_t * 100
if (energy_error > 0.5) && ~supress_warning
    warning(['Energy error due to IC2T is ' num2str(energy_error) '%']);
end

% Correct small imaginary result for single sided spectra
x(imag(x) < 5*eps) = real(x(imag(x) < 5*eps));
x = x(:);
end

```

Appendix B: Mixed-Mode S-Parameters for Matlab®

This section contains a transformation from conventional S-parameters to generalized mixed-mode scattering S-parameters as they were discussed in Section 2.3. For a detailed derivation, I refer to [37]. This class can be used to generate mixed-mode S-parameter objects like the conventional S-parameter objects of the Matlab® RF Toolbox. The implementation has been verified for real valued port impedances. Please note that the characteristic impedances of differential line differ from the characteristic impedance of a 50 Ohm single-ended line. The differential-mode impedance of a differential line made of two 50 Ω lines without coupling is 100 Ω , the corresponding common-mode impedance is 25 Ω . By supplying appropriate reference impedances, the resulting differential and common-mode reflection coefficients can be plotted to the same Smith Chart, although they are normalized to different reference impedances. Mode conversion parameters cannot be mapped to impedances and therefore should be visualized in polar plots instead of Smith charts.

```

% Author: David Veit
% Date: 03.06.2020
classdef SGeneral < handle
    %SGeneral is used to convert conventional S-parameters to generalized
    % mixed-mode scattering S-parameters.

    properties (Access = public)
        NumPorts % Number of all ports
        NumDiffPorts % Number of differential port pairs
        Parameters % General S-parameters
        Frequencies % Frequency vector for S-parameters
        single_ended_port_impedances % Single ended port impedances for each of the N ports
        differential_mode_port_impedances % Differential mode port impedance for each differential port
        common_mode_port_impedances % Common mode port impedance for each common mode port
        % Matrix containing information how the input single ended ports are connected to form differential ports
        diff_port_pairs
        port_order % shows how the ports have been reordered for simpler calculations
    end

    methods (Access = public)
        function obj = SGeneral(S, diff_port_pairs, type, differential_port_impedances, common_port_impedances)
            %SGeneral constructs a new generalized S-parameter object.
            % Arguments
            % S ... S-parameter object (Matlab RF toolbox)
            % diff_port_pairs ... matrix containing the differential port
            % pairs. Matrix has to have p rows and 2 columns, where p is
            % the number of differential port pairs.
            % type ... type of the input S-parameter object (single ended
            % or generalized)
            % differential_port_impedances, common_port_impedances ...
            % vectors containint the reference impedances of the
            % calculated mixed mode port parameters.

            % Check input arguments
            if nargin < 3
                error('Not sufficient input arguments')
            elseif nargin == 3
                obj.NumPorts = S.NumPorts;
                obj.NumDiffPorts = size(diff_port_pairs, 1);
                obj.diff_port_pairs = diff_port_pairs;
                obj.Frequencies = S.Frequencies;
                obj.single_ended_port_impedances = S.Impedance;
                obj.differential_mode_port_impedances = obj.single_ended_port_impedances * 2 * ones(obj.NumDiffPorts, 1);
                obj.common_mode_port_impedances = obj.single_ended_port_impedances / 2 * ones(obj.NumDiffPorts, 1);
            elseif nargin == 5
                obj.NumPorts = S.NumPorts;
                obj.NumDiffPorts = size(diff_port_pairs, 1);
                obj.diff_port_pairs = diff_port_pairs;
                obj.Frequencies = S.Frequencies;
            end
        end
    end
end

```

```

obj.single_ended_port_impedances = S.Impedance;

if length(differential_port_impedances) ~= obj.NumDiffPorts || ...
    length(common_port_impedances) ~= obj.NumDiffPorts
    error('Number of mentioned impedances and differential ports does not match.')
end
obj.differential_mode_port_impedances = differential_port_impedances;
obj.common_mode_port_impedances = common_port_impedances;
else
    error('Number of input arguments not supported')
end

% Calculate generalised S-parameters according to the given
% input data format
if strcmp('single',type)
    obj.calculateGeneralisedParameters(S);
else
    error('This input type is currently not supported.')
end

end

function S_general = calculateGeneralisedParameters(obj, S)
%calculateGeneralisedParameters is used to update the stored
%parameters using the stored configuration data and provided
%S-parameter data.
% arguments:
% S ... S-parameter object containing the single ended data
% return values:
% S_general ... generalised S-parameter data

n = obj.NumPorts; % number of ports
p = 2 * obj.NumDiffPorts; % number of differential ports
%(single ended ports which form a mixed mode port = diff. mode port + common mode port)

% Reorder ports according to map
port_ordering_vect = [];
port_list = 1:n;
for i_port = 0:obj.NumDiffPorts-1
    port_ordering_vect(i_port*2+1) = obj.diff_port_pairs(i_port+1,1);
    port_list(port_list == obj.diff_port_pairs(i_port+1,1)) = -1;
    port_ordering_vect(i_port*2+2) = obj.diff_port_pairs(i_port+1,2);
    port_list(port_list == obj.diff_port_pairs(i_port+1,2)) = -1;
end

% Remove already used ports and add other ports to the list
port_list(port_list<0) = [];
port_list = port_list(:);
port_ordering_vect = port_ordering_vect(:);
port_ordering_vect = vertcat(port_ordering_vect, port_list);
obj.port_order = port_ordering_vect;

S = snp2smp(S, port_ordering_vect);

% Calculate parts of the xi block matrix
X = zeros(4, 4, p/2); % third dimension is used for X12, X34, X56, ..., X(p-1)p

for i = 1:p/2
    % choose ports from port map
    j = i * 2 - 1;
    k = i * 2;

    % choose values corresponding to the ports --> to fit equation in book

    Z_j = obj.single_ended_port_impedances;
    Z_k = obj.single_ended_port_impedances;
    Z_djk = obj.differential_mode_port_impedances(i);
    Z_cjk = obj.common_mode_port_impedances(i);
    R_djk = real(Z_djk);
    R_cjk = real(Z_cjk);
    R_j = real(Z_j);
    R_k = real(Z_k);

    D = sqrt(R_djk) / (2 * abs(Z_djk));
    C = sqrt(R_cjk) / (2 * abs(Z_cjk));
    A_j = sqrt(R_j) / (2 * abs(Z_j));
    A_k = sqrt(R_k) / (2 * abs(Z_k));
    T = [1 0 -1 0; 0 1/2 0 -1/2; 1/2 0 1/2 0; 0 1 0 1];

    M_dash = [D, D*Z_djk, 0, 0; D, -D*Z_djk, 0, 0; 0, 0, C, C*Z_cjk; 0, 0, C, -C*Z_cjk];

    M = [A_j, A_j*Z_j, 0, 0; A_j, -A_j*Z_j, 0, 0; 0, 0, A_k, A_k*Z_k; 0, 0, A_k, -A_k*Z_k];

    Xjk = M_dash * T / M;

    X(:, :, i) = Xjk;
end

% Calculate Xi block matrix
Xi = zeros(2 * n, 2 * n);
for i = 1:p/2
    start = (i-1) * 4 + 1;
    Xi(start:start+3, start:start+3) = X(:, :, i);
end

if n > p
    I = diag(ones(2*(n-p),1));
    start = i * 4 + 1;
    Xi(start:end, start:end) = I;
end
end

```



```

% Calculate permutation matrices for the Xi block matrix
P_da = zeros(p/2, 2*n);
for i = 1:p/2
    P_da(i, 4*i-3) = 1;
end

P_ca = zeros(p/2, 2*n);
for i = 1:p/2
    P_ca(i, 4*i-1) = 1;
end

P_db = zeros(p/2, 2*n);
for i = 1:p/2
    P_db(i, 4*i-2) = 1;
end

P_cb = zeros(p/2, 2*n);
for i = 1:p/2
    P_cb(i, 4*i) = 1;
end

P_a = zeros(n-p, 2*n);
for i = 1:(n-p)
    P_a(i, 2*p + 2*i - 1) = 1;
end

P_b = zeros(n-p, 2*n);
for i = 1:(n-p)
    P_b(i, 2*p + 2*i) = 1;
end

P = [P_da; P_ca; P_a; P_db; P_cb; P_b];

Q_a = zeros(n, 2*n);
for i = 1:n
    Q_a(i, 2*i-1) = 1;
end

Q_b = zeros(n, 2*n);
for i = 1:n
    Q_b(i, 2*i) = 1;
end

Q = [Q_a; Q_b];

% Apply permutation (port reordering) to Xi matrix
Xi = P * Xi * Q';

% Split Xi Matrix in sub matrices
Xi_11 = Xi(1:n, 1:n);
Xi_12 = Xi(1:n, n+1:2*n);
Xi_21 = Xi(n+1:2*n, 1:n);
Xi_22 = Xi(n+1:2*n, n+1:2*n);

S = S.Parameters;
obj.Parameters = zeros(size(S,1),size(S,2),size(S,3));
for i_f = 1:size(S,3)
    s_one_frequency = S(:, :, i_f);
    obj.Parameters(:, :, i_f) = (Xi_21 + Xi_22 * s_one_frequency) / (Xi_11 + Xi_12 * s_one_frequency);
end
S_general = obj.Parameters;
end

function S_single = calculateSingleEndedParameters(obj)
%calculateSingleEndedParameters is used to calculate the single
%ended S-parameters from the stored generalized S-parameters.

n = obj.NumPorts; % number of ports
p = 2 * obj.NumDiffPorts; % number of differential ports
% (single ended ports which form a mixed mode port = diff. mode port + common mode port)

% Reorder ports according to map
port_ordering_vect = [];
port_list = 1:n;
for i_port = 0:obj.NumDiffPorts-1
    port_ordering_vect(i_port*2+1) = obj.diff_port_pairs(i_port+1,1);
    port_list(port_list == obj.diff_port_pairs(i_port+1,1)) = -1;
    port_ordering_vect(i_port*2+2) = obj.diff_port_pairs(i_port+1,2);
    port_list(port_list == obj.diff_port_pairs(i_port+1,2)) = -1;
end

% Remove already used ports and add other ports to the list
port_list(port_list<0) = [];
port_list = port_list(:);
port_ordering_vect = port_ordering_vect(:);
port_ordering_vect = vertcat(port_ordering_vect, port_list);
obj.port_order = port_ordering_vect;

%S = snp2smp(S, port_ordering_vect);
% Calculate parts of the xi block matrix
X = zeros(4, 4, p/2); % third dimension is used for X12, X34, X56, ..., X(p-1)p

for i = 1:p/2
    % choose ports from port map
    j = i * 2 - 1;
    k = i * 2;

    % choose values corresponding to the ports --> to fit equation in book
    Z_j = obj.single_ended_port_impedances;
    Z_k = obj.single_ended_port_impedances;
    Z_djk = obj.differential_mode_port_impedances(i);
    Z_cjk = obj.common_mode_port_impedances(i);
    R_djk = real(Z_djk);

```

```

R_cjk = real(Z_cjk);
R_j = real(Z_j);
R_k = real(Z_k);

D = sqrt(R_djk) / (2 * abs(Z_djk));
C = sqrt(R_cjk) / (2 * abs(Z_cjk));
A_j = sqrt(R_j) / (2 * abs(Z_j));
A_k = sqrt(R_k) / (2 * abs(Z_k));
T = sym([1 0 -1 0; 0 1/2 0 -1/2; 1/2 0 1/2 0; 0 1 0 1]);

M_dash = [D, D*Z_djk, 0, 0; D, -D*Z_djk, 0, 0; 0, 0, C, C*Z_cjk; 0, 0, C, -C*Z_cjk];

M = [A_j, A_j*Z_j, 0, 0; A_j, -A_j*Z_j, 0, 0; 0, 0, A_k, A_k*Z_k; 0, 0, A_k, -A_k*Z_k];

Xjk = M_dash * T / M;

X(:, :, i) = Xjk;
end

% Calculate Xi block matrix
Xi = zeros(2 * n, 2 * n);
for i = 1:p/2
    start = (i-1) * 4 + 1;
    Xi(start:start+3, start:start+3) = X(:, :, i);
end

if n > p
    I = diag(ones(2*(n-p), 1));
    start = i * 4 + 1;
    Xi(start:end, start:end) = I;
end

% Calculate permutation matrices for the Xi block matrix
P_da = zeros(p/2, 2*n);
for i = 1:p/2
    P_da(i, 4*i-3) = 1;
end

P_ca = zeros(p/2, 2*n);
for i = 1:p/2
    P_ca(i, 4*i-1) = 1;
end

P_db = zeros(p/2, 2*n);
for i = 1:p/2
    P_db(i, 4*i-2) = 1;
end

P_cb = zeros(p/2, 2*n);
for i = 1:p/2
    P_cb(i, 4*i) = 1;
end

P_a = zeros(n-p, 2*n);
for i = 1:(n-p)
    P_a(i, 2*p + 2*i - 1) = 1;
end

P_b = zeros(n-p, 2*n);
for i = 1:(n-p)
    P_b(i, 2*p + 2*i) = 1;
end

P = [P_da; P_ca; P_a; P_db; P_cb; P_b];

Q_a = zeros(n, 2*n);
for i = 1:n
    Q_a(i, 2*i-1) = 1;
end

Q_b = zeros(n, 2*n);
for i = 1:n
    Q_b(i, 2*i) = 1;
end

Q = [Q_a; Q_b];

% Apply permutation (port reordering) to Xi matrix
Xi = P * Xi * Q';
% Split Xi Matrix in sub matrices
Xi_11 = Xi(1:n, 1:n);
Xi_12 = Xi(1:n, n+1:2*n);
Xi_21 = Xi(n+1:2*n, 1:n);
Xi_22 = Xi(n+1:2*n, n+1:2*n);

S = obj.Parameters;
S_single = zeros(size(S,1), size(S,2), size(S,3));
for i_f = 1:size(S,3)
    s_one_frequency = S(:, :, i_f);
    S_single(:, :, i_f) = (Xi_22 - s_one_frequency * Xi_12) \ (s_one_frequency * Xi_11 - Xi_21);
end

end

function [I, frequency_error] = calculateIndexForFrequencyPoint(obj, frequency)
%calculateIndexForFrequency point calculates the index for a
%specific frequency point.
[frequency_error, I] = min(abs(obj.Frequencies - frequency));
end

end
end

```